THESIS FOR THE DEGREE OF DOCTOR OF PHILOSOPHY

Pd- and Pt-based Nanomaterials for Hydrogen Sensing in Complex Environments: The Role of Composition, Morphology and Defects

CARL ÅKE EMIL ANDERSSON

Department of Physics and Astronomy

CHALMERS UNIVERSITY OF TECHNOLOGY

Gothenburg, Sweden 2026

Pd- and Pt-based Nanomaterials for Hydrogen Sensing in Complex Environments: The Role of Composition, Morphology and Defects

CARL ÅKE EMIL ANDERSSON

ISBN 978-91-8103-411-0

Doktorsavhandlingar vid Chalmers tekniska högskola

Ny serie nr 5868

ISSN 0346-718X

https://doi.org/10.63959/chalmers.dt/5868

Department of Physics and Astronomy

Chalmers University of Technology

SE-412 96 Gothenburg

Sweden

Telephone + 46 (0)31-772 1000

Cover:

Historical to contemporary experimental methods for investigating H_2 absorption in Pd and Pt. Clockwise from the top: Sprengel pump used by Graham in the 19th century, single-particle nanocompression, visualization of defect-rich and alloy nanoparticles, single-particle resolution multiplexing on a single substrate.

Printed by Chalmers Digitaltryck

Gothenburg, Sweden 2026

"Everything is connected but nothing is working"

- *Asteroid City*

Abstract

CARL ÅKE EMIL ANDERSSON

Department of Physics and Astronomy

Chalmers University of Technology

In many technological applications of hydrogen gas (H_2), H_2 interacts with different forms of metals. H_2 sensors are one example, where irrespective of the sensing principle, Pd, Pt and their alloys often constitute the active sensing material. While reasonably well characterized for bulk systems, e.g. macroscopic films, the interaction of H_2 with nanoparticle alloys, which in this thesis generally are in the form of disks with a diameter of ~100 nm, remains a widely uncharted territory. Especially in chemically complex environments that include species like O_2, H_2O, CO and NO_X.

In this thesis, the hydrogen sorption characteristics and morphological evolution of neat Pd, Pt, and more than 70 alloy combinations of the two, both at the single nanoparticle and at the ensemble level are investigated. To do so, we have developed a new nanolithography fabrication method, that is combined with plasmonic nanospectroscopy, dark-field nanomicroscopy and electron microscopy and spectroscopy.

First, we find a strong intrinsic link between the evolution of hydrogen sorption kinetics and single-particle specific defect networks. Secondly, we quantify how a few atomic percent of secondary alloyants can stabilize the structure of these particles during heavy H_2 cycling and consequently also stabilize the time evolution of hydrogen sorption kinetics. This is important in H_2 sensor applications because it paves the way to sensors which deliver a stable response over extended operation. We also demonstrate how systematic alloy composition screening of Pd- and Pt-based alloy and hybrid nanoparticles, together with advanced deep learning-based data analyzation, can be leveraged to achieve plasmonic H_2 sensors that operate efficiently in technologically relevant, but highly challenging, environments, i.e., air with high levels of O_2, CO, NO_x and varying relative humidities.

Keywords: plasmonics, nanoparticles, multiplexing, nanofabrication, hydrogen, hydride, sensor, palladium, platinum, alloy, defect engineering.

List of Appended Papers

This thesis is based on the following appended papers:

Paper I: Andersson, C.; Zimmerman, J.; Fritzsche, J.; Rabkin, E.; Langhammer, C., Hydride formation pressures and kinetics in individual Pd nanoparticles with systematically varied levels of plastic deformation. *Nature Communications* **2025,** 16 (1), 9242.

Paper II: Theodoridis, A.; **Andersson, C.**; Nilsson, S.; Fritzsche, J.; Langhammer, C., A Catalytic-Plasmonic Pt Nanoparticle Sensor for Hydrogen Detection in High-Humidity Environments. *ACS Sensors* **2025,** 10 (11), 8983-8994.

Paper III: Theodoridis, A.*; **Andersson, C.***; Martvall, V.; Colliander, W.; Erhart, P.; Langhammer, C. Pd-Pt Nanostructures for Deep-Learning-Augmented Plasmonic Hydrogen Sensing in Dry and Humid Air. *In manuscript.* *equal contribution

Paper IV: Andersson, C; Serebrennikova, O.; Tiburski, C.; Alekseeva, S.; Fritzsche, J.; Langhammer, C., A Microshutter for the Nanofabrication of Plasmonic Metal Alloys with Single Nanoparticle Composition Control. *ACS Nano* **2023**, 17(16), 15978-15988.

Paper V: Andersson, C.; Theodoridis, A.; Abbondanza, G.; Fritzsche, J.; Langhammer, C. Screening Transition Metal Alloys with Single Nanoparticle Resolution for the Rational Design of Plasmonic Hydrogen Sensors. *Submitted manuscript.*

Paper VI: Klein Moberg, H. *; Theodoridis, A. *; **Andersson, C.** *; Fritzsche, J.; Nilsson, S.; Langhammer, C. A Quantitative Transformer-Augmented and Virtual-Material-Multiplexed Plasmonic Hydrogen Sensor for Chemically Deactivating Humid Air Environments. *In manuscript*. *equal contribution.

My Contribution to Appended Papers

Paper I: I designed the sample and performed the dicing, mask development, metal deposition, mask-lift off and annealing steps of the sample fabrication. I performed all hydrogenation experiments, all corresponding data analyzation and all SEM imaging (except Figure 1f-i). I wrote the first draft of the paper and the paper was finalized together with the co-authors.

Paper II: I performed the TEM imaging of fresh and hydrogen cycled Pt nanoparticles. Athanasios Theodoridis performed all optical hydrogenation experiments. Athanasios wrote the first draft of the paper and the paper was finalized together with the co-authors.

Paper III: I came up with the project idea and sample design together with Christoph Langhammer and Athanasios Theodoridis. William Colliander and Athanasios performed the sample fabrication with me and Athanasios doing the data analyzation. I performed the majority of the data analyzation of the hydrogenation measurements in varying humidities and extraction of signal descriptors with Athanasios focusing on the isotherms. Viktor Martvall have designed, structured and trained the Machine Learning models, including pre-processing the data. I wrote the first draft of the paper together with Athanasios and the paper was finalized together with the co-authors.

Paper IV: I performed the TEM and SEM imaging as well as the TEM EDX characterization. I performed the hydrogenation kinetics measurements. I wrote the first draft of the paper together with Christopher Tiburski and the paper was finalized together with the co-authors.

Paper V: I designed the samples and fabricated the alloy screening samples together with Joachim Fritzsche performing the EBL step. I performed all optical hydrogenation experiments and electron microscopy. Athanasios Theodoridis fabricated the Hole-Colloidal Lithography samples, where I performed the optical hydrogenation experiments. I performed the QMS measurements and wrote the data analyzation code together with Giuseppe Abbondanza. I wrote the first draft of the paper and the paper was finalized together with the co-authors.

Paper VI: Sara Nilsson built the experimental setup and designed the samples together with me, Athanasios Theodoridis and Christoph Langhammer. Sara, Athanasios and Joachim Fritzsche fabricated the samples. I have been part of structuring and planning the experimental measurements together with Athanasios. Henrik Klein Moberg have designed, structured and trained the Machine Learning models, including pre-processing the data. I wrote the first draft of the paper together with Athanasios and Henrik and the paper was finalized together with all co-authors.

Related Publications Not Included in The Thesis

Altenburger, B.; **Andersson, C**.; Levin, S.; Westerlund, F.; Fritzsche, J.; Langhammer, C. Label-Free Imaging of Catalytic H_2O_2 Decomposition on Single Colloidal Pt Nanoparticles Using Nanofluidic Scattering Microscopy. *ACS Nano* **2023**, 17 (21), 21030-21043.

Darmadi, I.; Piella, J.; Stolas, A.; **Andersson, C.**; Tiburski, C.; Moth-Poulsen, K.; Langhammer, C. Plasma cleaning of cationic surfactants from Pd nanoparticle surfaces: implications for hydrogen sorption. *ACS Applied Nano Materials* **2023**, 6 (10), 8168-8177.

Table of Contents

1 Introduction

The global use of hydrogen, is expected to experience a five-fold increase in usage between year 2020 and 2050 by the International Energy Agency (IEA).[1] Hydrogen is a gas that is not only highly explosive when the concentration in the atmosphere locally exceeds ~4%, but which also has been reported to likely have a negative climate impact if too much is released into the atmosphere.[2-5] The increased usage of hydrogen, combined with the risks to both people, infrastructure and the global warming targets, implies that developing means to limit leaks and overall emissions of the gas is imperative for hydrogen to reach its highest potential as an alternative energy vector to fossil fuels. To this end, the development of fast, reliable and cost-efficient hydrogen sensors has attracted considerable attention in recent decades, as demonstrated by an extensive focus from both the research community[6-9], national regulatory authorities[10,11] and industry.[12-14]

Nonetheless, hydrogen sensing is a not a new subject, and from a materials perspective, the use of Pd, Pt or alloys thereof, either directly as the active sensing element or as a hydrogen adsorbing / dissociating catalyst layer, has been well-established in the hydrogen sensing field since at least the 1970s.[15] However, in the last three decades, sensor design has become increasingly focused on nanostructured sensing elements, as their small size with large surface-to-volume ratio enables both high sensitivities and unprecedented response times.[7,16] Indeed, in recent years, novel nanostructured hydrogen sensors using Pd- or Pt-based materials have demonstrated sub-second response times[17-20], parts-per-billion detection limits[17,21,22] and stable response over seven orders of magnitude hydrogen pressure.[19]

However, despite this recent progress in hydrogen sensor development, there are still areas where even state-of-the-art nanostructured sensors struggle. One of these is operation in chemically complex environments, which for most hydrogen sensing technologies include conditions that are common for a sensor deployed in ambient conditions, e.g. elevated humidity levels or CO- and NO_x-rich urban air. Indeed, most of the breakthroughs previously listed have been demonstrated in "ideal" conditions, e.g. in vacuum or in inert backgrounds of Ar or N_2. The reason why essentially all hydrogen sensors struggle in more realistic conditions is that many molecular species present in the atmosphere, e.g. O_2, CO, H_2O and NO_x, adsorb competitively on the surfaces of the active sensing elements, limiting the senor's response to hydrogen by "poisoning" these surfaces via the blockage of hydrogen adsorption and dissociation sites.[6,7,23-28]

In addition to the poisoning issue, nanostructured state-of-the-art hydrogen sensors would benefit from enhanced stability, in particular during long-term cycling with hydrogen. Hydrogen can alter the structure of many solids during long-term exposure, where the most well-known example thereof is hydrogen embrittlement. In this failure mechanism, which affects many technologically relevant, macroscopic metals and alloys, e.g. most types of steel[29], long-term exposure to hydrogen leads to the nucleation of high densities of dislocations in the lattice of the metal, leading to a drastic reduction of the metals' strength. In contrast, for nanosized Pd, e.g. thin films[30] and nanoparticles[31,32], it has been demonstrated that the effects of long-term cycling with hydrogen instead can resemble that of thermal annealing, e.g. coalescence of individual nanocrystals into larger grains[31] and annihilation of dislocations at the surface of the structure[30,32,33] – in stark contrast to traditional hydrogen embrittlement. The annihilation of

dislocations is especially important since defects are integral for fast absorption of H into interstitial lattice sites of a hydride forming metal due to their favorable energetics[31,34,35], which is the key sensing mechanism for most Pd-based hydrogen sensors.

Taken together, hydrogen sensing research has experienced some impressive breakthroughs in recent years, but to fully commercialize and deploy these new technologies, many problems still need to be overcome[36], where the main two targets are an increased stability towards long-term hydrogen cycling and an enhanced resistance to common poisoning species. In this thesis, the first aim is consequently to improve the stability of Pd- and Pt-based nanostructures, which in thesis generally are in the form of disks with a diameter of ∼100 nm and a height of ∼30 nm, to long-term exposures of hydrogen. The second aim is to investigate methods and materials for enhanced poison resistance, specifically towards CO and NO_x, of Pd- and Pt-based hydrogen sensors, mainly facilitated through alloy screening including these two metals.

In **Paper I** we start the investigation of hydrogen cycling stability on a relatively fundamental level with pure Pd and study the morphological evolution of both pristine and systematically deformed Pd nanoparticles during long-term hydrogen cycling. Pd forms a hydride, a phase with different properties than metallic Pd, at exposures to hydrogen over a critical density. In this study, we find a strong intrinsic link between the hydride phase-transition pressure and degree of deformation of the Pd nanoparticles, as well as between the evolution of hydrogen sorption kinetics and single-particle specific defect networks.

In **Paper II**, we shift focus to Pt and specifically the interaction of Pt with hydrogen in high humidity environments. We here develop a catalytic-plasmonic hydrogen sensor that demonstrates an *enhanced* sensitivity to hydrogen at *high* humidities. This is in stark contrast to most other hydrogen sensing technologies, where high humidities generally results in decreased sensitivity.

In **Paper III**, we consequently combine Pd and Pt to channel the strengths of both systems, i.e. the benefits of hydride-forming Pd, which performs well in dry conditions, with the Pt-based catalytic sensor of **Paper II** that works best in humid conditions, resulting in a dual sensor architecture which exhibits a strong response to hydrogen over the full range from 0 to 80% relative humidity.

Having established the complementary properties of the combined Pd-Pt system, we broaden our scope with even more Pd- and Pt-based alloys. To this end, in **Paper IV** we present a new nanolithography fabrication method that, together with optical dark-field nanomicroscopy, enables the study of the hydrogenation characteristics of dozens of Pd- and Pt-based alloys, each consisting of hundreds of individual nanoparticles, simultaneously and with single-particle resolution.

This concept is utilized in **Paper V**, where we simultaneously screen the hydrogenation characteristics of 21 different Pd- and Pt-based alloys, with a specific focus on long-term cycling stability and performance in complex chemical backgrounds rich in NO and CO. We identify a with particularly favorable properties in the ternary $Pd_{70}Au_{20}Pt_{10}$ alloy. A prototype sensor chip of this alloy, when compared to an equivalent, state-of-the-art PdAu

sensor, demonstrates more than an order of a magnitude faster response to hydrogen in heavily contaminated NO backgrounds.

In **Paper VI**, we combine the insights gained from the previous studies and design a low-cost, multiplexed sensor platform utilizing 7 different transition metal-based sensor systems, all rationally chosen due to their high hydrogen sensing performance in a specific, technologically relevant condition. The convoluted signal from this sensor is subsequently treated with a transformer-based deep learning algorithm, enabling a sensor system that accurately quantifies hydrogen concentrations in a simulated metropolitan area with high humidity levels and poor air quality, which simultaneously track the concentrations of air pollutants, such as CO, NO and CO_2.

This thesis is partly based on the author's licentiate thesis.[37]

2 State-of-the-art Hydrogen Sensing

To introduce the concepts of Pd- and Pt-based hydrogen sensing materials, we will here start with a brief overview of current state-of-the-art hydrogen sensing principles. In the first section, the focus is on optical, nanoparticle based plasmonic hydrogen sensors – a type of sensor with intense research focus but which recently also took its first steps on the global market.[12] The reason for the specific focus on this sensor type is that I use the basic concept from this field, i.e. following the optical response from individual, as well as arrays of, nanoparticles to probe the intrinsic hydrogenation properties of different Pd- and Pt-based sensing materials in this thesis. In the following section, we will also briefly touch on other sensor principles to demonstrate that the materials investigated here (Pd, Pt and Pd-alloys) are relevant for many of these other sensor types as well.

2.1 Localized Surface Plasmonic Resonance Sensors

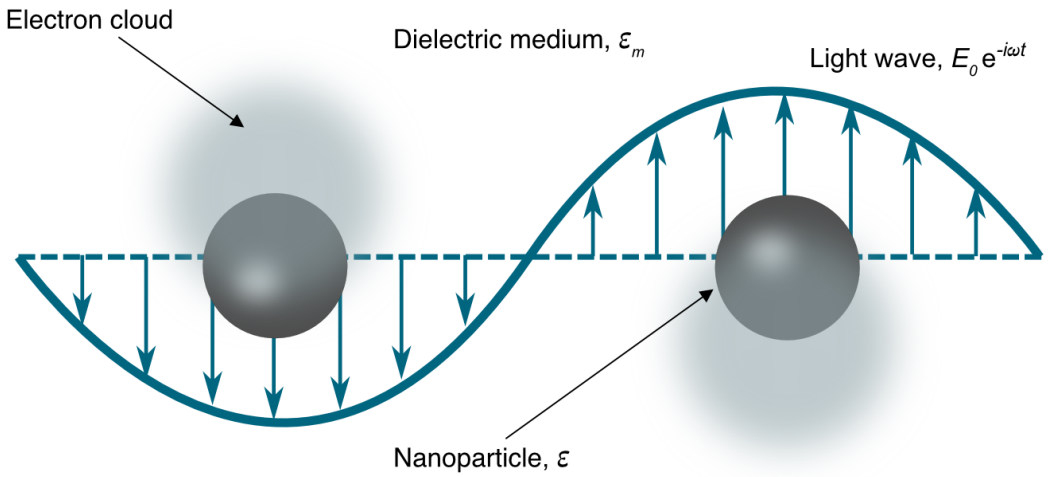

Figure 1. Localized surface plasmon resonance (LSPR) of metallic nanoparticles in the quasi-static approximation. A propagating light wave leads to a collective and synchronized oscillation of the electrons in metallic nanoparticles.

A localized surface plasmon resonance (LSPR) is a non-propagating collective oscillation of the electrons in a metallic nanostructure induced by an oscillating electromagnetic field, e.g. light (Figure 1). The key to this effect is that the nanostructure should be of comparable size or smaller than the wavelength of the inducing light, e.g., a nanoparticle in the case of optically visible light. With this assumption, one can approximate the electromagnetic field as spatially constant over the entire volume of the nanoparticle. This assumption is at the core of one of the simplest models of LSPR, the quasi-static approximation of a spherical nanoparticle (Figure 1).[38] In this approximation, a spherical nanoparticle with radius r and dielectric function ϵ embedded in a dielectric medium ϵ_m is exposed to plane-wave illumination of strength in the form of

$$\boldsymbol{E} = E_0 e^{-i\omega t}\hat{\boldsymbol{z}} \tag{1}$$

where E_0 is the amplitude of the electric field, ω is the angular frequency of the field and t is the time. This model leads to cross-sections for the scattering and absorption of light by the nanoparticle that can be written as:

$$C_{sca} = \frac{8\pi}{3} k^4 r^6 \left| \frac{\epsilon - \epsilon_m}{\epsilon + 2\epsilon_m} \right|^2 \tag{2}$$

$$C_{abs} = 4\pi r^3 \mathrm{Im}\left(\frac{\epsilon - \epsilon_m}{\epsilon + 2\epsilon_m} \right) \tag{3}$$

where k is the wave number of the electric field.[38] The quasi-static approximation has limited use for practical applications, e.g., since real particles rarely are perfectly spherical nor are they generally embedded in a fully isotropic dielectric. Nonetheless, the model still introduces the importance of the Fröhlich condition, namely that both the scattering (C_{sca}), absorption (C_{abs}) and extinction ($C_{ext} = C_{sca} + C_{abs}$) experiences a resonance when the denominator of $\epsilon + 2\epsilon_m$ approaches 0. Consequently, a shift of either the dielectric function of the particle, ϵ, or the surrounding medium, ϵ_m, due to, e.g., H_2 exposure will lead to a shift of this resonance condition and can be used to probe to hydrogen concentration of the particle environment. This is the fundamental principle of plasmonic hydrogen sensing.

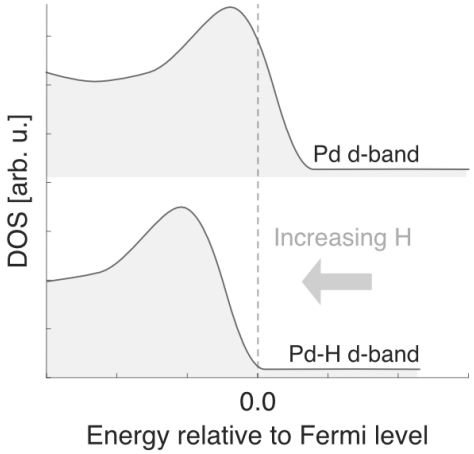

Figure 2. Schematic representation of the modification of the Density of States (DOS) for Pd when absorbing hydrogen. The absorption process has the effect of filling the Pd d-band and shifting its center down and away from the Fermi level.[39,40]

A key material for my work whose dielectric function is modified by hydrogen exposure is palladium (Pd). Pd is a metal that is highly efficient in absorbing hydrogen, which above a certain concentration transforms into as so-called Pd hydride (more on this in chapter 4.1). This hydride formation is concomitant with the formation of Pd-H bonds and an expansion of the Pd crystal lattice. Together, these effects lead to a filling of the Pd d-band and corresponding change of the density of states (DoS) (Figure 2)[39-41], which results in a modification of both the real and imaginary parts of the dielectric function for the system (Figure 3).[39,41-43] This modification of the dielectric function, as modeled by first-principle density functional theory (DFT)[39] calculations and measured experimentally[43], is in the form of a rigid shift to lower energies of the real part (Figure 3a), leading the Fröhlich condition to be satisfied at lower energies, and a magnitude decrease for the imaginary part (Figure 3b), decreasing the energy absorbed by the metal hydride.

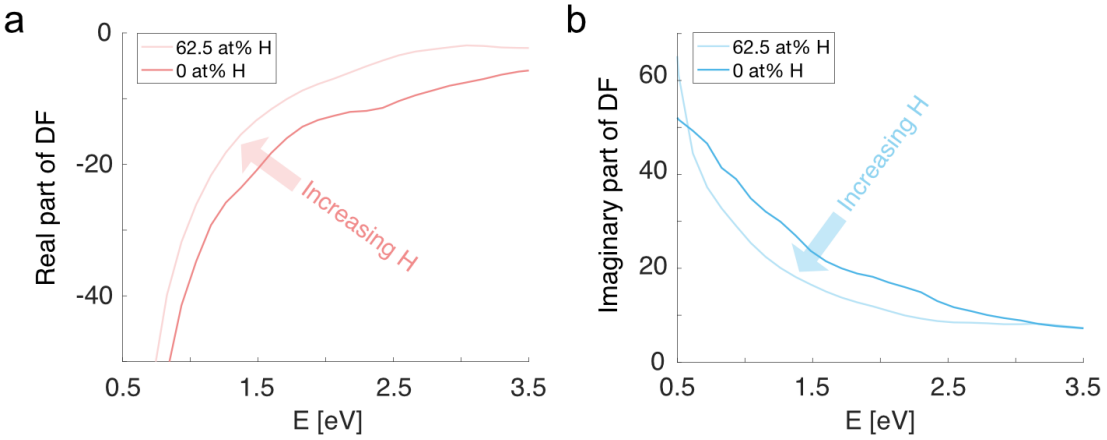

Figure 3. Real (a) and imaginary (b) parts of the dielectric function (DF) of the Pd system at 0 at% H (blue) and 62.5 at% H (red) Pd-H. This hydrogen concentration of 62.5 at% corresponds to the approximate H concentration of β-phase Pd-hydride.[44-46] Dielectric functions are from Ekborg-Tanner *et al.*[39]

To model the LSPR scattering, absorption and extinction cross section of a non-spherical Pd nanoparticle, e.g. a disk-shaped particle (the geometry used for all nanoparticles in this thesis), we have to consider more advanced models, e.g. the still analytical Modified Long Wavelength Approximation (MLWA)[47] or Finite-Difference Time-Domain electrodynamic simulations (FDTD).[39] Using the MLWA to describe a nanodisk with a diameter of 160 nm, with the DFs for Pd and Pd-H depicted in Figure 3, a clear red-shift and magnitude decrease of the plasmonic peak after hydrogen absorption is observed (Figure 4). Since the overall change of the plasmonic peak consists of both a spectral red shift and an amplitude decrease in the visible spectral range, this means that both the spectral peak shift and changes in total extinction and/or scattering intensity can be used to effectively probe the hydrogen concentration around a Pd nanoparticle via the corresponding

absorption of hydrogen into the particle, leading to multiple different read-out options for a Pd nanoparticle-based optical hydrogen sensor.[48]

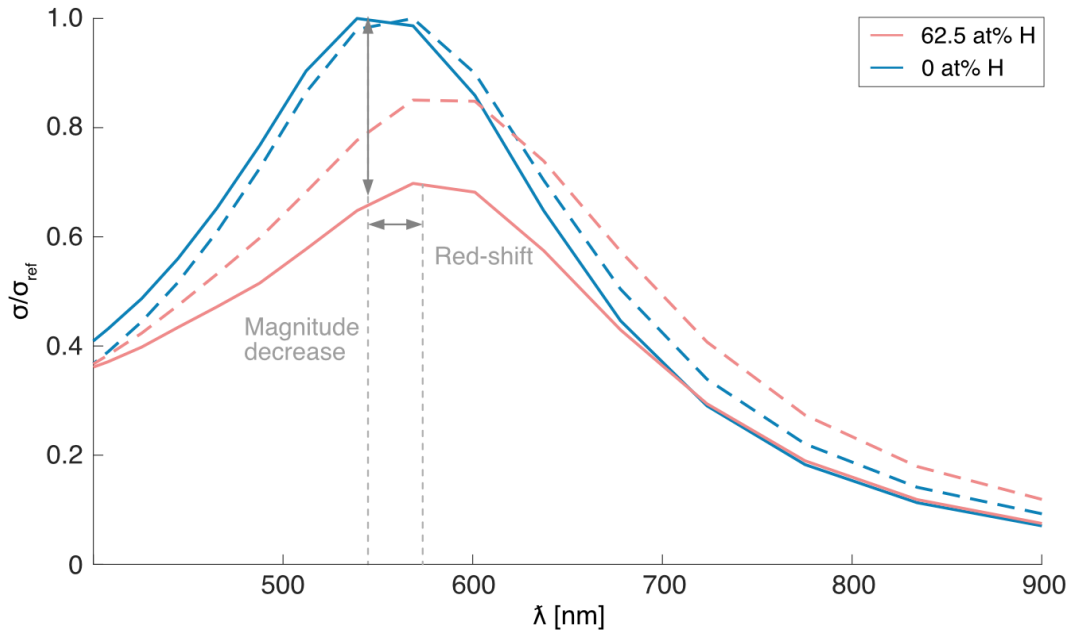

Figure 4. Plasmonic scattering (solid lines) and extinction (dashed lines) cross sections calculated for a Pd nanodisk with a diameter of 100 nm and a height of 20 nm at 0 at% H (blue) and 62.5 at% H (red) using the MLWA analytical model. The scattering and extinction cross sections are normalized to the corresponding cross section at 0 at% H (σ_{ref}). This hydrogen concentration corresponds to the approximate H concentration of β-phase Pd-hydride.[44-46] The cross-sections $C_{sca} = \frac{k^4}{6\pi}|\alpha|^2$ and $C_{abs} = k\mathrm{Im}(\alpha)$ were calculated using the MLWA modified polarizability for an oblate spheroid as introduced by Kelly *et al.*[38,47] Evidently, absorption of hydrogen leads to a magnitude decrease and a red-shift of both the scattering and extinction LSPR peaks. Dielectric functions are from Ekborg-Tanner *et al.*[39] and depicted in Figure 3.

Pd-based LSPR nanoparticle sensors have demonstrated the ability to reach ppb-levels limits of detection[21], enable safe and remote sensing by optical fiber deployment[49] and facilitate fast and reliable response over several orders of hydrogen concentrations.[18,19,50-52] Consequently, this type of sensor has been described as one of the best options to eventually meet the performance targets for hydrogen safety sensors set by global stakeholders, e.g. the U.S. Department of Energy (US DoE).[7] However, Pd has some serious drawbacks, namely that it is easily poisoned by molecular species common at trace amounts in ambient air, such as CO, NO_x and H_2O (more on this in section 4.2.3). Alleviating this problem for Pd-based nanoparticle sensors is therefore the focus of **Paper III**, **V** and **VI**.

As an alternative to using direct changes of the dielectric function, ϵ, of the active sensing material as the signal transducing mechanism in a plasmonic hydrogen sensor, one can also indirectly probe hydrogen concentrations by measuring a change of the dielectric function of the surrounding medium, ϵ_m, induced by hydrogen. This sensing mechanism forms the basis for the Pt-based catalytic-plasmonic optical hydrogen sensors the we introduce in **Paper II**,[53] as well as is used in **Paper III**, **V** and **VI**. It works on the basis that in ambient air, which in most conditions is rich water vapor in addition to high O_2 levels, Pt nanoparticles exposed to H_2 experience both a hydrogen mediated reduction of surface adsorbed oxygen species, leading to a shift of the free electron density of the Pt particle (and thus a change in its ϵ), and the evaporation of adsorbed H_2O layers due to the highly exothermic hydrogen-oxidation evolution reaction (HOR) taking place on the Pt surface (which changes ϵ_m).[53] In combination, the induced changes in ϵ and ϵ_m result in an H_2-induced spectral blue shift of the Pt plasmonic peak.[53]

A priori, it is not clear how many H_2O molecules that is needed on a surface for the water to optically respond as "bulk" water with a dielectric constant of $\epsilon_m = 1.7$. However, combined molecular dynamics and snapshot *ab initio* calculations has demonstrated that a 5 Å water layer on Pt is enough to reach a dielectric constant of $\epsilon_m = 1.7$.[54] This combined with the spatial extension of the enhanced field from the nanoparticle surface of a single Pt-like nanoparticle being on the order of ~100 nm,[55] lead to an effective dielectric medium where ϵ_m is expected to vary as a function of the water layer thickness. In **Paper II**, we have corroborated this effect by FDTD simulations of Pt nanoparticles covered by varying water layers from 0 to 5 nm, which revealed distinct shifts of the plasmonic peak position of up to ~20 nm.[53] In Figure 5, a bit more qualitatively, this phenomenon is also modeled with MLWA, by assuming $\epsilon_m = 1.7$ to indicate a very thick water layer and $\epsilon_m = 1.0$ for an extremely thin or absent water layer. Doing so reproduces the trend of more blue-shifted scattering and extinction plasmonic peaks in the absence of H_2O on the surface (Figure 5).

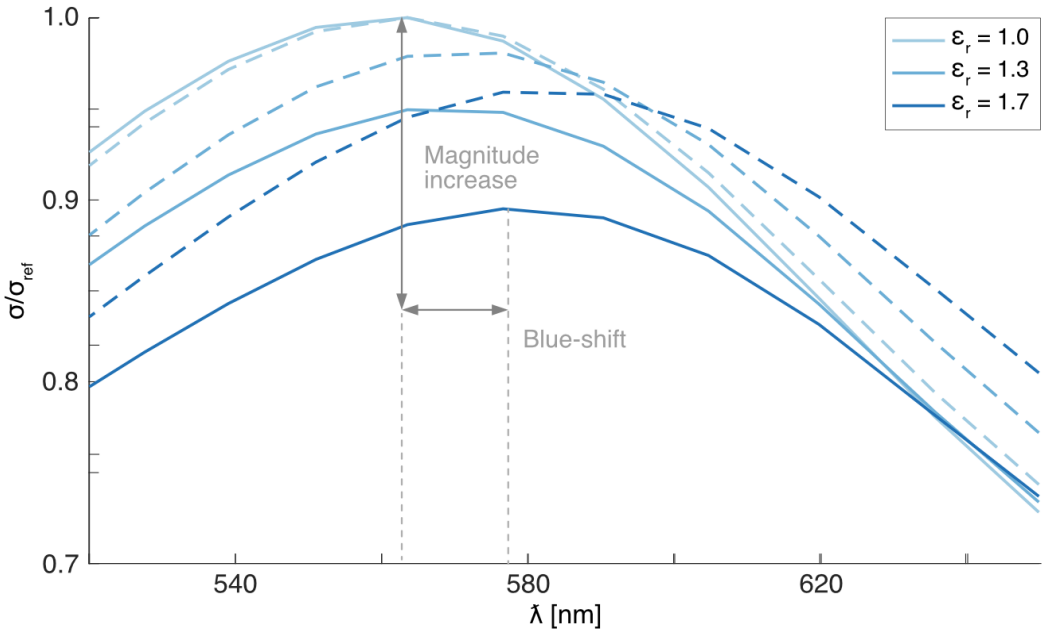

Figure 5. Plasmonic scattering (solid lines) and extinction (dashed lines) cross-sections for a Pt nanodisk with a diameter of 100 nm and a height of 20 nm, modeled as oblate spheroid in the MLWA framework for the real part of the surrounding dielectric medium, ϵ_m, varying from 1.0 to 1.7 to represent different H_2O layer thicknesses. The scattering and extinction cross sections are normalized to the corresponding cross section at $\epsilon_m = 1.0$ (σ_{ref}). The imaginary part of the dielectric function for H_2O is negligible at visible light wavelengths.[24] Evidently any evaporation of water layers ($\epsilon_m \rightarrow 1.0$) leads to an overall increase in extinction and scattering, and a blue-shift of both peaks. Dielectric functions for Pt are taken from Rahm *et al.*[25]

The catalytic Pt sensor is the main focus of **Paper II**, and is also employed in **Paper III**, **V** and **VI**.

2.2 Other Types of Hydrogen Sensors

Beyond optical nanoparticle-based hydrogen sensors, there exist numerous other types of sensors both on the commercial market and in active research and development. Despite using many different types of sensing readout technologies, e.g. thermal conductivity[6,8], electrical resistance[8,9,56,57] or acoustic oscillations[8,58-61], most hydrogen sensors use similar active sensing materials, e.g. Pd or Pt. This is due to these materials', from a sensing perspective, favorable reactions with hydrogen, e.g. reversible hydrogen absorption (Pd) and hydrogen oxidation reaction (Pd, Pt), both which I will discuss in more detail in chapter 4 – combined with their relative stability toward other gases, e.g., oxidation from atmospheric O_2. However, and most importantly for the general use of Pd and Pt in hydrogen sensing, is that both metals can facilitate the (exothermic) dissociation of H_2 molecules into monoatomic H on their surfaces, a key reaction step for most of the sensor technologies that I will discuss below. Due to this reliance on similar active sensing materials, e.g. Pd and/or Pt, I will in the following section briefly discuss different hydrogen sensor types to demonstrate that they face similar problems in terms of response times, chemical deactivation, etc. – irrespective of their sensing readout methodology.

Thermal conductivity gas sensors, i.e., sensors that measure the change in heat loss when exposed to gases with different thermal conductivities compared to air, have been in use in one way or another for the last 100 years.[6] Despite being a robust technique that is widely commercially available, traditional thermal conductivity sensors have some major drawbacks. For example, due to the difficulties of resolving small temperature changes in background thermal noise, thermal conductivity

sensors are generally not efficient in measuring small concentrations of H_2.[6,8] Also, if no hydrogen specific filter is used, thermal conductivity sensors are inherently cross-sensitive to other gases that, like H_2, have different thermal conductivities compared to air, e.g. He, Ar, CH_4 and CO.[6] Consequently, despite their effectiveness as general gas detectors, their potential as quantitative gas sensors that effectively can classify different kinds of gases and their concentrations is limited.[26]

Up until 2010, the most widely available sensor type on the market for H_2 *specific* gas sensing, i.e., sensors that are designed to primarily react with and detect H_2, was reported to be electrochemical hydrogen sensors.[62] The general working principle of this type of sensor is to use two electrodes immersed in electrolyte (sometimes a third reference electrode is used as well), and then dissociate and oxidize H_2 molecules on the working electrode, resulting in a proton and an electron per H atom. For the electrode materials, different material combinations of Pt are common choices due to Pt's ability to effectively dissociate the H_2 molecule.[8,62-64] After oxidation, the proton is transported through the electrolyte to the counter electrode, and the hydrogen concentration is inferred from either the current (closed circuit operation) or potential (open circuit operation) between the working and counter electrode. However, the reliance on diffusion of the proton through the electrolyte leads to this type of sensor generally having relatively slow response times.[8,62] Additionally, the harsh environment that most electrolytes provide lead to deterioration of the electrodes and short operating lifetimes.[8,62] Consequently, in a review from 2024 covering most current types of hydrogen sensors by Swager *et al.*, it was concluded that "recent research has largely focused on alternative [hydrogen sensing] modalities, particularly chemiresistive H_2 sensors".[8]

A chemiresistive sensor is also an electronically based, but instead of using an electrode-electrolyte based system as an electrochemical sensor, the hydrogen concentration of the environment is directly inferred from a resistance change of the active material. This active material is often a hydride forming metal, e.g. Pd or Pd-alloys, or a metal oxide semiconductor (MOS).[8,9,57,65,66] In the case of Pd, the hydride form has a higher resistance than metallic Pd, but the volumetric expansion associated with the hydride formation (more on this in chapter 4) often leads to the physical deterioration of the macroscopic sensing element if this is exclusively made of a hydride forming metal.[8] A way around this, which generally also lead to faster response times, is to nano-size the hydride forming metal and put it on / in a carbon support structure, e.g. carbon nanotubes.[8,57] The carbon structure then acts as a probe to the changing electronic properties of the nano-sized hydride. However, since most of these sensors are based on hydrogen-interacting sensing materials like Pd, they are consequently also prone to the drawbacks of these materials, e.g., easily poisoned by molecular species common in ambient air at trace amounts, such as CO, NO_x and H_2O (more on this in chapter 4).

For MOS-based sensors on the other hand, the sensing mechanism is generally based on H-induced reduction of surface oxides, leading to either an increase (p-type) or decrease (n-type) of the resistance in the semiconductor.[8,62] MOS-sensors are relatively easy to fabricate, effective at reaching low limits of detection in air (at least in clean air without any additional detrimental molecular species like H_2O, CO etc.) together with comparably fast response times.[8] However, their dependence on surface adsorbed oxygen also leave them vulnerable to other surface adsorbing

species, e.g. H_2O. Additionally, this dependence also means that filter materials like polymethyl methacrylate (PMMA) are less useful for this sensor type since oxygen effectively reaching the surface is integral for the sensor operation.[8]

Finally, optical micromirrors[8,67,68], fiber Bragg gratings[8,69,70], acoustic resonators,[8,58-61] as well as catalytic thermal sensors[53,71-73] are other types of sensors with a strong research focus, all of which generally use Pd, Pt or their corresponding alloys as active sensing material.[53,58-61,67-70,72,73] To this end, it is clear that these materials are not only important for LSPR-based sensors, but for most types of technologically relevant hydrogen sensors.

3 Physical Metallurgy

In this chapter, I will review some concepts of physical metallurgy, a research field which deals with relating the microstructure of metals and alloys to their physical properties. Some of the concepts discussed in this chapter are based on the properties of *macroscopic* metals and may therefore not completely apply to the nano-sized systems discussed in this thesis. Nonetheless, these concepts still serve as a foundation for how the internal structure of metallic nanoparticles affects their individual physical and chemical properties, e.g., the diffusivity of hydrogen through a metal, which is discussed in more detail for Pd specifically in section 4.1.2. The first section of this chapter delves into the different types of defects and how these affect the mechanical strength and diffusion properties of a metal. In the second section, I will briefly discuss different phases of metals and explain two different types of phase transitions that will be important for the Pd-H system in chapter 4. Finally, in the last section, I will introduce the concept of alloying and discuss the systems used in this thesis.

3.1 Defects in Metals

Many of the physical properties of metals (and other crystalline materials) can be directly or indirectly related to their crystal lattice. This includes plastic deformation properties, e.g. slip planes[74,75], diffraction and radiation scattering properties, e.g., Bragg diffraction[74] as well as electronical properties, e.g., the density of states for electrons in a material.[74] The discussion of these concepts often start with an infinite and defect-free crystal lattice for the corresponding material. However, real crystals generally contain different types of defects. These imperfections have profound effects

on the physical and chemical characteristics of the material, such as mechanical strength[76] and solute diffusivity[34,77]. Indeed, defect engineering, e.g., by work hardening, has been a staple in metallurgy for thousands of years[78], with contemporary examples including efforts to produce gradient nanostructuring.[79] In this section, I will introduce some basic defect types, including point defects, edge and screw dislocations, as well as grain boundaries.

3.1.1 Point Defects

Point defects are imperfections resulting from either the addition or removal of a single atom into/from the crystal lattice. The two most important point defects in this thesis are interstitials and vacancies.

An *interstitial* is an addition of an extra atom in between the ordinary lattice sites of the host metal, introducing strain by displacing the host atoms from their equilibrium positions in the process (Figure 6a). Consequently, interstitials increase the global stress-levels of the material.[76] In the context of this thesis, the absorption of hydrogen into Pd-based alloys will be the most discussed form of an interstitial. The stress induced by the H atom on the Pd lattice is the key contributing factor to the α-to-β phase transition of Pd-hydride, and will be discussed in detail in section 4.1.1.

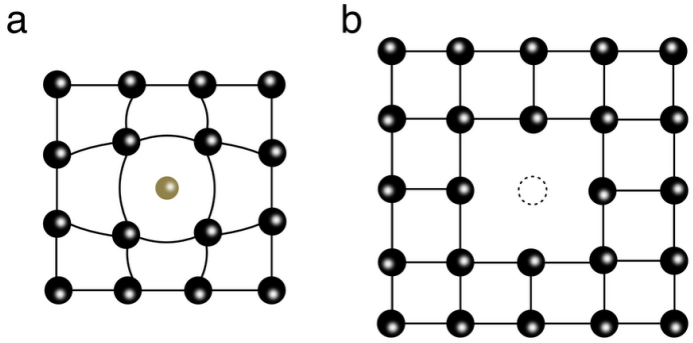

Figure 6: Schematic of an (a) interstitial and (b) vacancy defect in a crystal.

In contrast to an interstitial, a *vacancy* is an atom missing from the crystal lattice (Figure 6b). Vacancies introduce a change in entropy for the system, which at elevated temperatures generally is high enough to overcome the enthalpy of formation for the vacancy.[80] This means that for elevated temperatures, having a certain concentration of vacancies is energetically favorable for the system.[76,80] The Gibbs free energy of vacancies is

$$\Delta G = n\Delta E_v - T\left(n\Delta S_{vib} + \Delta S_{conf}\right) \tag{4}$$

where ΔS_{vib} and ΔS_{conf} is the change of vibrational and configurational entropy per vacancy respectively, n is the number of vacancies, ΔE_v is the vacancy energy of formation, k is the Boltzmann constant and T is the temperature.[76] Assuming that the number of vacancies is small compared with the total number of atoms in the solid, N, i.e. $n << N$, the equilibrium concentration of vacancies in a solid, X_v, is expected to follow the relation[76,80]

$$X_v = \mathrm{e}^{-\frac{\Delta S_{vib}}{k}-\frac{\Delta E_v}{kT}} \quad (5)$$

The most important feature of vacancies in the context of this thesis is that they aid the diffusion of atoms through the lattice.[76] This is due to the vacancy substantially lowering the energy for site-hopping of atoms through the lattice and consequently increasing the diffusivity in the solid.[76] Indeed, many solid-state diffusion models are predicated on the existence of vacancies.[81] For hydrogen however, as an interstitial, vacancies are not necessary for diffusion, but the vacancies will influence the hydrogen absorption process by acting as hydrogen sinks (more on this in section 4.1.2).

3.1.2 Dislocations

Dislocations are a one-dimensional type of defect, meaning that they consist of entire rows of displaced or otherwise anomalously arranged atoms. Accordingly, they are also called *linear* or *line* defects. The two simplest types of dislocations are *edge* and *screw* dislocations, from which all other dislocations can be constructed as linear combinations.[76] This is due to the geometrical descriptor of any dislocation, the Burgers vector, $\vec{b}$, of an edge dislocation being perpendicular to the local dislocation line $\vec{s}$ (Figure 7a), while for a screw dislocation it is parallel (Figure 7b).[76] Consequently, using $\vec{s}$ together with edge, $\overrightarrow{b_{\perp}}$, and screw, $\overrightarrow{b_{\parallel}}$, components, any other dislocation can be fully described.[76]

To visualize an edge dislocation, we can imagine an extra half crystal plane inserted into the lattice. For example, if we over a distance x beneath the

dislocation have 6 atoms, at the dislocation (and all rows above it) we instead have 7 atoms along the same distance x (Figure 7a). For a screw dislocation on the other hand, one can imagine that a cut has been made partly through the lattice and that the crystal "surfaces" on both sides of this imaginary cut have been "twisted" away from each other (Figure 7b).

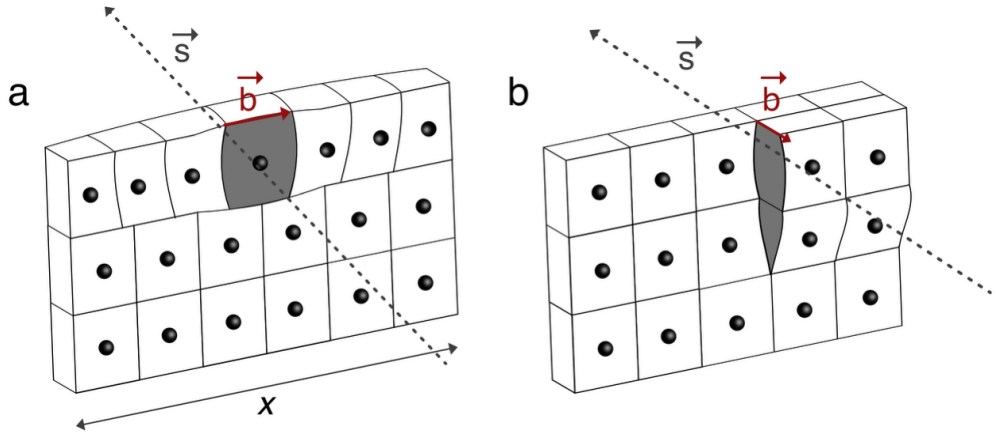

Figure 7: An edge (a) and screw dislocation (b) in a crystal plane along the local dislocation line $\vec{s}$. The Burgers vector, $\vec{b}$, for each dislocation is marked by a red arrow. The origins of the lattice misfits, the extra atoms in (a) and the lattice distortion in (b) are highlighted in grey.

Both types of dislocations, edge and screw, increase the Gibbs free energy of the system. This means that in contrary to vacancies - and in the absence of any external stress (a highly unlikely scenario in practice) - they are not thermodynamically favored at any temperature.[76] Their formation is instead generally a consequence of a stressed crystal, e.g. from mechanical work or intercalation of interstitials, leading to the formation of dislocations as a stress-relief mechanism.[76] Even for techniques routinely used to make single

crystals, such as colloidal synthesis of nanoparticles, dislocations still often form if the crystallite is large enough (more on the critical size for Pd crystallites in section 4.1.1).[82,83] In the case of nanoparticles, one of the ways to create (nearly) dislocation-free crystals is through solid-state-dewetting, a method that through the use of high temperature annealing and single crystal substrates provide the environment to form (nearly) defect-free nanoparticles.[84-88]

Having established the dislocation concept as such, it is interesting to discuss what effect dislocations have on the properties of metals. It is well-known that the critical shear strength of metals (*i.e.* the amount of shear stress that the metal can withstand before plastic deformation) is well below the theoretical strength expected from theoretically perfect crystals.[76,86] The reason for the low critical strengths is attributed to the activation of slip and plastic flow from pre-existing dislocations in the sample, or the nucleation of dislocations in geometrical "weak" spots, e.g., corners or imperfect surfaces, leading to the observed low yielding strengths of most materials compared to the theoretical maximum strength.[86,89-94] However, if the yield strength of a material initially decreases with increasing dislocation densities, there comes a turning point when the yield strength instead start to increase.[76,95] This is the basis of work hardening, where above a critical dislocation density, the numerous dislocations in a material start to impede lattice slip and plastic deformation, leading to increasing strength.[95]

Regarding the effect of dislocations on the diffusion properties through a material in general, and of hydrogen in particular, dislocations generally increase the diffusivity of H through the crystal lattice by *pipe diffusion*.[96,97] This phenomenon is due to locally reduced activation energy barriers for

diffusion in the disordered region around a dislocation.[96,97] The importance of dislocations on the kinetics of hydrogen absorption in Pd is further discussed in section 4.2.2 and in **Paper I**.

3.2 Interfaces

An *interface* in a crystal can be defined as a two (or three) dimensional region with an abrupt and significant change in the atomic ordering of the material, e.g., (i) a free surface, (ii) the interface between two materials with different crystal structures or (iii) a grain boundary.

Of these three types of interfaces, the free surface (i) is one of the most important in all of chemistry, not only due to being the interface by which a solid material interacts with its environment, but also for being a chemically highly reactive interface due to the many uncoordinated atoms at the surface. Indeed, the research field of surface science has been awarded at least four Nobel prizes[98-101] and is at the core of the field of heterogenous catalysis.[102] In the context of this thesis, the interaction of H_2 with the surfaces of Pd and Pt are thoroughly discussed in chapter 4. In addition to their interesting chemical properties, free surfaces serve as termination points for internal stress fields inside a crystal and, together with grain boundaries, as termination points for gliding dislocations during plastic deformation[76] - a concept that will be of importance during the discussion of the effects of hydrogen cycling on Pd-based nanoparticles in section 4.2.4.

The interface between two materials (ii), e.g. between a supported nanoparticle and its substrate, is another type of interface of significant importance in nanoscience, e.g. through epitaxial growth of nanostructures[103]

or by strain-induced changes in catalytic activity of nanoparticles.[83,104] This strain arises from a lattice mismatch between the support and the nanostructure, which for a hydrogen absorbing (and consequently expanding) Pd-based material can lead to very high stress levels during H absorption through substrate clamping – a concept that is further discussed in section 4.1.1 and in **Paper I**.

Finally, grain boundaries (iii) are defined as the interface between crystallites of the same phase and composition but with different crystallographic orientations. Grain boundaries are often quantified by the angle of misorientation between the facets of the crystallites in the grain boundary. If the rotation axis of the misorientation is parallel to the grain boundary face, we have a *tilt boundary* (Figure 8a). If the rotation axis of the misorientation instead is perpendicular to the grain boundary, we have a *twist boundary* (Figure 8b).

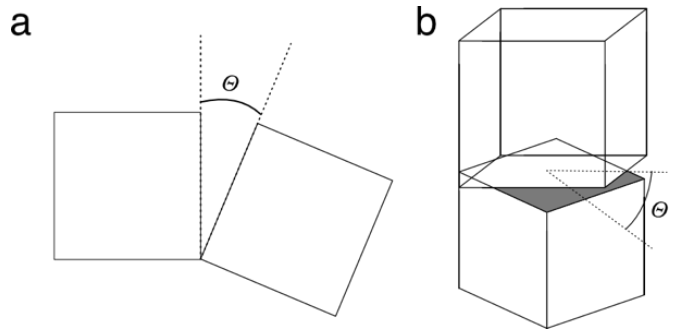

Figure 8: Schematic representation of two types of grain boundaries. (a) Tilt boundary and (b) twist boundary with θ as the misorientation angle.

We can further classify the two types of grain boundaries through the magnitude of the misorientation angle θ between the two grains (Figure 9). If $\theta > 15°$, the boundary is called a *high-angle* grain boundary (Figure 9a) and if $\theta < 15°$, it is called a *low-angle* grain boundary (Figure 9b). The high-angle grain boundaries are generally associated with more open space between the grains and a higher interfacial energy at the surface of the grains compared to their low-angle counterparts.[76,105] A twin-boundary (Figure 9d) is a special type of boundary, where the arrangement of atoms in the respective grains are mirrored along the boundary.

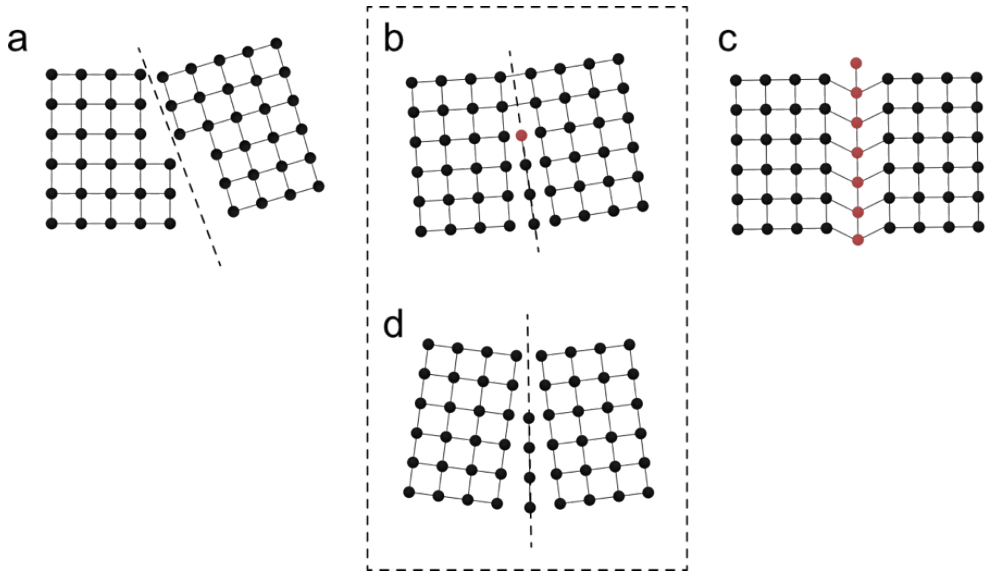

Figure 9: Different types of planar defects. (a) High-angle grain boundary (dashed line). The misorientation angle between the two grains of the boundary is $> 15°$. (b) Low-angle grain boundary (dashed line). The misorientation angle between the two grains of the boundary is $< 15°$. Low-angle grain boundaries can often be described as an array of dislocations (one dislocation highlighted as a red atom). (c) Stacking fault. A stacking fault is a special type of planar defect where the lattice points of an entire plane of atoms (red) are displaced compared to planes on either side. (d) Twin-boundary. A twin-boundary is a special type of boundary, where the arrangement of atoms in the respective grains is mirrored along the boundary (dashed line). Image adapted from Lu *et al.*[105]

Finally, as with vacancies and dislocations, grain boundaries also aid diffusion of hydrogen through the lattice.[31,76] As was the case with dislocations, the increased diffusion is generally attributed to a reduced activation energy barrier for diffusion through the grain boundary.[31,96,106] However, it should here be emphasized that due to the high degree of individuality of different grain boundaries and dislocation networks, combined with the, from a first-principle modelling point of view, large size

of grain boundary and dislocation-supporting systems, it is very difficult to provide a generalized formalism for the diffusion effects of these types of defects. Adding to this that grain-boundaries rarely are in equilibrium, but dynamically evolve as a response to their environment, further complicates the matter.[107]

3.3 Phases

A *phase* can be defined as homogeneous region with uniform crystal structure and composition, separated from other phases by interfaces across which properties change discontinuously. The most relevant example of two phases for this thesis are the α- and β-phase of the palladium-hydrogen system. The electronic differences between these two phases were discussed in section 2.1 and the enthalpy difference between the two phases will be further discussed in section 4.1.1.

The boundary between two phases in a crystal can either be *coherent* or *incoherent*. To describe the difference between the two, we will consider the two phases of the Pd-H system, α and β, with lattice parameters of 3.895 Å and 4.025 Å respectively.[108] For a coherent phase boundary, the transition from a lattice parameter of 3.895 Å to 4.025 Å is continuous (Figure 10a). This leads to increased strain in the phase boundary, increasing the Gibbs free energy of the system.[76] For an incoherent phase boundary, the atomic bonds between the two phases are "broken", e.g., by means of dislocations or grain boundaries (Figure 10b). This leads to decreased stress compared to the coherent boundary, but instead increased surface energy at the uncoordinated surface atoms at the interface.[76] Consequently, both types of phase boundaries increase the Gibbs free energy of the system, such that

which is the most energetically favorable depends on the current stress levels of the phase transition. If the stress levels of a coherent phase transition are high enough, such that the increase to the Gibbs free energy by continuing the coherent phase transition is higher than the corresponding increase to the free energy by switching to an incoherent transition (ΔG of nucleating the necessary dislocations + the increased interfacial surface energy), dislocations will nucleate to relieve the coherent stress.[109]

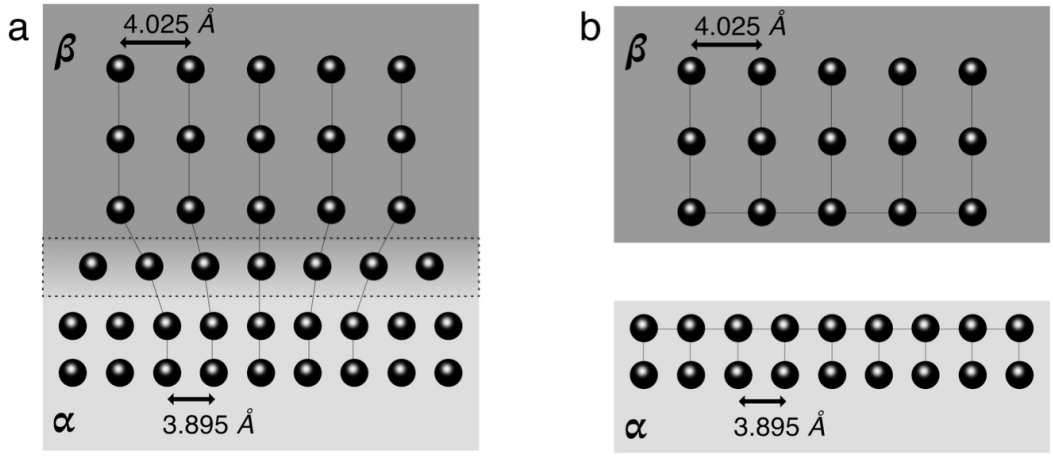

Figure 10: Schematic representing the two different types of phase boundaries between two phases α and β with different lattice parameters. (a) For a coherent phase boundary (dashed box), we have continuity between the crystal planes. This introduces stress on the boundary. (b) For an incoherent phase boundary, the atomic bonds are "broken" between the two phases, e.g., by means of dislocations or grain boundaries. This leads to decreased strain, but higher interfacial surface energies compared to (a).[76]

3.4 Alloying

Since the bronze age, alloying has been a cornerstone of metallurgy to improve and expand the physical and chemical properties of elemental metals. That many properties, e.g. the hardness of bronze[110], vary continuously with the stoichiometry of the alloyants is quite intuitive. However, there are also examples of where even minuscule additions of a second element unproportionally changes a property of an alloy, e.g. the boron hardening effect in steel[111,112], superconductive phases in $Ba_{1-x}K_xFe_2As_2$[113] and $LaO_{1-x}F_xFeAs$[114] as well as catalytic activity in dilute, single-atom-catalyst-like alloy nanoparticles.[115-117] In this thesis, I investigate the hydrogen sorption properties of Pd- and Pt-based alloys, and also for these systems, small concentrations of secondary alloyants can lead to drastically different physical and chemical properties (cf. **Paper III** and **Paper V**). The thermodynamics and kinetics of the interaction of these alloys with hydrogen will be further discussed in section 4.2. Here, I will give a more general introduction to the thermodynamics of alloying for these alloys.

First however, I will introduce two different types of atomic orderings that will be important for the continued discussion. The first is the homogenous atomic ordering where atoms of the constituent elements are randomly dispersed among each other (Figure 11a). This resembles how atoms are dispersed in a liquid, and consequently, this atomic ordering is often called *solid solution*. The other type of atomic ordering is a heterogenous ordering of separate phases. Here, long-range order exists that differentiates between the two different phases of the alloy, either in terms of composition (Figure 11b) or some other physical property, e.g., lattice parameter, as is the case with the α- and β-phase of Pd-hydride.

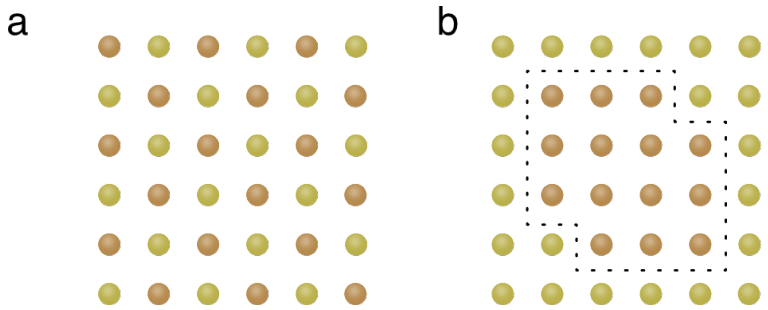

Figure 11: Two different types of atomic ordering in metallic alloys, here represented by a binary alloy of two constituent elements. (a) Homogenous ordering, also called "solid solution", in which the atoms of the two elements are randomly dispersed within each other. (b) Compositional heterogenous ordering. Here atoms of different elements have clustered together in separate phases of distinct local compositions (outlined with a dashed line). In general, the term "alloy" mainly refers to the homogenous ordering in (a), while (b) would be termed a phase-separated intermetallic phase.

Key to understanding the thermodynamics of alloys are the so-called *phase diagrams*. Phase diagrams are, in essence, maps showing the most thermodynamically stable state (i.e., the state of lowest Gibbs free energy G) of alloys under thermodynamic equilibrium as a function of different thermodynamical variables, most commonly temperature and composition for metallic alloys. A hypothetical phase diagram between the constituent elements A and B is presented in Figure 12. Here we follow the multiple phase changes that occur after having prepared an alloy of composition X_O at elevated temperature T_0 and subsequently letting it cool down to lower temperatures. We assume that we initially prepare an alloy of composition X_O at temperature T_0 (point O in the phase diagram). At this temperature the alloy is in a liquid state (L) with the constituents A and B randomly mixed

(Figure 11a) in a solution. The overall composition is X_O. We then let the system cool down, and when the temperature has dropped to T_1 (point a), the alloy separate in two phases, one solid and one liquid, such that concentration of the liquid follows the liquidus line (between L and L+S) and the concentration of the solid follows the solidus line (between S and L+S). To this end, at T_2 the thermodynamically most favorable state for the system is a liquid of composition X_b (point b), with solid phases of composition X_c (point c). The volume ratio between the liquid of composition X_b and the solid of composition X_c is such that the overall composition is still X_O. When the alloy cools further to temperature T_3 (point d), the most stable form of the alloy is now a solid solution (Figure 11a) between the constituents *A* and *B* of composition X_O. The area where the solid solution is stable is highlighted in the phase diagram as (A, B). When the alloy cools even further to temperature T_4 (point e), the solid solution is again not stable anymore. Instead, two different compositional phases are favored (Figure 11b), one of composition X_e (point e) and one of composition X_f (point f). Again, the volume ratio between the two phases is still such that the overall composition is X_O.

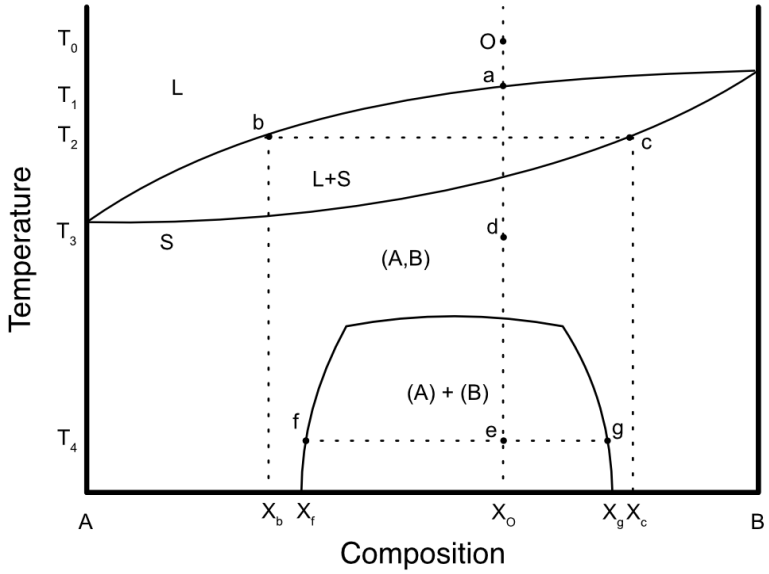

Figure 12: Hypothetical temperature-composition phase diagram for binary alloy *AB*. The dashed lines are visual guides for following the solidification of an alloy initially prepared at composition X_O at temperature T_0 (point *O*). For more information, see the main text.

Having established how to interpret these diagrams, we move on to the bulk phase diagrams for three of the alloy systems I studied in this thesis, PdPt (Figure 13a), PtAu (Figure 13b) and PdAu (Figure 13c). The PtAu system I only investigate as a part of the PdPtAu system, but to the best of my knowledge, no reliable bulk phase diagram for this ternary alloy exists. However, this is of limited consequence for our nanoalloys, as bulk phase diagrams rarely are applicable at the nano level.[118,119] The key factor for this discrepancy between bulk and nano systems, e.g. nanoparticles, is the high surface-to-volume ratio (SVR) of the latter.[118,119] The high SVR of nanosystems lead to the surface energetics between the constituent metals playing a more important role for the miscibility in the alloy than in the bulk phase, leading to not only material-, but also shape- and size-dependent

melting temperatures of the alloyants.[118,119] This has in turn led to the emergence of "nanophase" diagrams, i.e., alloy phase diagrams which consider both shape, size and material of the nanostructure in question.[118]

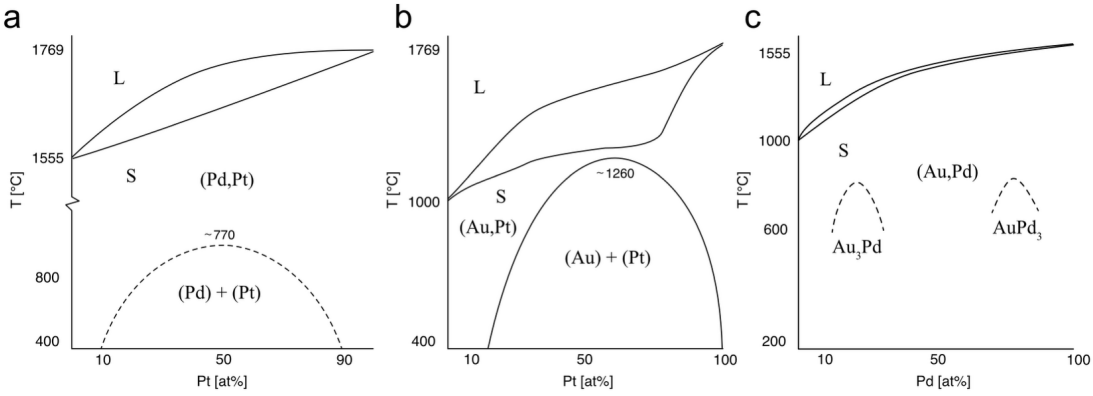

Figure 13. Binary alloy phase diagrams for (a) PdPt, adapted from Bharadwaj *et al.*[120], (b) AuPt, adapted from Okamoto *et al.*[121] and (c) PdAu, adapted from Okamoto *et al.*[122] L and S denotes liquid and solid phases respectively, while (A,B) and (A) + (B) denotes a solid solution and phase separation respectively for the constituent metals A and B.

To exemplify the difference between bulk and nanoalloys, we consider the PdPt system. In the PdPt bulk phase diagram, there is a hypothetical miscibility gap between 10-90 at% Pt below 770 °C (Figure 13a), which is generally not reproduced in nanophase diagrams, e.g., for 3-10 nm octahedral PdPt nanoparticles.[118] Instead, a number of first-principle and molecular dynamics studies have established a general thermodynamic tendency for Pd surface segregation for a multitude of different nanostructures.[119,123-125] However, despite this thermodynamic segregation argument, we note that there is substantial experimental evidence of alloying between Pd and Pt at the nano-level[126-129], albeit these alloys may be kinetically locked in a

metastable configuration rather than in a thermodynamically stable state. The key takeaway from this discussion, corroborated by the discourse regarding the miscibility of nanostructured PdPt in the literature[119,123,124,126-130], is that the miscibility of nanoalloys is highly dependent on the shape, size and morphology of every individual nanoparticle. Consequently, we should expect a high variance in alloying degree between single particles in an ensemble for certain alloy systems. This is exemplified in **Paper V**, as inferred by a significant difference in single-particle variance of the hydrogenation properties between PdPt, PdAu and PdPtAu nanoalloy systems.

4 Metal-Hydrogen Systems

The interactions of hydrogen with metals is a wide topic, with direct applications in reduction of iron ore in steel production[131], gas separation membranes[132,133], hydrogen storage[134-136], and gas sensing applications[7-9] as well as more undesired, adverse material effects, such as hydrogen embrittlement, e.g. in Zr alloys used in the cladding of nuclear reactors[137,138], in hydrogen storage tanks for fuel cell vehicles[139] and in pipelines for fossil fuel transportation.[140] As such, hydrogen can interact with metals in different ways, e.g., by weak/none to strongly (exothermic) adsorption on the metal surface – as is the case for Au and Pt respectively – all the way to full absorption into the metal lattice, eventually leading to a complete phase transformation into a metal hydride – as is the case for Pd.[23,141-144] Since the topic for this thesis is Pd- and Pt-based materials for hydrogen sensing, with a specific focus on optical nanoplasmonic sensors, we will here concentrate on the interaction of hydrogen with three different plasmonic metals: Pd, Pt and Au. Of these three, we will examine Pd in most detail as it constitutes the key building block in most commercial- and research-stage hydrogen sensing technologies.

4.1 The Palladium-Hydrogen System

The highly efficient hydrogen absorption capabilities of Pd have been well known since the mid 19th century[145], and they have been key to establishing Pd as *the* model system for metal-hydrogen interactions. The reason for the great interest in Pd is that already at ambient conditions, the metal is not only highly efficient in dissociating the hydrogen molecule, but it can also absorb the resulting monoatomic hydrogen into its metal lattice. During this

absorption process, hydrogen occupies the interstitial sites of the metal (Figure 6a), eventually forming Pd hydride – an entirely different phase of Pd-H with significantly altered lattice parameter and electronic properties compared to metallic Pd. For example, as discussed in section 2.1, the altered dielectric function of Pd hydride leads to a distinct spectral shift of light scattered from Pd nanoparticles LSPR excitation, which is the key operating principle for Pd nanoparticle based optical hydrogen sensors. Indeed, the altered physical and chemical properties of the hydride phase are the mechanistic sensing principles for essentially *all* hydride-based H_2 sensors. Consequently, the thermodynamics and kinetics of the hydride phase transformation are critical for the operation of any hydrogen sensor based on this principle.

4.1.1 Thermodynamics of Palladium Hydride Formation

At ambient conditions, it is energetically favorable for a hydrogen molecule to dissociate on a Pd surface compared to staying in the gas phase. The most stable position for the dissociated hydrogen atom is on the surface (enthalpy of ~ -0.5 eV, see Figure 14)[23,144,146-148], and the surface is therefore the first part of a Pd system to be saturated with hydrogen. Nonetheless, both the tetrahedral and octahedral interstitial sites inside the Pd crystal lattice are also energetically favorable (enthalpy of -0.1 eV and -0.2 eV respectively[109,148-150], see Figure 14) compared to gas phase H_2. Thus, there is a thermodynamic drive to not only fill the surface and subsurface sites, but the Pd bulk as well. Consequently, the surface hydrogen atoms will start to diffuse into the bulk after all surface and subsurface sites are fully occupied.

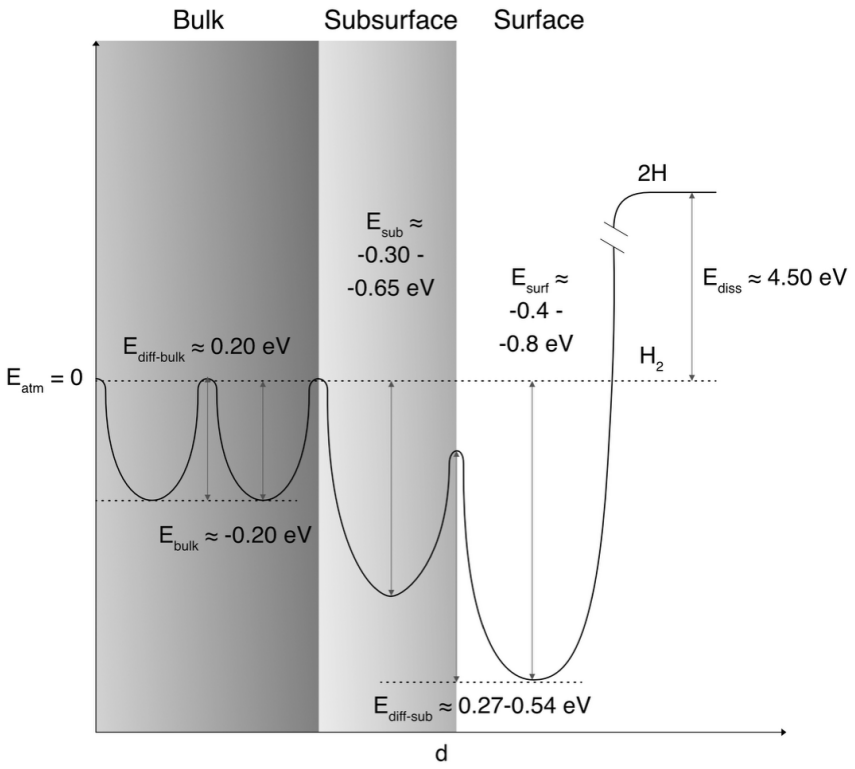

Figure 14. Energy (enthalpy) landscape encountered by a hydrogen molecule dissociating on a Pd surface and diffusing into the bulk. E_{diss} represents the change in energy between the hydrogen molecule and dissociated monoatomic hydrogen. E_{surf}, E_{sub} and E_{bulk} represent the binding energy of hydrogen at surface, subsurface and bulk sites, respectively. Energy values are compared to a hydrogen molecule in the gas phase E_{atm}.[23,144,146-149] $E_{diff-bulk}$ represents the diffusion barrier for hydrogen to diffuse from one bulk interstitial octahedral site to another while $E_{diff-sub}$ represents the rate-limiting diffusion barrier from surface to the first subsurface sites.[149,151] The higher value of $E_{diff-sub}$ is representative of the diffusion barrier at 5% compressive strain, a case that is relevant at the initial stages of β-phase hydride growth due to the compressive stress experienced by the β-phase from the surrounding α-phase.[149]

In these initial stages of the hydrogen absorption process, the hydrogen concentration in the lattice is a dilute solid solution (Figure 15a) – the Pd-H α-phase. In this phase, the Pd-H system obeys Sieverts' law,

$$n_H = \mathrm{K_S}\sqrt{p_{H_2}} \tag{6}$$

which states that the concentration of hydrogen inside the metal, n_H, is proportional to the square root of the partial hydrogen pressure p_{H_2} outside the metal and Sieverts' constant K_S.[152,153] In other words, if the partial hydrogen pressure p_{H_2} increases, more and more hydrogen will absorb into the Pd lattice. The interstitial hydrogen atoms strain the Pd lattice and increase the lattice parameter from 3.887 Å (metallic Pd) up to 3.895 Å (α-phase Pd-H).[108]

However, when the hydrogen pressure gets high enough, Sieverts' law will break down as, compared to continuing the slow, continuous increase of the α-phase absorption, it will become more favorable for the system to undergo a first-order phase transformation and drastically increase its lattice parameter (up to 4.025 Å, Figure 15a).[108] This new phase of the Pd-H system is called the β-phase (or sometimes only "Pd-hydride"). Even though the existence of this β-phase has been known since the 1920s,[154] exactly how the phase transformation proceeds has been a matter of great debate.[109,155,156] Not only can the process differ substantially between a bulk and a nano-scale system, but except for the smallest of nanoparticles, there is also sizable hysteresis between the hydrogen pressure for formation and decomposition of the β-phase in Pd. This hysteresis manifests itself as a difference in hydrogen pressure for the α-to-β phase transformation compared to the

reverse transformation (Figure 15b), where the absorption process (α-to-β) occurs at a higher hydrogen pressure than the desorption (β-to-α). The most recent theory regarding the origin of hysteresis in Pd instead involves different types of strains acting on the system during the transformation.[109,157] Different mechanisms for the hysteresis have been proposed throughout the years, e.g. that it is caused by energy losses due to the formation of dislocations during both the α-to-β transformation, as well as the reverse process.[155] However, with this explanation, it would be close to impossible to explain the reproducibility of hysteresis measured on the same system, as the formation and subsequent annihilation of equal dislocation networks time after time during repeated hydrogen cycling is highly unlikely.[157] To fully understand the α-to-β phase transition and the corresponding hysteresis, we need to systematically discuss the key interactions that lead to the phase transformation and their respective enthalpies.

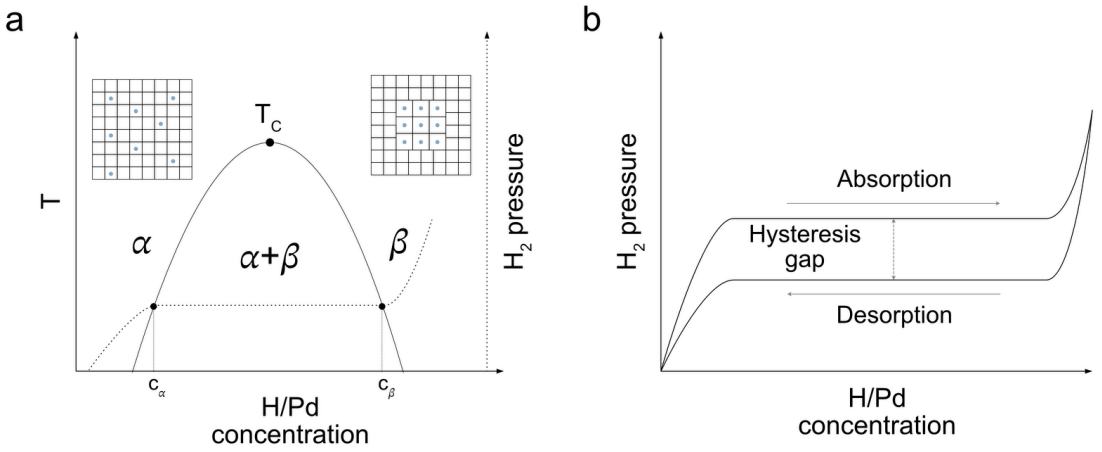

Figure 15. (a) Schematic of the bulk Pd-H phase diagram. At low hydrogen concentrations, the system is in the α-phase where hydrogen forms a dilute solid solution in the Pd lattice. As the external hydrogen pressure increase (dashed line), the hydrogen concentration in the metal increases up to the (temperature specific) critical concentration c_α. Now we enter the two-phase coexistence region where β-rich regions of concentration c_β grow at the expense of the α-rich regions of concentration c_α until the entire system has transformed to the β-phase. The area between c_α and c_β (solid line) is called the miscibility gap and decreases with increased temperature until it disappears at the critical temperature T_c. (b) Schematic of hydrogen absorption-desorption hysteresis in Pd systems. The α-to-β phase transformation occurs at a higher relative hydrogen pressure than the reverse transformation during desorption, yielding a hysteresis gap between the two sorption branches.

In hydride forming metals, the concentration (partial pressure $\frac{p_{\alpha-\beta}}{p_0}$) at which the hydride phase transformation occurs is described by the Van't Hoff equation[158]

$$ln\left(\frac{p_{\alpha-\beta}}{p_0}\right) = \frac{\Delta H}{RT} - \frac{\Delta S}{R} \quad (7)$$

where ΔH and ΔS are the enthalpy and entropy of formation, respectively, for the β-phase (α-phase) during hydrogen absorption (desorption), R is the gas constant and T is the temperature. In mean-field models of neat Pd, the enthalpy of formation for the β hydride phase consists of two terms[109]

$$\Delta H_{\beta} = \Delta H_{sol} + \Delta H_{\alpha-\beta} \quad (8)$$

where ΔH_{sol} is the enthalpy of solution at infinite dilution, i.e., very low H concentration α-phase, and $\Delta H_{\alpha-\beta}$ is the enthalpy difference between α- and β-phases. $\Delta H_{\alpha-\beta}$ in turn have four main contributions that are all hydrogen concentration, x, dependent according to:

$$\Delta H_{\alpha-\beta}(x) = \Delta H_{coh}(\mathrm{x}) + \Delta H_{attr}(x) + \Delta H_{elec}(\mathrm{x}) + \Delta H_{other}(x). \quad (9)$$

Below I will discuss these contributions in more detail.[157,159]

Coherent Strain at the Phase Boundary - ΔH_{coh}

Assuming the phase transformation proceeds coherently, i.e., the crystal lattice stays intact without any dislocation formation (see section 3.3 for the details of coherent vs incoherent phase transitions), the different lattice parameters of the α- and β-phases lead to significant stress levels in the interface region between the two phases.[157] This interphase-induced stress effectively imposes an energy barrier on the growth of either phase into the other, leading to additional work having to be exerted for *both* phase transformations, resulting in the pressure hysteresis between the two.[157] For

an open, otherwise stress-free Pd system that transforms without dislocation formation, e.g., small nanoparticles on an open surface with low friction, the total coherent stress between the α- and β-phases is volume dependent.[109,157] In other words, the larger a defect-free single crystal is, the wider the hydrogenation hysteresis will be (by way of higher absorption pressures), if no dislocations are formed in the process.[109]

However, if dislocations nucleate during the phase transformation, this volume dependent hysteresis breaks down. The reason for this is *if* dislocations can nucleate, stress can consequently be relieved from the system and a lower absorption pressure is needed for the α-to-β phase transition, leading to a smaller hysteresis. As discussed in section 3.3, it can be energetically favorable for a system to switch from a coherent to an incoherent phase transformation if the stress involved in the former grows too large, i.e. for the grains/crystals in bulk Pd.[109,156,160] This is the reason for why absorption pressures (and hysteresis) generally are lower for Pd bulk than for single, defect-free nanocrystals, e.g. in the 30-100 nm range.[109]

Nonetheless, the specific size a crystallite needs to have to reach this critical threshold has been highly debated.[109,156,160] It is well established that for macro-scale bulk Pd the grains are large enough to transform incoherently, i.e. dislocations are formed to relieve stress during the phase transformation.[161] For nano-scale systems like single-crystalline nanoparticles on the other hand, different critical regimes of ~40 nm up to 300 nm have been reported.[109,156,160] The discrepancy in the reported values for the critical size for Pd nanoparticles has been attributed to which model that is used to describe the spatial growth of the β-phase. If one assumes that the β-phase grows from the (entire) surface of the particle and inwards (a

core-shell structure, Figure 16a), a smaller critical size for the crystals will follow compared to if one assumes that the β-phase grows as a "cap", *i.e.* from one end of the nanoparticle to the other (Figure 16b).[156,160,162,163] For the particle size used in all studies for this thesis, i.e. disk-shaped particles with a diameter in the 150-200 nm and a height of ~30 nm, they are large enough to support dislocations, as discussed in **Paper I**.

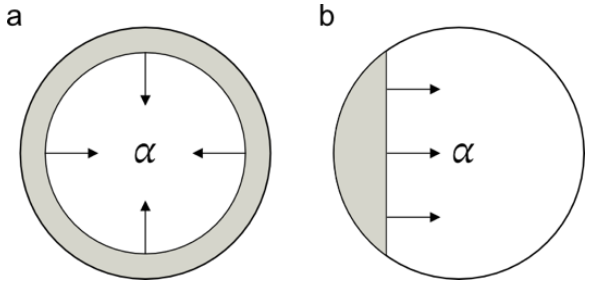

Figure 16. Schematic depicting the (a) "core-shell" vs the (b) "cap" model of β-phase growth into the α-phase. In the core-shell model (a) the β-phase (in grey) grows from the surface of the particle and inwards. In the cap model (b) the β-phase grows from one end of the particle to the other.

Effective Attractive H-H Interactions - ΔH_{attr}

As we saw in section 3.1, adding an interstitial atom into the lattice of a host metal introduces stress on the neighboring region. This stress will also result in a locally expanded lattice around the interstitial, with a displacement field that decreases as $\frac{1}{r^2}$.[164] With the lattice slightly expanded from this interstitial atom, the stress added to the system if another interstitial atom would be added in the expanded region is less than if the same interstitial would be added to a non-expanded region of the lattice.[165,166] Hence, the expanded lattice around hydrogen interstitials results in an effective, attractive H-H potential that lowers the enthalpy of formation of the β-phase as a function

of added hydrogen.[109,155,165,167] Consequently, this effect is recognized as the thermodynamic driving force for the β-phase transformation.[109,155,165,167]

Electronic H-H Interactions - ΔH_{elec}

Working against the attractive effective potential described in the previous paragraph is a repulsive force due to the electronic repulsion between hydrogen atoms that are too close together. When hydrogen is hybridized with the palladium system, the extra electron of the hydrogen atom enters the electronic bands of the host metal. The resulting change to the enthalpy of formation of the β-phase is small for low hydrogen concentrations[109,155,164,167] but becomes significant when the hydrogen concentration in Pd goes above ~60% and is the mechanistic origin for the steep slope in the pressure-composition isotherm in the β-phase (cf. Figure 15).[155]

Other External and Internal Strains - ΔH_{other}

As we have already discussed for ΔH_{coh} and the critical role of interphase stress in the α-to-β phase transition, a natural next step is that other types of stresses also should affect the phase formation enthalpies. These stresses can either be internal, e.g. stress from dislocation networks, directly affecting ΔH_{coh} - or external e.g. strain generated by substrate clamping, which then would add their own term, ΔH_{other}, to the overall enthalpy change $\Delta H_{\alpha-\beta}$.

That both types of stresses, both external and internal, directly affect the phase transformation thermodynamics is well established in the literature. Starting with external stresses, we consider thin film systems of Pd. These are systems that inherently exhibit a high-degree of substrate clamping due to the large substrate surface-to-volume ratio, and consequently, high stresses are generated during hydrogenation due to the compressive forces

the substrate generates on the expanding metal.[168-170] As a consequence of this increased stress during hydrogenation, absorption pressures, and consequently also hysteresis, increase.[30,169]

On the other hand, for internal stresses, e.g. resulting from defect networks, the situation is not as straightforward. It is well established that hydrogen is attracted to different defect sites, such as vacancies[171], dislocations[172] and grain boundaries[173] due to their larger binding energy.[174] Moreover, as previously discussed, if the Pd crystallites are larger than the critical size for dislocation nucleation, and if the stress of the hydrogenation becomes large enough - large amounts of dislocations will be generated during the phase transformation.[30,168-170,175-177] When these dislocations nucleate and move to the surface or a grain boundary, stress is alleviated from the system, and we consequently expect absorption pressures and hysteresis to decrease. This has been exemplified by Alekseeva *et. al.* where it was shown that a higher density of grain boundaries in a Pd nanoparticle, characterized by the total grain boundary length inside the particle (and consequently, a higher the number of grains in the particle) the lower the absorption pressures and degree of hysteresis were.[178] However, this effect was the most pronounced for high-angle grain boundaries and the same effect was not seen for more closely packed twin boundaries. From a mechanistic point of view, this effect can likely be attributed to high-angle grain boundaries providing more room for grains to expand during hydrogenation than more closely packed grain boundaries, *e.g.* twin-boundaries.[178]

Nonetheless, even though dislocations are nucleated to relieve stress in a system, if enough dislocations are formed, they might instead start to *increase* stress during hydrogenation at a critical dislocation density – akin

to dislocation hardening in classical metallurgy.[95] This, together with the effects of external and internal strains on the α-to-β phase transition in supported Pd nanoparticles, specifically the strains that occur as a result of substrate clamping and dislocation networks, are further discussed in **Paper I**.

4.1.2 Kinetics of Palladium Hydride Formation

As previously discussed, hydrogen dissociation at the Pd surface is highly efficient already at ambient conditions (Figure 14). However, due to the relatively high energy barriers of the surface-to-subsurface diffusion ($E_{diff-sub}$ in Figure 14),[149,151] Pd has, compared to some more optimized alloys, e.g. PdAu (see section 4.2.2), relatively sluggish absorption kinetics. The slow hydrogenation kinetics of Pd is especially limiting from a hydrogen sensing perspective, where response times below 1 s are the target set by global stake holders.[10] Consequently, much effort has been put into understanding and accelerating the hydrogen absorption process in Pd.[7,21,34,35,50,77,149,151,175,178-185] The two main pathways to address the slow absorption process of Pd are i) alloying or ii) defect engineering. Alloying (i) will be discussed in section 4.2, and the focus of the following section will be (ii) defect engineering.

The role of defects for the kinetics of the Pd-H system is at first glance contradictive. The lower energy sites provided by dislocations and grain boundaries should intuitively act as traps for hydrogen and consequently lower the diffusivity of hydrogen through the metal. Accordingly, a lower diffusion constant has been reported for Pd samples with a high degree of dislocations and grain boundaries compared to defect-free samples.[155,174,175]

However, this effect is most pronounced in the very low-concentration α-phase regime (< 0.001 H/Pd ratio, < 0.1 mbar H_2 partial pressure). When the hydrogen pressure is increased (> 0.01 H/Pd ratio, > 0.1 mbar H_2 partial pressure), the deepest (lowest energy) traps are quickly saturated, and higher energy / more unstable sites start to fill instead.[34,77] When this happens, pathways that include a range of sites with energies both high and low (such as defects like grain boundaries and dislocations) may overtake pathways with sites of more constant energy (such as a pathway through octahedral sites in a defect-free crystal), as the pathways via defects effectively results in a reduced activation energy barrier for diffusion.[34,77] Consequently, the defects start to act as accelerated pathways for the hydrogen diffusion into the system. Experimental verifications of faster absorption kinetics for intermediate to high hydrogen pressures (> 1 mbar) in Pd with high defect densities have been confirmed for nanocrystalline Pd films vs single-crystal films[34], as-deposited (and therefore, defect-rich) magnetron sputtered vs annealed Pd thin films[35] and for highly-nanocrystalline Pd nanoparticles[31]. As most hydrogen sensors are intended to work from about 1 mbar[10] up to the flammability limit of hydrogen (40 mbar), defects are consequently imperative for accelerating the sensing kinetics of Pd-based hydrogen sensors.

Having established the importance of defects for the overall H absorption kinetics in Pd, we should also add that increased strain has been reported to act detrimentally for diffusion by increasing the activation energy barrier for diffusion.[149] Hence, as defects like dislocations acts as a stress release mechanism, the resulting relaxed structure of a system with an intermediate density of defects (*i.e.* not so many that dislocation hardening start to come

into effect), could also be a factor for the accelerated kinetics in defect-rich systems.

The hydrogen absorption kinetics of defect-lean and defect-rich Pd nanoparticles are further discussed in **Paper I**.

4.1.3 The Influence of Hydrogen Cycling

Metal-hydrogen systems, and specifically Pd-H, are not static systems but highly dynamic. For macroscopic systems, hydrogen embrittlement is a well-studied topic in material science where the critical plastic strength of a metal is reduced upon long-term exposure to hydrogen due to the nucleation of massive defect networks in the metal lattice.[186-189]

For nano-sized systems, and especially Pd nanoparticles, the situation is generally not as straightforward as that hydrogenation exclusively nucleates new defects. It is well established that the mobility of dislocations increases in the hydride state of Pd[155,175] and dislocations and (closely packed) grain boundaries have even been found to completely annihilate after hydrogenation in Pd nanoparticles.[31,32] Wagner and Pundt investigated the stress evolution during hydrogenation of three thin-film Pd samples with different defect densities.[30,168] During the initial part of the hydrogenation (before major plastic deformation), the highest stress levels were found in the defect-free single-crystalline sample, while the lowest stress levels were found in the sample with pre-existing dislocations. Dislocations in both samples were then nucleated and able to creep during hydrogenation to relieve the rising stress levels. The highest final stress (after major plastic deformation) was found in the sample with the highest density of pre-existing

grain boundaries, i.e., the inverse of the initial stress levels. The high stress level in this sample was attributed to dislocation pile-up at the many grain boundaries hindering stress relaxation.[30,168] On the other hand, the lowest final stress levels were found in the (nominally) single-crystalline sample where stress relaxation through plastic deformation was the most efficient.[30] Consequently, for both Pd nanoparticles and thin film systems, hydrogenation can lead to *both* the nucleation of new defects and the annihilation of old ones, as decided by the initial stress state and defect networks of the system pre-hydrogenation.

In **Paper I** and **Paper V**, we investigate the evolution of thermodynamic and kinetic parameters as well as the microstructure of supported Pd nanoparticles upon heavy hydrogen cycling. As a final note for this section, and a corroboration for the above discussion, a consistent trend in both these studies is that the atoms in Pd under hydrogenation are mobile enough to completely change the morphology of the studied nanoparticles. This morphology change comes in the form of a shrinking of the in-plane diameter of the Pd particles (if allowed by the substrate), approaching a more energetically favorable spherical / Winterbottom[190] shape, together with an emergence of distinct Pd protrusions on the surface of the Pd particles and a void at the particle-substrate interface (Figure 17). This morphological restructuring is coupled with deaccelerated kinetics, leading to the likely mechanistic origin of the protrusions to be in the form dislocation creep and subsequent annihilation at the surface. Further discussion of this restructuring as a substrate mediated stress relief mechanism is presented in **Paper I**.

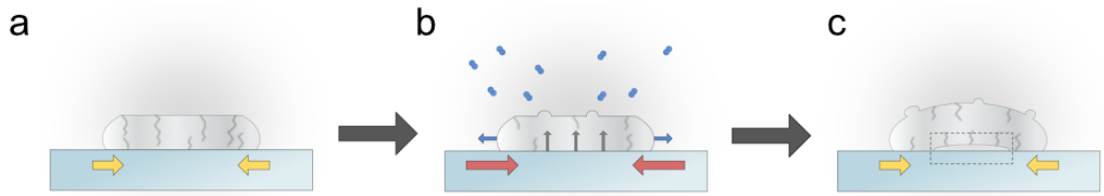

Figure 17. Substrate mediated protrusion growth during hydrogenation. (a) Due to lattice mismatch, the interface region between Pd particle and substrate surface is stressed. (b) During hydrogenation, the Pd particle expands due to the absorbed hydrogen. This expansion increases the stress at the substrate interface, triggering a diffusion of Pd atoms from the interface region to the surface of the particle. (c) The diffusion of Pd atoms from the substrate interface leaves a void in the interface region and protrusions on the surface.

4.2 Alloys of Palladium and their Hydrogen Interactions

Alloying Pd with other metals is a key method for altering the thermodynamics and kinetics of hydrogen absorption in hydrogen sensing applications. Examples include PdAg[18,191-193], PdNi[58,194,195], PdCo[17,18,51] and PdCu[52,59,196] for accelerating the hydrogen sensor response and suppress hysteresis, the ternary PdAuCu[180,181] system for increasing CO poisoning resistance and PdPt alloys for resistance to both oxidation[197,198] and poisoning by species like O_2 and H_2O.[53,60,67,68,127,199-205] In the following sections, I will go through the effects that alloying Pd with other transition metals, specifically Au and Pt, have on the hydrogenation properties of the combined system, with a specific focus on its relevance for rational design of nanoparticle based optical hydrogen sensors in technologically relevant and chemically complex environments.

4.2.1 Thermodynamics of Palladium Alloy Hydride Formation

For hydrogen sensing applications using Pd, the α-to-β phase transition, which is the main contributor to the optical response of Pd-based H_2 sensors (see section 2.1), is generally occurring in the technologically relevant range of 1-6% H_2. Hence, the main thermodynamic motivation for alloying Pd with other metals is to modify the characteristics of this phase transition in some capacity. For example, to limit crack formation induced by the β-phase expansion in macroscopic samples, one can engineer the α-to-β phase transition to occur at higher hydrogen concentrations than the sample is expected to be exposed to. This can be achieved in accordance with the Van't Hoff equation, eq. (7), by decreasing the enthalpy of formation of the β-phase (less negative ΔH_β), e.g. by decreasing the hydrogen solubility in the alloy (less negative ΔH_{sol}) or increasing the phase transition stress (more positive ΔH_{coh}).

However, for nanoparticle-based hydrogen sensors, in which structural failure of the nanoparticle sensing elements rarely is a problem, the main thermodynamic motivation for alloying Pd with other transition metals is instead to reduce hysteresis between the absorption and desorption plateaus (cf. Figure 15b).[46,181,206] This since hysteresis leads to the sensor response being dependent on its hydrogen exposure history, which complicates the sensor readout. Suppression of the hysteresis is achieved by either (i) making the enthalpy difference between the two phases comparable during absorption and desorption, i.e., $\Delta H_{\alpha-\beta}(x) \approx \Delta H_{\beta-\alpha}(x)$ or (ii) by suppressing the phase transition itself, i.e., $\Delta H_{\alpha-\beta}(x) \approx \Delta H_{\beta-\alpha}(x) \approx 0$. In this thesis, I mainly alloy Pd with Au or Pt, which each serve as a

representative example of the modifications (i-ii) of the phase transition enthalpy $\Delta H_{\alpha-\beta}$ of a Pd-alloy.

Starting with Au, the significantly larger lattice parameter of Au (4.07 Å[207]) compared to Pd (3.89 Å[108]) means that for the alloyed PdAu system, the difference in lattice parameter between the α- and β-phase is reduced.[179] Consequently, so are also the magnitudes of the internal, stress mediated enthalpies ΔH_{coh} and ΔH_{attr}, leading to a more negative total β-phase enthalpy of formation ΔH_{β}. This in turn results in a suppressed hysteresis together with a decreased phase transition pressure according to eq. (7) (Figure 18).[157,181,206,208-210]

Conversely, if one alloys Pd with Cu, a metal that is not used in this thesis, but which has been used for comparable hydrogen sensors[52,59,181,196], the effects on the phase transition enthalpies are the opposite of alloying with Au. This is due to the smaller lattice parameter of Cu (3.61 Å[207]), leading instead to a higher (more positive) ΔH_{coh} due to the increased strain barrier during the phase transition. However, the magnitude of ΔH_{attr} (more negative) is also increased, since the attractive effective potential of local interstitial H atoms is also increased. Consequently, hysteresis is still reduced, but the phase transition is pushed to higher pressures due to a less negative total β-phase enthalpy of formation, ΔH_{β} (Figure 18).[181]

In contrast to both Au and Cu, Pt has a comparable lattice parameter (3.92 Å[207]) to Pd. Hence, any lattice parameter induced strain effects on the α-to-β phase transition will be less pronounced in PdPt compared to PdAu and PdCu. Instead, Pt is predominantly reducing the overall solubility of H in the alloy, leading to a decrease in ΔH_{sol} (less negative), resulting in a less

negative ΔH_β and a consequential increase in phase transition pressures (Figure 18).[211] The mechanistic origin for this decreased H solubility originates from the highly unfavorable energetics of hydride formation in neat Pt.[141,211] Indeed, Pt-hydride has a high (positive) enthalpy of formation in the +20-50 kJ/mol range[141,212], resulting in extreme pressures (> 25 GPa) required for the nucleation of the hydride.[212,213] The highly unfavorable enthalpy of formation for hydride in Pt compared to Pd has been described by the *d-band center theory*[141,211,214], which connects the center of a metal's d-band to its reactivity. As an example of this, a d-band center *closer* to the Fermi-level for a metal has been connected with an increased affinity for H adsorption on the metal surface.[214,215] The d-band center model has also been used to represent the affinity of hydrogen absorption for different metals, with Griessen *et al.* connecting a d-band center *further* from the Fermi-level with a high enthalpy of formation for the hydride in the corresponding metal.[141] Consequently, with Pt reported to have a wider d-band with a center further from the Fermi-level compared to Pd, this model has been used to explain the higher enthalpy of formation of hydride in the former metal[141,211]

However, despite its usefulness in capturing broad trends between different metals, more detailed calculations are required for more extensive information about the systems. For example, even though Pd features the strongest-binding H adsorption site according to the d-band theory[216] (e.g. the fcc hollow site on a 111-plane[144,147,217]), other sites on Pt (e.g. the top and bridge sites on the 111-plane) have been calculated to feature higher adsorption energies than the corresponding sites on Pd[144,147], which the d-band center theory consequently fails to capture. Nonetheless, the high enthalpy of formation for Pt-hydride is a well-established

concept[126,128,141,212,213], and its effect of reducing the heat of solubility, ΔH_{sol}, of PdPt alloys is generally consistent with the literature.[211,218,219]

I should here add that several connected studies[126,129,202,220] have claimed that alloying Pd nanoparticles in the 10 nm size range with a small amount of Pt (~ 8 at%) leads to a surprising *increase* of hydrogen solubility. This increase of solubility would supposedly only exist in a small Pt concentration interval around 8 at% before the solubility again starts decreasing at higher Pt concentrations.[218] This effect has been speculated to be a consequence of a shifted d-band center for this specific alloy stoichiometry and nanoparticle size.[218] However, this hypothesized, anomalous difference between the d-band centers of Pd, $Pd_{92}Pt_8$ and other PdPt alloys have, to the best of my knowledge, never been explicitly measured nor modelled.[218] Furthermore, the Pd particles used in many of these studies[126,221] exhibit a surprisingly low H solubility (0.2 H per metal atom at 1000 mbar H_2 and 303 K) compared to other, independent studies of Pd nanoparticles in the same size range (0.4 H per metal atom at 1000 mbar H_2 and 303 K[222,223]). Consequently, this sample-to-sample difference is a further motivation for fabricating and investigating different alloy systems simultaneously and on a single sample, e.g. by the combined microshutter lithography fabrication (section 5.1) and single particle plasmonic microscopy (section 5.3) that we employ in **Paper IV** and **Paper V**.

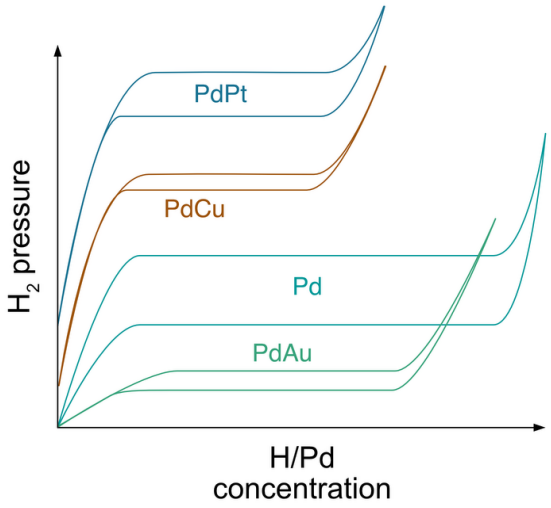

Figure 18. Schematic representation of pressure-composition isotherms for Pd[48,206,224], PdAu[46,206], PdCu[181] and PdPt[211].

Regarding the decreased hysteresis observed for PdPt[126,211], the similar lattice parameters between Pd and Pt again make the strain argument, which was used together with its influence on ΔH_{coh} and ΔH_{attr} to explain the suppressed hysteresis for PdAu and PdCu, less applicable for PdPt alloys. A recent statistical model instead uses a distribution argument to qualitatively show that hysteresis can be suppressed in Pd-alloys with a weak to non-hydride forming secondary alloyant (e.g. Au, Pt, Cu etc.).[150,225] The key idea in this model is that *if* the (non-hydride forming) secondary alloyant is randomly distributed in the Pd lattice, i.e., a perfect solid solution (see section 3.4), the absorbed hydrogen atoms should distribute more evenly in the alloy lattice during the hydrogen sorption processes (Figure 19).[150,225] This suppression of hydrogen agglomeration should then lead to a corresponding suppression of the α-to-β phase transition.[150,225] From an enthalpy perspective, this would mean that the $\Delta H_{coh}(x)$ and $\Delta H_{attr}(x)$ terms in eq. (9), become more comparable to each other during absorption and desorption

for every hydrogen concentration x, leading to $\Delta H_{\alpha-\beta}(x) \approx \Delta H_{\beta-\alpha}(x)$ and thus a reduced hysteresis.

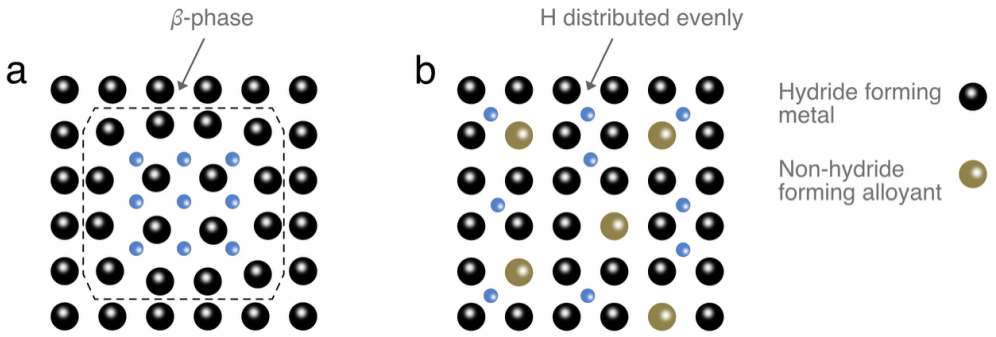

Figure 19. (a) In a hydride forming metal, e.g. Pd, H (blue) has a thermodynamic drive to agglomerate due to the expanded lattice around already absorbed H. This is the mechanistic origin behind the $\Delta H_{attr}(x)$ enthalpy term in eq. (9) and leads to the emergence of the β-phase. (b) According to Mamatkulov *et al.*[150,225], a solid solution of non-hydride forming secondary alloyants, e.g. Au or Pt, will lead to a decrease in H binding energy at every site neighboring an atom of the non-hydride forming alloyant. This decrease should then supposedly exceed the energy earned from $\Delta H_{attr}(x)$, leading to a spatially uniform distribution of H atoms and a consequential suppression of hysteresis.

On the basis of the above discussion, the thermodynamics of Pd-based PdAu, PdPt and PdPtAu alloys is further discussed in **Paper III** and **Paper V**.

4.2.2 Kinetics of Palladium Alloy Hydride Formation

For hydrogen sensor applications, the main motivation from a kinetics perspective to alloy Pd with other metals is to achieve a sensor response to H_2 fast enough to fulfill the response time performance target set by various

global stakeholders.[10,11] For hydride-based hydrogen sensors utilizing Pd, this translates to reducing the time of hydrogen absorption into the metal. This absorption time, despite being an intuitively straightforward concept, is decided by a number of system specific parameters, e.g. rate-limiting activation energy barriers and total volume of absorbed hydrogen. In the following section, I will discuss the different factors deciding the hydrogen absorption time in a Pd-based alloy, with PdAu as the primary model system.

Beginning with rate-limiting energetics, in Pd, the rate-limiting step of hydrogen absorption is the diffusion from the surface to the first sub-surface layers (see Figure 14 and section 4.1.2).[149,151] Consequently, one of the primary goals of alloying Pd with other metals, e.g. Au, is to reduce the activation energy of this elementary reaction step. Due to the endothermic energetics of H adsorption and hydride formation on/in Au[142,151,226], which is a consequence of the filling of high energy, anti-bonding states during H-Au hybridization[216], alloying Pd with Au has been shown by first principle studies to successfully decrease the activation energy barrier for the rate-limiting diffusion of H from the surface to the first subsurface layers.[151] The enhanced hydrogen absorption kinetics of PdAu is experimentally well-established[151,206,210] and has enabled the fabrication of hydrogen sensors with subsecond response times.[50] However, alloying is not always exclusively beneficial, which PdAu paradoxically also is a good example of. Specifically, if one adds too much Au to Pd, not only will the density of available Pd surface sites for H_2 dissociation decrease[142], but with increasing amounts of non-hydride forming Au in the bulk of a PdAu alloy, bulk diffusion will emerge as a competing rate-determining step with the surface-to-subsurface diffusion.[226] In other words, by trying to improve the kinetics of the surface-to-subsurface diffusion by alloying Pd with Au, using excessive amounts can

instead introduce new kinetic bottlenecks either at the surface, in the bulk, or both.[226]

Further complicating the experimental quantification of the kinetic energy landscape of alloys is that experimentally measured apparent activation energies, E_a, generally consist of a weighted sum of energies from elementary reaction steps. The reason for this is that experimental E_a's generally are quantified from the rate of the product at the end of a reaction chain. This means that if the rate-limiting step is not the very first step of the reaction, e.g. adsorption on a surface, the kinetics of the rate-limiting step – and consequently the measured E_a – are generally dependent on multiple previous steps in the reaction chain.[159,227,228] Taking a hydride, where the surface-to-subsurface diffusion is the rate-limiting step, e.g. Pd, as an example, experimentally measured E_a's are not only consisting of the activation energy of the rate-limiting surface-to-subsurface diffusion step, but is also influenced by (i) the equilibrium H_2 dissociation enthalpy at the current temperature, as well as (ii) any potential temperature dependence of the available surface sites, e.g. temperature activated alloyant surface segregation.[159,227,228] This is also excluding any effects that defects might have on the kinetics, which adds further complexity to the energetics (see section 4.1.2). Additionally, if the rate-limiting step would change, e.g. as discussed for PdAu with high concentrations of Au, the experimentally measured activation energy E_a will evolve to include even more/other terms. This is exemplified by plots of measured E_a for hydrogen absorption in PdAu alloys as a function of Au at%, which exhibit an inverse volcano-shape (see Patki *et al.*[229] and **Paper V**), reflecting the convoluted and shifting contributions to the measured apparent activation energy E_a for a Pd-alloy system.

Moreover, and as discussed in the introduction to this section, the rate of hydrogen absorption into a hydride forming metal is not only decided by the activation energies of the different reaction steps, but also by the amount of reactant, i.e. the amount of dissociated H atoms on the metal surface. For the Arrhenius equation, which together with the gas constant R and temperature T connects the measured rate constant, k_a, of a product to the (composite) apparent activation energy E_a of the corresponding reaction steps,

$$k_a = k_0 e^{-\frac{E_a}{RT}} \tag{10}$$

with k_0 as a pre-exponential factor.[230] Mathematically, k_0 is the rate at "infinite" temperature. For surface mediated reactions, which includes hydrides, k_0 is generally connected to the concentration of available surface sites, which for all alloy systems studied in this thesis means Pd- or Pt-sites available for H_2 dissociation.[230] With this in mind, it is clear that for alloys that include elements that are thermodynamically driven to segregate to the surface, but which also principally are inactive for H_2 dissociation, e.g. Au[142,231], k_0 for these alloys will be strongly dependent on the Au concentration at the surface, which in turn is decided by both temperature, the adsorbate environment and the alloy stoichiometry.[142,231]

Furthermore, for the systems that are the primary focus of this thesis, i.e. Pd- and Pt-based nanoparticles, it is not only the *rate* of hydrogen absorption in the hydride forming alloys that decides the final response time of the sensor, but also the total *volume* of absorbed H. This means that replacing hydride forming Pd with non-hydride forming metals, e.g. Au or Pt, inherently

accelerates absorption times simply by a facilitating a reduced volume of absorbed H to reach a steady state after H_2 exposure compared to pure Pd.

With this discussion introducing the key factors deciding the response times of Pd-alloy based hydrogen sensors, the hydrogen absorption kinetics of PdPt, PdAu and PdPtAu nanoparticles are further discussed in **Paper V**.

4.2.3 Palladium Alloys in the Presence of Poisoning Species

Beyond modifying the phase transition characteristics and hydrogen absorption kinetics of Pd-based H_2 sensors, a third motivation for alloying Pd with other metals is to make the material more resistant to poisoning species. In the following sections, I will discuss some of the most important poisoning species in H_2 sensing, which I here define as chemical compounds that are (i) common at ambient conditions for deployed hydrogen sensors and (ii) highly efficient in deactivating the sensor's response to H_2. Three species that fulfill these criteria, and which I focus on in this thesis, are CO, NO_x and H_2O.

4.2.3.1 NO_x and CO compounds

CO and the different NO_x compounds are molecules whose primary origin in the atmosphere is due to the combustion of fossil fuels.[232,233] Consequently, these species are constantly present in the atmosphere, with typical concentrations of ~1 ppm and ~50 ppb, with elevated concentrations in urban settings during daily rush hours, for CO and NO_x respectively.[234,235]

Both CO and NO_x are deactivating Pd- and Pt-based hydrogen sensors in the same way, namely by binding more strongly to the active sensing materials than hydrogen. For NO, which out of the two most common NOx species, NO_2 and NO[235,236], binds more strongly to Pd than H (Table 1). The same applies also for CO (Table 1). Consequently, by alloying Pd with an element that exhibits lower binding energies to CO and NO, e.g. Pt or Au, the deactivation can be reduced (Table 1).[216]

	H	CO	NO	H_2O
Pd	-0.22 to -1.26 eV, mean of -0.60 eV [142,144,146,147,217]	-1.17 to -2.01 eV, mean of -1.69 eV [23-25,27,28]	-1.09 to -2.29 eV mean of -1.80 eV [23-27] -1.24 eV for NO_2[23]	-0.40 eV[237]
Pt	-0.11 to -0.52 eV, mean of -0.36 eV [144,147,217]	-1.36 to -1.56 eV, mean of -1.42 eV [23,24]	-1.23 to -1.68 eV, mean of -1.44 eV [23,24]	-0.38 eV[237]
Au	-0.47 eV[151] ($Pd_{50}Au_{50}$)	-1.16 eV[24] ($Pd_{50}Au_{50}$)	-1.25 eV[24] ($Pd_{50}Au_{50}$)	-0.27 eV[237]

Table 1. Adsorption energies for different molecular gas species on Pd, Pt and Au / $Pd_{50}Au_{50}$. The energies differ depending on binding site and study.

The use of PdPt, PdAu and PdPtAu alloys for hydrogen sensing in backgrounds contaminated with CO and NO_x is further discussed in **Paper V** and **Paper VI**.

4.2.3.2 Water

Any hydrogen sensor that aims to be realizable in technologically relevant conditions, e.g. ambient atmospheric air, needs to be able to withstand elevated humidity levels. This is due to (i) the inevitable presence of H_2O in the atmosphere, even in some of the most arid deserts on the planet[238], and (ii) H_2O being either a reactant or product in most reactions involving H_2, e.g. the hydrogen oxidation reaction in fuel cells or in H_2 production through water splitting. Consequently, there is a great demand for hydrogen sensors that perform well at elevated humidity levels, as exemplified by humidity-focused performance targets set by global stakeholders such as the International Organization for Standards (ISO)[11] and the US DoE[10].

Just as with NO_x and CO, H_2O decreases both the sensor's sensitivity and response time to H_2 by competitive adsorption on the surface of the active sensing material.[6,7,23,27] This adsorption process, and the subsequent formation of water layers, is a highly complex process due to the adsorption energies of H_2O to most metals, e.g. Pd or Pt, and the intermolecular forces between individual H_2O molecules being of comparable orders of magnitude.[239,240] Consequently, water layer formation on metal surfaces is a highly dynamic process with considerable degrees of freedom, leading to first-principle based simulations of these systems being highly computationally expensive.[239,240] Nonetheless, simulations of adsorption of a single H_2O monomer on a close-packed metal surface using van der Waals

corrected DFT-functionals can still yield relevant insights on the relative strength of water's interaction with different metals.[239] For Pd, Pt and Au specifically, adsorption energies of -0.40, -0.38 and -0.27 eV respectively have been reported from this kind of study (Table 1).[237] Out of these three metals, the debilitating effect of H_2O poisoning on H_2 sensing is consequently the worst on Pd due to the stronger binding energy.

Nonetheless, most metal surfaces, including Pd, Pt and Au, are not limited to simply adsorbing H_2O, but can on their surfaces also facilitate a number of reactions including the molecule, e.g. partial dissociation of H_2O into OH and H.[239] One of these reactions, which can occur under the presence of H_2 and O_2, i.e. typical conditions for H_2 sensing in atmospheric air, is the hydrogen oxidation reaction (HOR). As previously discussed (see chapter 0), this is the basis for many types of catalytic hydrogen sensors.[241] More important in the context of H_2O poisoning however, is that the HOR is a highly exothermic reaction (enthalpy of formation of -2.96 eV[242]), and the heat generated from the reaction consequently leads to an increased desorption of weakly bound surface species, e.g. H_2O.[53] Out of Pd, Pt and Au, the HOR proceeds most efficiently on Pt[241], meaning that adding Pt to a material that is heavily susceptible to poisoning by H_2O, e.g. Pd, can beyond acting as a second sensing material (see section 2.1) also indirectly alleviate H_2O poisoning on the Pd-surface by decreasing the number of adsorbed water layers on its surface. This effect is likely mediated by the transfer of residual heat from the efficient HOR on the Pt.[53]

Using Pt to alleviate water poisoning on Pd is further discussed in **Paper III**, together with a more general discussion on the interactions between Pt and H_2O in **Paper II**.

4.2.4 The Influence of Heavy Hydrogen Cycling

As established in section 4.1.3, Pd-structures are highly dynamic systems whose microstructure evolve during interaction with hydrogen, a phenomenon that extends also to Pd- and Pt-based alloys.[231,243] Indeed, a microstructural evolution due to hydrogen exposure extends to many technologically relevant alloy systems, as exemplified by decades of research into macroscopic systems, such as hydrogen embrittlement in commercial steels[29] and the physical degradation of hydride-forming alloys for hydrogen storage.[244-246] However, for nano-sized alloy systems, the literature is more sparse. The importance of dedicated studies on nano-systems is exemplified by the "solute softening effect" in which the hardness of different nano structures[84,247-249], e.g. NiCo nanoparticles[84], is decreased upon alloying with a secondary element, in sharp contrast to the solute hardening observed for the corresponding macroscopic systems.[84] This consequently means that concepts from the studies of the interaction of hydrogen with macroscopic alloys, e.g. hydrogen embrittlement, might not be directly applicable to nano-systems. To this end, the literature that does exist for nano-sized Pd-alloy systems is mainly focused on different types of adsorbate-mediated miscibility changes of the alloyants, e.g. (i) surface segregation of Pd in PdAu in a H_2 rich atmosphere while Au segregates in vacuum[142,231] and (ii) solid solution mixing of nominal Pd-Pt core-shell nanoparticles.[119,126,128,129,202]

In the first case, i.e. the segregation tendencies of Pd versus Au, the thermodynamic energetics initially seem straightforward. Au atoms have lower surface energy than Pd, and therefore should demonstrate a higher

thermodynamic drive to segregate to the surface under vacuum conditions.[142,231] However, this effect can be reversed by adsorbates like H or CO, who instead drive Pd towards the surface.[142,231,250,251] Consequently, the thermodynamically most stable surface state of a PdAu alloy nanoparticle should be dependent on its current (gas) environment. However, PdAu nanoparticles of the sizes studied in this thesis (disks with a diameter of 100-200 nm and a height of 25-30 nm) conversely demonstrate a very high stability in both their hydrogen absorption kinetics, response magnitudes and morphology, involving dozens of repeated hydrogenations over months of operation in synthetic air.[50] In other words, the experimentally verified stability of PdAu nanoparticles, as inferred by their stable hydrogenation characteristics, and the proposed Pd-Au (adsorbate-driven) thermodynamic segregation tendencies is tentatively contradictive.

To the best of my knowledge, there is no *established* explanation for this discrepancy, but three different rational hypotheses can be discussed. The first (i) involves the surface of the experimentally measured nanoparticles, which after having been exposed to an initial activation sequence of up to 10 H_2 pulses[50,180], reaches a steady – but meta-stable – state, as dictated by the specific durations of the alternating H_2 rich and H_2 poor atmospheres. However, due to the high reproducibility of the measured hydrogenation kinetics over many cycles[50,180], two more reasonable explanations are rather (ii) that the PdAu solid solution is thermodynamically stable for the specific Pd-Au compositions and nanoparticle sizes studied here (see section 3.4) or (iii) that the Pd and Au atoms are kinetically locked in their solid-solution configurations. The latter argument is corroborated by an increased toughness, defined as the stress-per-strain ratio after plastic failure, for alloy nanoparticles compared to their single-element counterparts.[84] In other

words, even if a lower stress might be needed in an alloy nanoparticle to nucleate the first dislocation, the ensuing plastic flow / dislocation slip has a higher energy barrier for propagating.[84] The structural stability and the corresponding hydrogenation characteristics for PdAu nanoparticles of varying stoichiometries under long-term hydrogen cycling is further discussed in **Paper V**.

For PdPt nanoparticles on the other hand, most segregation studies have been focused on the thermodynamic stability of Pd-Pt core-shell particles, as this is a commonly synthesized structure of this system in various applications.[119,125,126,128,202] For this system, it is well-established that bulk Pd has lower surface energy[119,125], which for core-shell nanoparticles prepared with Pt as the shell consequently leads to the diffusion of bulk Pd to the surface and a resulting (meta-stable) solid-solution mixing of the alloyants.[119,126,128,202] However, consistent with the discussion regarding nanophase diagrams in section 3.4, other studies have argued that the thermodynamically most stable structure is dependent on the specific nanoparticle size and alloy stoichiometry, leading to surface Pt being stable for certain configurations.[119,125]

Nonetheless, regardless of what the most stable structure of a specific PdPt nanoparticle might be, cyclic hydrogenation of these systems has been argued to drive the morphological restructuring of the nanoparticles toward their thermodynamic minimum energy state.[126,128] In other words, the hydrogen absorption/desorption process mainly affect this system by providing the necessary kinetic energy for the particles to restructure toward their the thermodynamically most stable structure. This contrasts with PdAu, where it was argued that the interaction with H_2 itself can alter the

thermodynamic minimum.[119] On this note, the structural stability and the corresponding hydrogenation characteristics for PdPt nanoparticles of varying stoichiometries under long-term hydrogen cycling is further discussed in **Paper V**.

5 Experimental Methods

In the following chapter, I will briefly describe some of the specific nanofabrication and experimental methods used in this thesis. This includes our microshutter nanofabrication method for high precision fabrication of up to 50 nanoparticle alloy systems on a single sample (section 5.1), nanocompression for systematic plastic deformation of individual nanoparticles (section 5.2) as well as plasmonic-based optical gas sensing setups with both single-particle (section 5.3) and ensemble resolution (section 5.4).

5.1 Microshutter Nanofabrication

When studying the hydrogenation properties of different binary and ternary alloy systems, the number of viable systems to fabricate and test can quickly take on overwhelming proportions. Taking the PdAu system as an example, even if we would limit ourselves to only investigate alloys in a relevant range for H_2 sensing applications, e.g. $Pd_{50}Au_{50}$ to $Pd_{99}Au_1$ in steps of 2.5 at% Au per sample, this still corresponds to approximately 20 samples. Clearly, this translates to a considerable amount of hours including both the fabrication and experimental testing of every individual sample. Additionally, we must also consider the inherent uncertainties and sample-to-sample variations that inherently follow from fabricating and testing a large number of individual samples. For this purpose, the microshutter nanofabrication method was developed. Using this nanofabrication method, dozens of different nanoparticle alloy systems can simultaneously be fabricated on a single sample, minimizing both fabrication time and sample-to-sample errors.

However, before I go into the details of the microshutter fabrication method, I need to describe the general foundation for how we nanofabricate alloy nanoparticle array samples on a surface. This approach is based on the subsequent deposition of thin films of different metals, whose thickness defines the final alloy composition, through a supported, prefabricated nanolithography mask, the holes in which decide the size and position of the nanoparticles.[183]

For the preparation of the nanolithography mask, we start with a clean substrate wafer, e.g. Si, SiO_2 or sapphire (I in Figure 20) which we spin-coat with an electron-sensitive resist (II in Figure 20). After this step, there are two different options to define the mask. In the first option, which can be used to prepare well-defined, regular particle arrays, the spin-coated wafer is exposed to electrons by use of an electron-beam lithography (EBL) system (III-a in Figure 20). Next, the sample is placed in a developer solution to dissolve the resist in the areas exposed to the electron beam (IV in Figure 20). The second option to define the mask is to use Hole-mask Colloidal Lithography (HCL)[252] (III-b in Figure 20). This method involves the distribution of colloidal polystyrene beads on the sample surface, deposition of a protective Cr layer, tape stripping away the polystyrene beads and etching of the mask by dry reactive-ion etching (DRIE), resulting in a semi-random nanolithography mask (IV in Figure 20).

The next step of the fabrication is the subsequent deposition of different metals through the mask (V-a in Figure 20). This is done by evaporation of thin films of the desired metals by an e-beam physical vapor deposition (PVD) system. The metals are deposited layer-by-layer, and the ratio between the layer thicknesses of the different metals defines the composition

of the final alloys. After the PVD step, the mask is removed in a lift-off step and the sample is annealed at high temperature to form the final, alloyed nanoparticles. This annealing process is based on the principle of thermodynamically driven atomic mixing of alloy components by solid-state diffusion, which can occur far below the respective melting temperatures of the constituent metals.[183] Hence, homogeneous alloys can form, despite the low temperature, provided that alloying is thermodynamically favorable and that sufficient time is provided for diffusion.[183]

The microshutter method has been used to successfully fabricate alloy nanoparticle samples for over a decade[46,50,179-181,183,253,254], but has the drawback that a single sample only can support a single alloy composition. The microshutter alleviates this limitation. The tool itself is a custom-built sample holder for the PVD system (Figure 21) that introduces a moveable piezo-controlled microaperture between the sample and the metal source (V-b in Figure 20). Hence, when the aperture moves across the sample it defines both the area where the metal is deposited and the final thickness of each metal layer. In this way, particles of varying alloy compositions can be fabricated on the same sample with high precision. The demonstration of this technique and its application for plasmonic-based hydrogen sensing is the focus of **Paper IV**, and it is again used in **Paper V**.

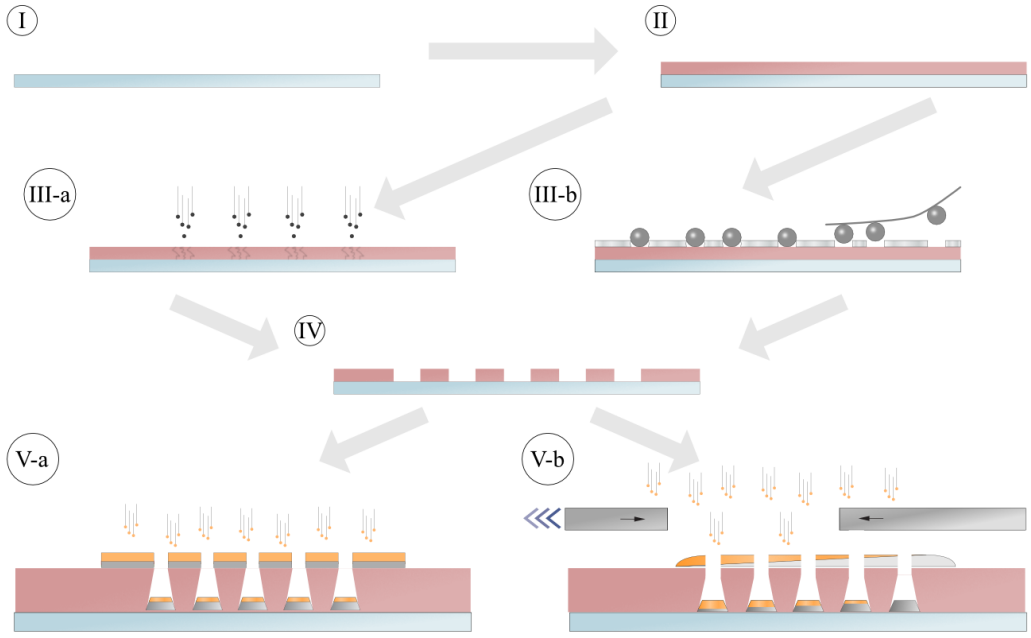

Figure 20: Schematic of the bottom-up nanofabrication process of alloy nanoparticles. (I-II) A substrate wafer (*e.g.* Si, SiO_2 or sapphire) is prepared and spin-coated with an electron-sensitive resist. The nanolithography mask is then either defined by (III-a) electron-beam lithography or (III-b) Hole-mask colloidal lithography[252]. (IV) Final nanolithography mask. Metallization of the sample is performed by subsequent deposition of metal films either (V-a) directly or (V-b) through a moving aperture using the microshutter device.

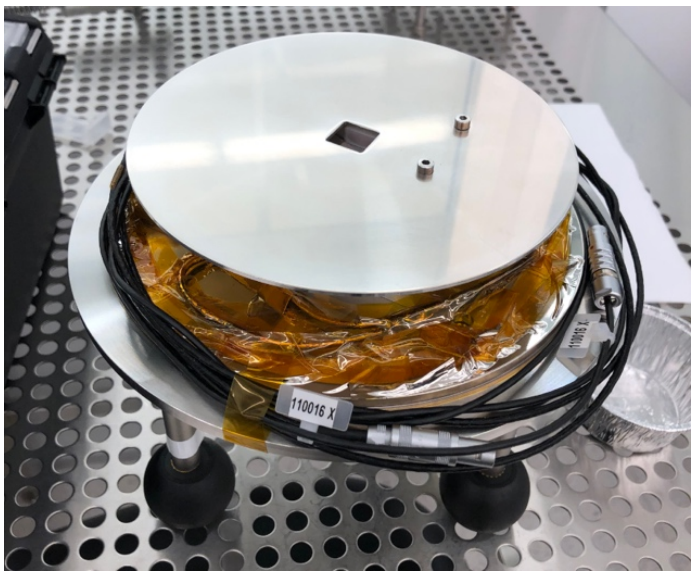

Figure 21: Photograph of the microshutter device mounted on a sample holder for a Lesker PVD225 e-beam physical vapor deposition system.

Despite the efficiency of the microshutter concept, the method comes with some intricacies that needs special consideration. One of the main limiting factors in terms of both the spatial and compositional resolution of the tool comes down to the precision in the geometry of the sample substrates. The reason for this is related to how samples are mounted in the device. At the PVD step of the fabrication process, the sample (with its prefabricated mask) is mounted in a fixed slot inside the microshutter (Figure 22a). As the dimensions of this slot are fixed, this means that the sample must fit perfectly inside the slot for maximum spatial and compositional resolution during the metal deposition. To demonstrate this, we can imagine that the sample is slightly smaller than the slot. This results in a small gap forming between the sample and the walls of the slot (Figure 22b), and translates to an uncertainty between the relative position of the aperture and the lithography mask on the sample. To showcase how important this can be, a schematic of a

representative lithography mask together with the positions of the blocking edge of the aperture at each deposition step is presented in Figure 22c. In this example, the row-to-row distance between particle rows in the mask is 2.5 μm and the aperture is programmed to stop between every row. This means that if the misalignment of the sample substrate is more than 2.5 μm, there is a high likelihood that the blocking edge of the aperture will not be positioned correctly relative the particle mask on the sample, and the alloy compositions will consequently be off.

From this example, it is evident that high-precision control of the sample substrate's geometries is critical. For most microshutter samples used in this thesis, traditional dicing using a Disco DAD-3350 dicing saw have been used to define the sample substrates. However, using this method results in a high variance in the dimensions of the substrates, yielding a significant number of non-usable substrates from every diced wafer. An alternative method that has been promising in trial rounds is Si-specific DRIE etching (from the front) combined with traditional dicing (from the back). Micro water jet cutting has also been under discussion but not yet realized.

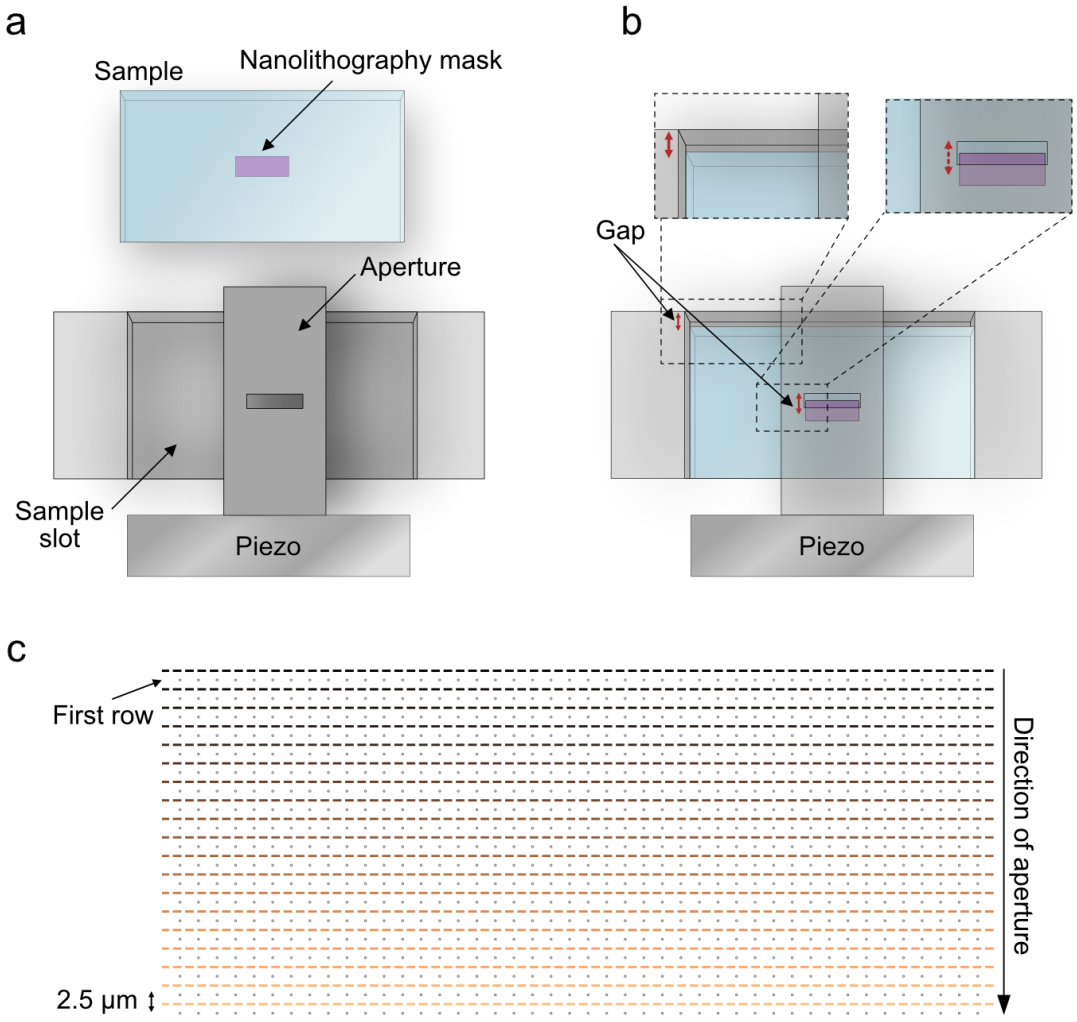

Figure 22: (a) Schematic of the sample mounting area of the microshutter device, including the sample slot and the aperture, together with a sample before mounting. (b) The mounting of a sample slightly smaller than the sample slot results in a gap forming between the sample and the slot wall (red arrow in the left magnified area). This leads to an uncertainty of the position between the microshutter aperture and the nanolithography mask (red, dashed arrow in the right magnified area). (c) Schematic of a representative nanolithography mask (black dots) together with the programmed position of the blocking edge of the aperture (dashed lines) in each deposition step. The aperture is programmed to move from top to bottom.

5.2 Nanocompression

When fabricating nanoparticles using nanolithography combined with PVD, it is practically impossible to control the defect density in the final nanoparticles beyond the two extremes. In other words, either one leaves the particles "as is" after metallization and mask lift-off, resulting in highly nanocrystalline particles consisting of thousands (depending on the size of the nanoparticle) of grains with dimensions in the range of single nanometers[31], or, one anneals the sample, leading to nanoparticles consisting of a few, large grains with a significantly lower defect density (see **Paper I**). This makes a thorough quantification of the impact of different defect densities on the hydrogenation properties of particles fabricated with our method difficult.

To this end, in **Paper I**, we instead used nanocompression on annealed Pd nanoparticles post-fabrication to systematically introduce defects in the annealed particles via plastic deformation (Figure 23).[84,86,88,255] The nanocompression device used (Bruker Hysitron PI85) consists of a pyramid-shaped diamond "punch" with a flat tip that is brought into contact with a nanoparticle, after which load is applied until the target displacement is achieved (Figure 23). This type of nanocompressor employs a capacitive transducer design to simultaneously apply load and measure the resulting displacement of the tip. This type of design generally employs three capacitive plates, where a direct voltage on the moveable middle plate (to which the diamond tip is attached) provides the load, with the resulting displacement measured via a change in capacitance between the moving plates.[256] The minimum resolvable displacement and load for this nanocompressor is ~ 1 nm and ~ 1 μN respectively.

Using this technique, in **Paper I** we systematically nanocompressed 56 individual Pd nanoparticles of 60 nm nominal thickness to different degrees (nominal displacements of 5 nm, 10 nm, 15 nm, 20 nm, 25 nm, 30 nm, 35 nm and 40 nm) and investigated their corresponding hydrogenation properties, e.g. hydrogenation kinetics, phase transition characteristics and cycling stability.

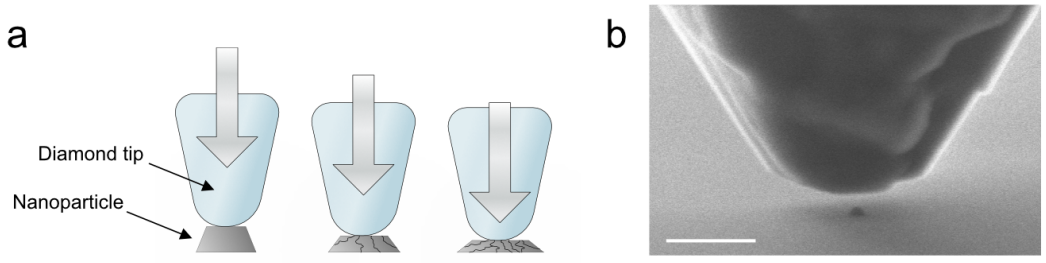

Figure 23: (a) Schematic of the nanocompression of a single nanoparticle. The diamon tip is brought into contact with the particle, which is compressed until the target displacment is reached. (b) SEM image of the diamond tip and a Pd nanoparticle. Scale bar is 1 μm.

5.3 Single Particle Plasmonic Microscopy

To study nanoparticles at their individual level, we make use of the light scattered due to the LSPR effect (see section 2.1) together with an upright microscope equipped with a ring-illumination dark-field objective. In this type of objective, the incident light is focused on the sample at a very high angle, ensuring that only light scattered from the sample, and minimal reflected incident light, is collected by the objective lens (Figure 24a). Even

though the nanoparticles themselves are too small to individually resolve, a single Pd nanoparticle of the size studied in this thesis (disks of diameter 150-200 nm and height of 25-30 nm) scatters enough light to clearly be visible in a dark-field microscope as a diffraction-limited spot of light (DLS). Consequently, if the particles are fabricated on the sample in a well-defined array, e.g. by EBL-facilitated nanolithography, such that the distance between every individual particle is larger than the diameter of their corresponding DLS, we can thus optically follow the evolution of the scattering from individual nanoparticles (Figure 24b-c). To this end, when Pd-based particles absorb hydrogen, their scattering cross-section will decrease as the hydrogen concentration increases in the Pd (see section 2.1). Consequently, using a Complementary Metal Oxide Semiconductor (CMOS) camera or an Electron Multiplying Charge-Coupled Device (EMCCD) camera with an objective of suitable magnification (e.g. a camera with a sensor chip in the range of 10 x 10 mm and a 50X objective), we can optically follow the hydrogenation of hundreds of individual Pd-based nanoparticles simultaneously *in situ* (Figure 24c).

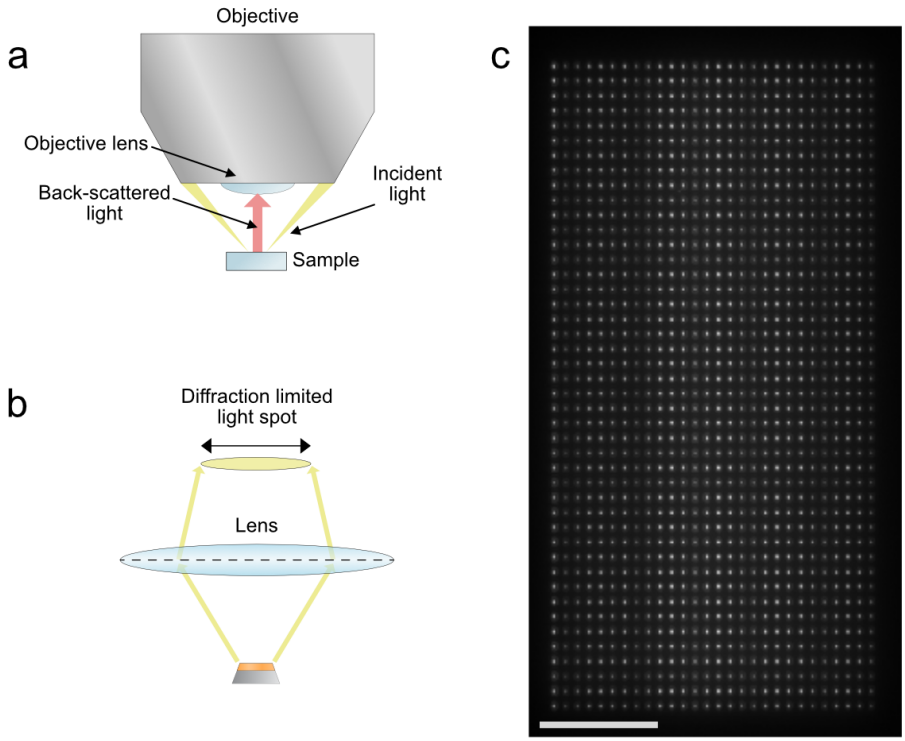

Figure 24: (a) Schematic of back-scattering dark-field microscopy. The incident light exits the objective at a high angle so that its reflection is not collected by the objective lens. As such, only the back-scattered light from the sample is collected and imaged. (b) Schematic of a diffraction limited spot (DLS), resulting from the light scattered from a single nanoparticle. The diameter of the DLS is more than an order of magnitude larger (~1 μm) than the diameter of the nanoparticle (~100 nm), but provided that the nanoparticles are adequately separated (i.e. more than the diameter of a DLS), every individual nanoparticle is still resolvable from their corresponding DLS. (c) An array of a spatially separated Pd-based nanoparticles as viewed through a dark-field microscope. Each DLS is the result of the light scattering from a single nanoparticle. Scale bar is 50 μm.

To provide the gas environment for the *in situ* experiments, the sample is placed in a gas-tight reactor chamber where optical access is provided

through a glass window (Figure 25a). Automatic, solenoid valves at the inlet and outlet allow quick exchange of the gas environment. On the outlet side, either an atmospheric exhaust pipe or a vacuum pump can be connected to allow for either continuous flow or vacuum measurements (~1 μbar base pressure), respectively. Different gases (e.g., Ar, H_2 and O_2) are available and supplied to the inlet through mass-flow controllers (MFC's) with control of the individual flow rates for every gas (Figure 25b). The gases are mixed in the inlet piping before introduction into the reactor chamber. A heating stage beneath the sample and heating tape mounted on the inlet piping allows for heating of both the sample and the gas used in the experiment. The system is fully automatic and controlled through a custom Labview software to minimize operator-induced experiment-to-experiment errors and to allow for maximum reproducibility.

This type of setup, either directly using scattered intensity as described above or with a spectrometer mounted in the optical path for spectral resolution, has been used in the last decade for a number of studies investigating both the hydrogenation and the catalytic properties of individual metallic nanoparticles[31,178,224,257-261], as well as in **Paper I**, **Paper IV** and **Paper V**.

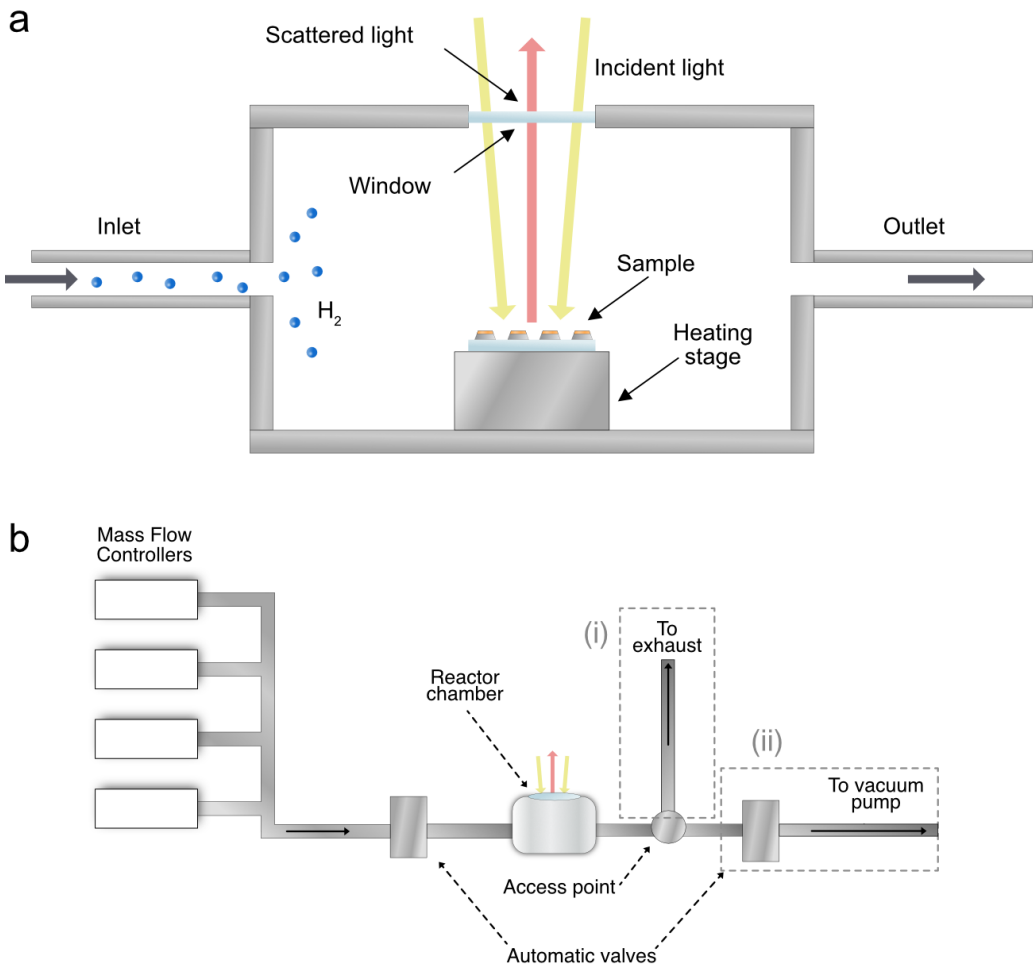

Figure 25: (a) Schematic of the reactor chamber for gas sensing experiments with single particle resolution. The samples are placed on top of a heating stage inside a gas-tight reactor chamber with optical access through a top-mounted glass window. An inlet and outlet provide gas exchange through automatic solenoid valves. (b) Schematic of the full gas sensing setup. MFC's provide controllable gas flows that are mixed in the inlet piping. An automatic valve controls when the gas is introduced into the reactor chamber (a). An access point provides the choice between i) continous flow experiments where the gas is fed to the ventilation exhaust or ii) a second automatic valve which leads to a vacuum pump, which is used for kinetics experiments in vacuum.

5.4 Ensemble Nanoplasmonic Spectroscopy

Beyond the single particle plasmonic microscopy, which provides information from individual particles, it is interesting to also be able to test ensembles of plasmonic particles, i.e. the type of full sensor chips that are used in more realistic, commercialized versions of nanoparticle-based plasmonic sensors.[12,262] In this thesis, two different spectroscopy-based ensemble setups have been used. The samples used in both these setups are large-scale (i.e. approx. 10 x 10 mm) sensor chips, fully covered with quasi-random arrays of nanoparticles fabricated on transparent substrates (e.g. fused silica) using HCL.[252] Due to the scalable fabrication principle of the HCL samples, they are a good representation of what future, large-scale and commercialized nanoparticle-based plasmonic gas sensors might resemble. Indeed, this type of sample design is already used by some companies for gas sensing applications.[262]

Furthermore, the transparent substrates allow us to track the evolution of the particles' ensemble plasmonic resonance when they are exposed to different analytes in the gas phase from simple extinction measurements, either directly from the transmitted light intensity[179] or from spectral shifts of the LSPR peak if a spectrometer is used for the readout.[21,46,48,50,181,206,263] Which of the two readout methods that is the most sensitive depends on the specific changes to the dielectric functions of the sensor material and the environment that the analyte induces (see section 2.1). Nonetheless, for the ensemble samples used for hydrogen-sensing applications in this thesis, spectrally-resolved data generally provide information that are both more detailed and more sensitive than data collected from absolute transmission measurements,

which consequently justify the increased cost of adding a spectrometer to the setup.

In this thesis, two different spectroscopy-based setups and one transmission/extinction intensity-based setup for nanoparticle ensemble sample measurements have been used. In **Paper II** and **Paper III**, we used a dual-chip reactor chamber with capability of spectral readout of two sensor chips simultaneously (Figure 26). The two sensor chips are generally divided such that one chip consists of a hydrogen-active sensing material and the other of a non-reactive reference material (e.g. SiN-covered Au). In this way, drifts in the illumination source or other, environmentally induced drifts can be corrected for. Moreover, on this setup we have installed a Controlled Evaporator Mixer (CEM), which is connected to a water supply by a Liquid Flow Controller (LFC), and which we can use to humidify the experiment gas mixtures from 0 to 80% relative humidity (RH) before introduction into the reactor chamber (Figure 26).

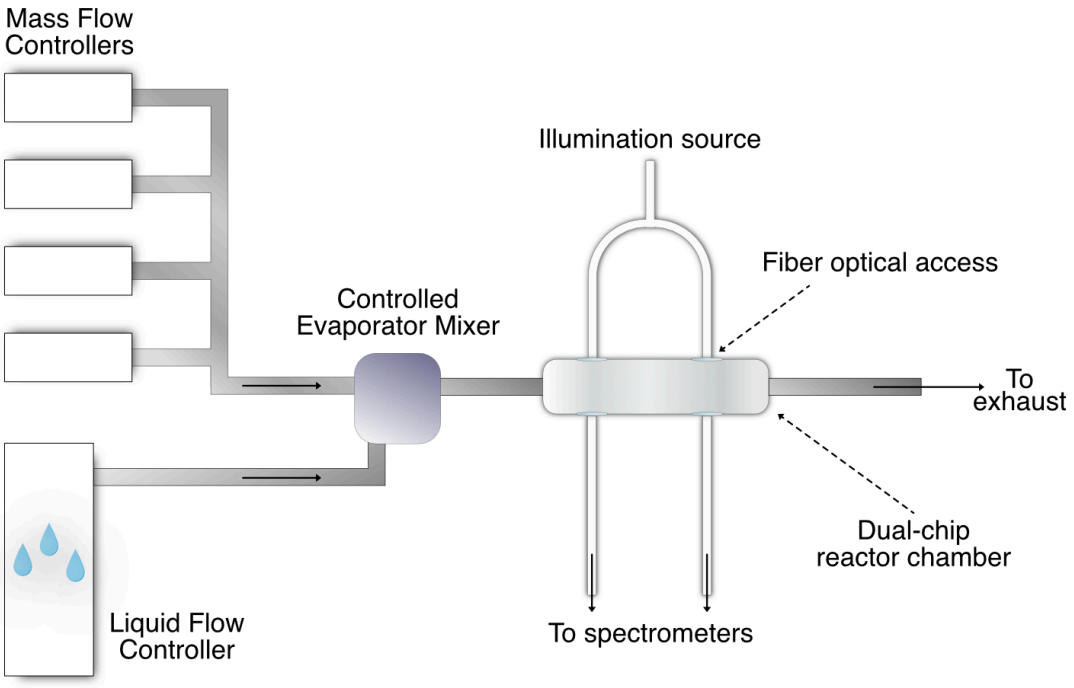

Figure 26. Schematic of the dual-chip setup. A Liquid Flow Controller (LFC) feeds a Controlled Evaporator Mixer (CEM) that allows humidification of the gas supplied by the MFC's up to 80% RH at 30°C. The dual-chip reactor chamber allows for *in situ* optical measurements of two sensor chips simultaneously using the same light source.

The other spectroscopy-based setup, which is used in **Paper V**, uses a chamber dedicated for high precision kinetics measurements in chemically complex environments, e.g. CO and NO in synthetic air (Figure 27). The small volume of this reactor translates to a smaller time constant for complete gas exchange compared to the humidity reactor and the single particle setup (section 5.3), meaning that faster intrinsic sensor response times can be accurately measured without being influenced by mass-transport limitations. A double set of MFC's and a pre-mixing station allows flow from one set of MFC's to feed the reactor while preparation and flow stabilization of a

second gas mixture is managed at the second MFC set (Figure 27). Two three-way solenoid valves then allow quick exchange of the two gas mixtures with a time constant of ~45 ms.

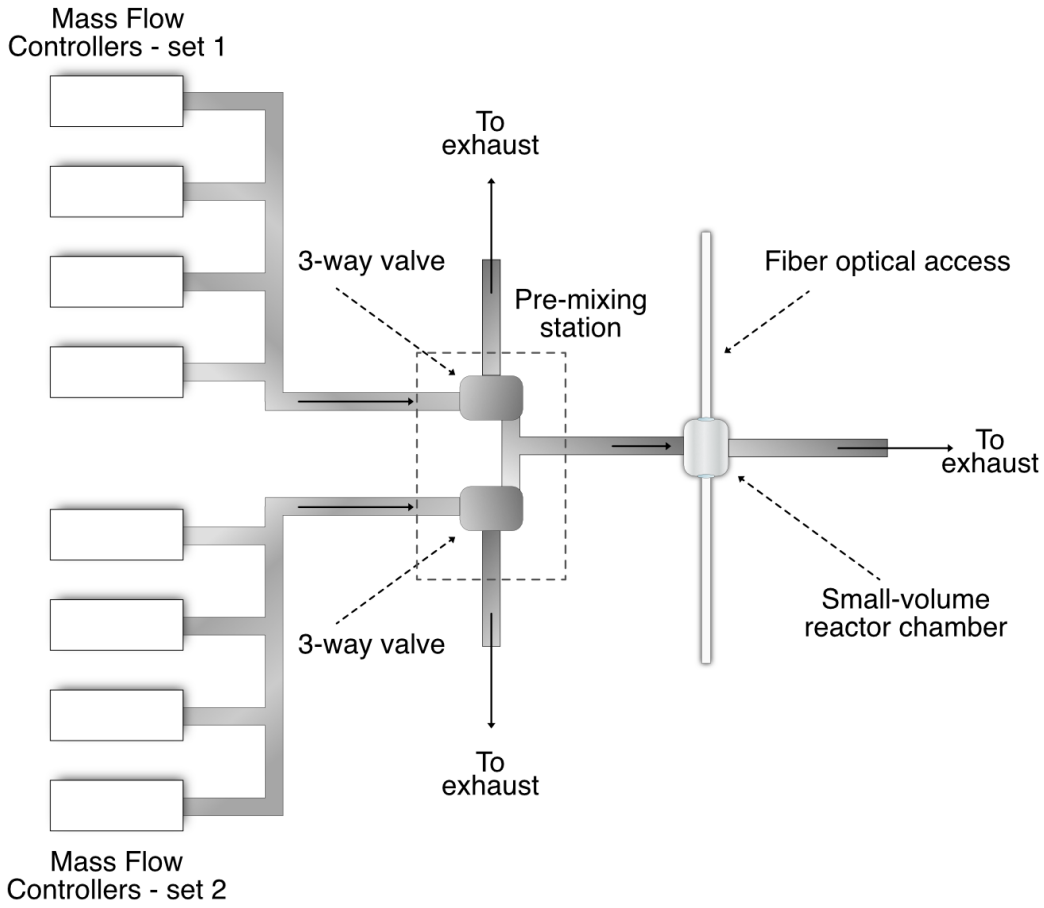

Figure 27. Schematic of the small volume reactor chamber for high precision kinetics measurements. Two sets of MFC's, each connected to a pre-mixing station by a three-way valve, allow pre-mixing and stabilization of a gas flow mixture through one valve + MFC set while the reactor is fed by the other set. The solenoid design of the valves allows for quick switching between the two sets, which together with the small-volume chamber yield a gas exchange constant of ~45 ms.

The final setup uses concepts from all three previous setups, as it includes a CEM for controlled humidification, a small reactor chamber for quick gas exchange and a simple photodiode array for a direct readout of scattered light intensity. This readout method is employed to replicate a low-cost, simple sensing setup that would be straightforward to commercialize and deploy in technologically relevant conditions. In **Paper VI**, we use this setup, with 7 different plasmonic nanoparticle systems on a waveguide, together with a transformer-based deep learning model. This to enable accurate multi-gas sensing of both the H_2, NO, CO and CO_2 concentrations over a full day in a simulated, high humidity and low-air quality metropolitan area.

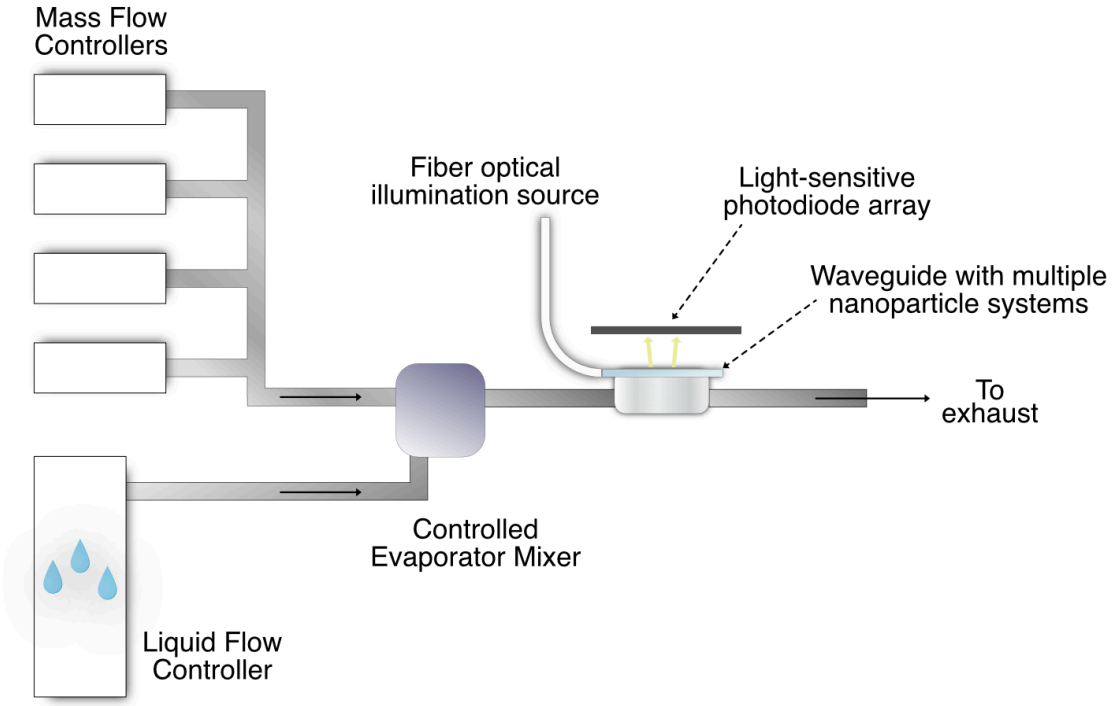

Figure 28. Schematic of the waveguide sensor setup with photodiode array readout. A CEM+LFC combination together with a set of gas control MFC's allow humidification of a wide range of gases. An optical fiber feeds light to the glass waveguide onto which nanoparticle arrays are fabricated, with the scattered light from the nanoparticles collected by a low-cost light-sensitive photodiode array arranged along the waveguide, such that it enables spatially-resolved scattering intensity measurements.

6 Conclusions

In this thesis, I have studied different Pd- and Pt-based materials for hydrogen sensing applications, with a specific focus on technologically relevant chemically complex environments, i.e., air with different sensor response degrading species including H_2O, NO and CO, and the effect of long-term hydrogen cycling. These materials and their hydrogenation characteristics have been studied in the form of disk-shaped nanoparticles, using state-of-the-art nanofabrication, optical hydrogen sensing methods with both single particle and ensemble resolution, and different electron microscopy methods.

6.1 Main Findings

As the main findings and outcomes of the thesis, in **Paper I**, we demonstrate the importance of defect and dislocation networks on the hydrogenation kinetics of individual Pd nanoparticles with different degrees of plastic deformation. Additionally, facilitated by heavy hydrogen cycling, the particles restructure themselves to a degree where there is no discernible difference between initially deformed and pristine particles by top-view SEM imaging. Nonetheless, the difference in hydrogenation kinetics between the two populations is still around an order of a magnitude, demonstrating the importance of internal defect networks on the hydrogenation kinetics of Pd nanoparticles. To this end, based on the kinetic and isothermal hydrogenation data, we propose a mechanism for the structural evolution of Pd nanoparticles on hard substrates during hydrogen cycling. This mechanism involves the diffusion of Pd atoms away from the highly strained particle-substrate interface region and to the particle surface,

coupled with a continuous annihilation of kinetics-accelerating dislocations in the surface-subsurface region of the Pd nanoparticles, leading to a continuous deacceleration of the hydrogen absorption kinetics.

In **Paper II**, we shift our focus to Pt nanoparticles and their interaction with hydrogen in highly humified synthetic air. Here, we find that through synergistic surface reactions, which involve the desorption of surface-adsorbed water layers facilitated by the highly exothermic hydrogen-oxidation reaction (HOR) together with a substitution of surface adsorbed O with H, the Pt plasmonic resonance condition is shifted to higher photon energies in the presence of H_2. This means that Pt can act as a highly efficient catalytic-plasmonic hydrogen sensor in highly humified air. Moreover, the sensor's response magnitude to a given H_2 pulse is increased the higher the humidity level, which we attribute to a direct relationship between the number of desorbed water layers and the sensor's total potential response in terms of plasmonic resonance spectral shift upon exposure to hydrogen. That the exothermic HOR is indeed leading to elevated temperatures of the nanoparticles capable of desorbing water is corroborated by TEM inspection of hydrogen-cycled nanoparticles that reveals distinctive signs of recrystallization similar to what is induced by thermal annealing.

In **Paper III**, we make use of the complementary interactions of Pd and Pt with hydrogen in dry versus highly humid conditions, respectively, to introduce a hybrid sensor-system comprising both metals either as homogeneous alloy or in a layered nanoarchitecture. These systems provide a distinct optical response to hydrogen over the full 0% to 80% relative humidity range considered in synthetic air. The ability of this hybrid system to detect hydrogen in both dry and highly humified conditions stems from

the complementary response of Pd and Pt, where the spectral shifts of the plasmonic resonance of Pd, which is due to the absorption of H into its lattice, are largest in dry conditions, while the response of Pt, as outlined in the last paragraph, is enhanced in more humid conditions by complementing surface reactions.

Broadening the focus to also include alloys of both metals, in **Paper IV**, we develop a new nanofabrication method for spatially highly resolved physical vapor deposition in the lithography-based fabrication of nanostructured surfaces. With this method, we can fabricate thousands of individual nanoparticles, consisting of more than 50 different alloys over an area of ~100 μm x (up to) 5 mm. This method, combined with plasmonic dark-field nanomicroscopy with single-particle resolution, is used in **Paper V** to thoroughly screen 21 different Pd- and Pt-based alloys for their hydrogen sensing characteristics in chemically complex environments, specifically in backgrounds with high concentrations of (detrimental) NO and CO. Based on this screening, we propose a new "champion" system for hydrogen sensing in this demanding environment consisting of the ternary alloy $Pd_{70}Au_{20}Pt_{10}$, which demonstrates more than an order of a magnitude faster response in high concentration NO environments compared to a state-of-the-art $Pd_{70}Au_{30}$ sensor.

Finally, in **Paper VI**, we combine the insights gained from the previous studies and design a low-cost, multiplexed sensor platform utilizing Pd, Pt, PdPt, PdPtAu, PdAu, PdAuCu and Au nanoparticle systems together with a transformer-based deep learning network, which accurately quantifies both H_2, CO, NO and CO_2 concentrations in a simulated, high-humidity and poor air-quality metropolitan area. Hence, we demonstrate that by a rational

choice of active hydrogen sensing materials, enabled by effective material screening methods, Pd- and Pt-based materials combined with contemporary machine learning methods can be used to enable efficient and accurate hydrogen sensing in demanding and highly technologically relevant conditions, e.g. highly urbanized areas with realistic, elevated humidity levels and air pollution.

To summarize, this thesis further elucidates the intricacies between the defect networks of individual nanoparticles and their evolution upon hydrogen cycling, and how these can be stabilized with a few at% of a secondary alloyant. Furthermore, this thesis provides a thorough investigation of the hydrogen sorption properties of more than 70 different Pd- and Pt-based systems, with more than 30 tested in CO, NO_x or H_2O rich backgrounds, enabling sensor systems that demonstrates excellent hydrogen detection in highly challenging, realistic conditions.

6.2 Limitations and Future Perspectives

Fully characterizing individual nanoparticles at an atomic level, and especially nanoparticles of the relatively large size studied in this thesis, is a highly challenging process. Even with state-of-the-art electron microscopes, atomic probe tomographs, and advanced synchrotron beamlines, where an extensive characterization of a single few nanoparticles could potentially be possible, it is practically unfeasible to conduct such detailed measurements on a large scale. Consequently, the discussion regarding particle-to-particle variance within populations of nominally identical particles, i.e., particles being of the same composition, fabricated on the same sample at the same time and treated in the same way post fabrication, must be kept relatively

superficial. For example, if two nominally identical particles demonstrate different hydrogenation properties, but no discernible difference can be found from top-down SEM imaging, this difference will generally be attributed to "individuality in internal structure", i.e., different (unknown) defect distributions and/or distribution of alloyants. To this end, more exhaustive, high-throughput characterization methods with atomic resolution are desperately needed to fully resolve this problem. Until then, more superficial structure characterization, e.g., high-resolution, top-down SEM imaging of a large number of individual nanoparticles, coupled with deep-learning methods, could potentially extract structure-property relationships from the combined imaging and hydrogenation data than what would previously been possible.

Moreover, the surface state of both Pd- and Pt-based nanoparticles is critical for the different reactions occurring on these particles that are discussed in this thesis, e.g., HOR and H-absorption. The surface state of the nanoparticles includes (i) the dynamic distribution of atoms at the nanoparticle surface, which is especially important for alloy nanoparticles, (ii) the shape and morphology of the nanoparticle surface, e.g. including edges, facets and defects, and (iii) concentration of both intended and unintended adsorbed molecular gas species. In this context, "intended" species include sensor interferents, e.g. NO and CO, *if* they are part of the experiment, while "unintended" refers to unintentional and unwanted contaminants. The presence of such unwanted contaminants is a constant worry in most types of surface sciences and why benchmarking against reference systems is of utmost important. In this thesis, we generally use previous, established studies on Pd or PdAu nanoparticle systems to compare our results against, and is one reason for why, for example, isotherm data is

a recurring feature in most of the included papers. For single-particle studies, the reference systems, e.g., Pd and PdAu, can be directly fabricated on the same sample as other systems of interest, and used to directly "sanity check" the results from different measurements. Still, using methods with more direct resolution of the surface state of the nanoparticles, e.g., AFM-IR, could be a rational extension of the studies in this thesis.

Acknowledgments

First, I would like to acknowledge the funding provided by the Knut & Alice Wallenberg Foundation and the Swedish Foundation for Strategic Research, which has enabled the PhD thesis.

Secondly, I would like to thank my main supervisor Christoph, who gave me the opportunity to work with a project that I truly enjoyed, whose advice has been critical for my development as a researcher, and who I have truly enjoyed working together with.

I would also like to extend my gratitude to:

My co-supervisor Joachim, for whom yet another e-beam session or collapsing dry-etch machine is just business as usual.

My examiner Henrik, who gave me feedback on this thesis and strives to keep the division the best workplace it can be.

Past and present members of the Langhammer group, who are always willing to help with small and large things in the lab, and with a special thanks to Thanos, with whom several productive collaborations have been conducted in the context of this work.

Past and present members of the division of Chemical Physics whose lunch company are always enjoyable.

Eva Olsson, who put me on the research track by providing me with a full-year Master thesis project with training on state-of-the-art electron microscopes.

The Chalmers Materials Analysis Laboratory, Nanofabrication Laboratory, and Industrial Materials Science, who provide the infrastructure necessary for high-end nanoscience.

And finally, my family, friends and especially my partner Amanda, all who have been supportive during my PhD endeavor and whose support have been invaluable.

References

1 IEA. Net Zero by 2050. (IEA Paris, 2021). https://www.iea.org/reports/net-zero-by-2050 License: CC BY 4.0

2 Sand, M. *et al.* A multi-model assessment of the Global Warming Potential of hydrogen. *Communications Earth & Environment* **4** (2023). https://doi.org/10.1038/s43247-023-00857-8

3 Ocko, I. B. & Hamburg, S. P. Climate consequences of hydrogen emissions. *Atmospheric Chemistry and Physics* **22**, 9349-9368 (2022). https://doi.org/10.5194/acp-22-9349-2022

4 Schultz, M. G., Diehl, T., Brasseur, G. P. & Zittel, W. Air pollution and climate-forcing impacts of a global hydrogen economy. *Science* **302**, 624-627 (2003). https://doi.org/10.1126/science.1089527

5 Tromp, T. K., Shia, R. L., Allen, M., Eiler, J. M. & Yung, Y. L. Potential environmental impact of a hydrogen economy on the stratosphere. *Science* **300**, 1740-1742 (2003). https://doi.org/10.1126/science.1085169

6 Hübert, T., Boon-Brett, L., Black, G. & Banach, U. Hydrogen sensors – A review. *Sensors and Actuators B: Chemical* **157**, 329-352 (2011). https://doi.org/10.1016/j.snb.2011.04.070

7 Darmadi, I., Nugroho, F. A. A. & Langhammer, C. High-Performance Nanostructured Palladium-Based Hydrogen Sensors—Current Limitations and Strategies for Their Mitigation. *ACS Sensors* **5**, 3306-3327 (2020). https://doi.org/10.1021/acssensors.0c02019

8 Swager, T. M. *et al.* Critical Sensing Modalities for Hydrogen: Technical Needs and Status of the Field to Support a Changing Energy Landscape. *ACS Sens* **9**, 2205-2227 (2024). https://doi.org/10.1021/acssensors.4c00251

9 Koo, W. T. *et al.* Chemiresistive Hydrogen Sensors: Fundamentals, Recent Advances, and Challenges. *ACS Nano* **14**, 14284-14322 (2020). https://doi.org/10.1021/acsnano.0c05307

10 U.S. Department of Energy. *Hydrogen and Fuel Cell Technologies Office Multi-Year Program Plan. Section 8.3,* 143-145, **2024**

11 International Organization for Standardization. *Hydrogen detection apparatus─Stationary applications (ISO Standard No. 26142:2010).* **2010**

12 Klockar, P. *Insplorion Sensor Systems AB*. Optical measurement device. US12504373B2 (2021).

13 H.Koda & Ono, K. *FIS Inc*. Hydrogen gas sensor. US7980116B2 (2008).

14 Mendoza, E. & Menon, A. *OpTech Ventures LLC*. Hydrogen sensor apparatus and method of fabrication. US6535658B1 (2000).

15 Lundström, I., Shivaraman, S., Svensson, C. & Lundkvist, L. A hydrogen−sensitive MOS field−effect transistor. *Applied Physics Letters* **26**, 55-57 (1975). https://doi.org/10.1063/1.88053

16 Favier, F., Walter, E. C., Zach, M. P., Benter, T. & Penner, R. M. Hydrogen sensors and switches from electrodeposited palladium mesowire arrays. *Science* **293**, 2227-2231 (2001). https://doi.org/10.1126/science.1063189

17 Ngo, T. A. *et al.* Fullerene-decorated PdCo nano-resistor network hydrogen sensors with sub-second response and parts-per-billion detection at room temperature. *Nat Commun* **17**, 977 (2025). https://doi.org/10.1038/s41467-025-67708-2

18 Luong, H. M. *et al.* Sub-second and ppm-level optical sensing of hydrogen using templated control of nano-hydride geometry and composition. *Nat Commun* **12**, 2414 (2021). https://doi.org/10.1038/s41467-021-22697-w

19 Bannenberg, L., Schreuders, H. & Dam, B. Tantalum-Palladium: Hysteresis-Free Optical Hydrogen Sensor Over 7 Orders of Magnitude in Pressure with Sub-Second Response. *Advanced Functional Materials* **31**, 2010483 (2021). https://doi.org/10.1002/adfm.202010483

20 Luong, H. M. *et al.* Ultra-fast and sensitive magneto-optical hydrogen sensors using a magnetic nano-cap array. *Nano Energy* **109** (2023). https://doi.org/10.1016/j.nanoen.2023.108332

21 Nugroho, F. A. A. *et al.* Inverse designed plasmonic metasurface with parts per billion optical hydrogen detection. *Nat Commun* **13**, 5737 (2022). https://doi.org/10.1038/s41467-022-33466-8

22 He, Y., Cheng, Y., Yang, C. & Guo, C. F. Creep-free polyelectrolyte elastomer for drift-free iontronic sensing. *Nat Mater* **23**, 1107-1114 (2024). https://doi.org/10.1038/s41563-024-01848-6

23 Lee, M. W., Lee, E. J. & Lee, K.-Y. Comparative analysis of NOx reduction on Pt, Pd, and Rh catalysts by DFT calculation and microkinetic modeling. *Applied Surface Science* **611**, 155572 (2023). https://doi.org/10.1016/j.apsusc.2022.155572

24 Hao, X. *et al.* Experimental and Theoretical Study of CO Oxidation on PdAu Catalysts with NO Pulse Effects. *Topics in Catalysis* **52**, 1946-1950 (2009). https://doi.org/10.1007/s11244-009-9378-y

25 Honkala, K., Pirilä, P. & Laasonen, K. CO and NO adsorption and co-adsorption on the Pd(111) surface. *Surface Science* **489**, 72-82 (2001). https://doi.org/10.1016/s0039-6028(01)01135-9

26 Loffreda, D., Simon, D. & Sautet, P. Vibrational frequency and chemisorption site: a DFT-periodic study of NO on Pd (111) and Rh (111) surfaces. *Chemical Physics Letters* **291**, 15-23 (1998). https://doi.org/10.1016/s0009-2614(98)00569-7

27 Herron, J. A., Tonelli, S. & Mavrikakis, M. Atomic and molecular adsorption on Pd(111). *Surface Science* **606**, 1670-1679 (2012). https://doi.org/10.1016/j.susc.2012.07.003

28 Loffreda, D., Simon, D. & Sautet, P. Dependence of stretching frequency on surface coverage and adsorbate–adsorbate interactions: a density-functional theory approach of CO on Pd (111). *Surface Science* **425**, 68-80 (1999). https://doi.org/10.1016/s0039-6028(99)00186-7

29 Barrera, O. *et al.* Understanding and mitigating hydrogen embrittlement of steels: a review of experimental, modelling and design progress from atomistic to continuum. *J Mater Sci* **53**, 6251-6290 (2018). https://doi.org/10.1007/s10853-017-1978-5

30 Wagner, S. & Pundt, A. Quasi-thermodynamic model on hydride formation in palladium–hydrogen thin films: Impact of elastic and microstructural constraints. *International journal of hydrogen energy* **41**, 2727-2738 (2016). https://doi.org/10.1016/j.ijhydene.2015.11.063

31 Alekseeva, S. *et al.* Grain-growth mediated hydrogen sorption kinetics and compensation effect in single Pd nanoparticles. *Nature Communications* **12**, 5427 (2021). https://doi.org/10.1038/s41467-021-25660-x

32 Ulvestad, A. & Yau, A. The self-healing of defects induced by the hydriding phase transformation in palladium nanoparticles. *Nature Communications* **8**, 1-6 (2017). https://doi.org/10.1038/s41467-017-01548-7

33 Čížek, J. *et al.* Hydrogen-induced microstructural changes of Pd films. *International journal of hydrogen energy* **38**, 12115-12125 (2013). https://doi.org/10.1016/j.ijhydene.2013.03.096

34 Kirchheim, R. Hydrogen solubility and diffusivity in defective and amorphous metals. *Progress in Materials Science* **32**, 261-325 (1988). https://doi.org/10.1016/0079-6425(88)90010-2

35 Delmelle, R. *et al.* Effect of structural defects on the hydriding kinetics of nanocrystalline Pd thin films. *International Journal of Hydrogen Energy* **40**, 7335-7347 (2015). https://doi.org/10.1016/j.ijhydene.2015.04.017

36 Lu, H., Liu, C., Wang, B. & Cheng, Y. F. Lagging hydrogen detection standardization threatens energy transition. *Nature Sensors* **1**, 101-104 (2026). https://doi.org/10.1038/s44460-025-00027-7

37 Andersson, C. *Hydrogen sorption properties of Pd-based nanoparticles - the role of alloying and internal structure* Licentiate thesis, Chalmers University of Technology, (2024).

38 Maier, S. A. *Plasmonics: Fundamentals and Applications*. 1st edn, Vol. 148 (Springer US, 2007).

39 Ekborg-Tanner, P. *et al.* Computational Design of Alloy Nanostructures for Optical Sensing of Hydrogen. *ACS Applied Nano Materials* **5**, 10225-10236 (2022). https://doi.org/10.1021/acsanm.2c01189

40 Bennett, P. A. & Fuggle, J. C. Electronic structure and surface kinetics of palladium hydride studied with x-ray photoelectron spectroscopy and electron-energy-loss spectroscopy. *Physical Review B* **26**, 6030-6039 (1982). https://doi.org/10.1103/PhysRevB.26.6030

41 Silkin, V. M., Diez Muino, R., Chernov, I. P., Chulkov, E. V. & Echenique, P. M. Tuning the plasmon energy of palladium-hydrogen systems by varying the hydrogen concentration. *J Phys Condens Matter* **24**, 104021 (2012). https://doi.org/10.1088/0953-8984/24/10/104021

42 Poyli, M. A. *et al.* Multiscale Theoretical Modeling of Plasmonic Sensing of Hydrogen Uptake in Palladium Nanodisks. *The Journal of Physical Chemistry Letters* **3**, 2556-2561 (2012). https://doi.org/10.1021/jz3007723

43 Palm, K. J., Murray, J. B., Narayan, T. C. & Munday, J. N. Dynamic Optical Properties of Metal Hydrides. *ACS Photonics* **5**, 4677-4686 (2018). https://doi.org/10.1021/acsphotonics.8b01243

44 Wicke, E., Brodowsky, H. & Züchner, H. in *Hydrogen in Metals II: Application-Oriented Properties* (1st ed.) *Topics in Applied Physics* (eds G. Alefeld & J. Völkl) 73-155 (Springer, 1978).

45 Frazier, G. A. & Glosser, R. Phase diagrams of thin films of the palladium hydrogen system using a quartz crystal thickness monitor. *Journal of Physics D: Applied Physics* **12**, L113-L115 (1979). https://doi.org/10.1088/0022-3727/12/10/002

46 Nugroho, F. A. A., Darmadi, I., Zhdanov, V. P. & Langhammer, C. Universal Scaling and Design Rules of Hydrogen-Induced Optical Properties in Pd and Pd-Alloy Nanoparticles. *ACS Nano* **12**, 9903-9912 (2018). https://doi.org/10.1021/acsnano.8b02835

47 Kelly, K. L., Coronado, E., Zhao, L. L. & Schatz, G. C. The Optical Properties of Metal Nanoparticles: The Influence of Size, Shape, and Dielectric Environment. *The Journal of Physical Chemistry B* **107**, 668-677 (2002). https://doi.org/10.1021/jp026731y

48 Langhammer, C., Zoric, I., Kasemo, B. & Clemens, B. M. Hydrogen storage in Pd nanodisks characterized with a novel nanoplasmonic sensing scheme. *Nano Lett* **7**, 3122-3127 (2007). https://doi.org/10.1021/nl071664a

49 Nugroho, F. A. A., Eklund, R., Nilsson, S. & Langhammer, C. A fiber-optic nanoplasmonic hydrogen sensor: Via pattern-transfer of nanofabricated PdAu alloy nanostructures. *Nanoscale* **10**, 20533-20539 (2018). https://doi.org/10.1039/c8nr03751e

50 Nugroho, F. A. A. *et al.* Metal–polymer hybrid nanomaterials for plasmonic ultrafast hydrogen detection. *Nature Materials* **18**, 489-495 (2019). https://doi.org/10.1038/s41563-019-0325-4

51 Pham, M. T. *et al.* Pd80Co20Nanohole Arrays Coated with Poly(methyl methacrylate) for High-Speed Hydrogen Sensing with a Part-per-Billion Detection Limit. *ACS Applied Nano Materials* **4**, 3664-3674 (2021). https://doi.org/10.1021/acsanm.1c00169

52 Westerwaal, R. J. *et al.* High throughput screening of Pd-alloys for H2 separation membranes studied by hydrogenography and CVM. *International Journal of Hydrogen Energy* **36**, 1074-1082 (2011). https://doi.org/10.1016/j.ijhydene.2010.10.014

53 Theodoridis, A., Andersson, C., Nilsson, S., Fritzsche, J. & Langhammer, C. A Catalytic-Plasmonic Pt Nanoparticle Sensor for Hydrogen Detection in High-Humidity Environments. *ACS Sens* **10**, 8983-8994 (2025). https://doi.org/10.1021/acssensors.5c03166

54 Zhu, J. X., Cheng, J. & Doblhoff-Dier, K. Dielectric profile at the Pt(111)/water interface. *J Chem Phys* **162** (2025). https://doi.org/10.1063/5.0239284

55 Liu, N., Tang, M. L., Hentschel, M., Giessen, H. & Alivisatos, A. P. Nanoantenna-enhanced gas sensing in a single tailored nanofocus. *Nature Materials* **10**, 631-636 (2011). https://doi.org/10.1038/nmat3029

56 Hinkle, A. R., Nöhring, W. G., Leute, R., Junge, T. & Pastewka, L. The emergence of small-scale self-affine surface roughness from deformation. *Science advances* **6**, eaax0847 (2020). https://doi.org/10.1126/sciadv.aax0847

57 Kim, D. H. *et al.* High-Resolution, Fast, and Shape-Conformable Hydrogen Sensor Platform: Polymer Nanofiber Yarn Coupled with Nanograined Pd@Pt. *ACS Nano* **13**, 6071-6082 (2019). https://doi.org/10.1021/acsnano.9b02481

58 Wang, W. *et al.* Development of a High Stability Pd-Ni Alloy Thin-Film Coated SAW Device for Sensing Hydrogen. *Sensors (Basel)* **19** (2019). https://doi.org/10.3390/s19163560

59 Wang, W. *et al.* Development of a Pd/Cu nanowires coated SAW hydrogen gas sensor with fast response and recovery. *Sensors and Actuators B: Chemical* **287**, 157-164 (2019). https://doi.org/10.1016/j.snb.2019.02.047

60 Tsuji, T. *et al.* Highly Sensitive Ball Surface Acoustic Wave Hydrogen Sensor with Porous Pd-Alloy Film. *Materials Transactions* **55**, 1040-1044 (2014). https://doi.org/10.2320/matertrans.I-M2014816

61 Sil, D., Hines, J., Udeoyo, U. & Borguet, E. Palladium nanoparticle-based surface acoustic wave hydrogen sensor. *ACS Appl Mater Interfaces* **7**, 5709-5714 (2015). https://doi.org/10.1021/am507531s

62 Boon-Brett, L. *et al.* Identifying performance gaps in hydrogen safety sensor technology for automotive and stationary applications. *International Journal of Hydrogen Energy* **35**, 373-384 (2010). https://doi.org/10.1016/j.ijhydene.2009.10.064

63 Lu, X., Wu, S., Wang, L. & Su, Z. Solid-state amperometric hydrogen sensor based on polymer electrolyte membrane fuel cell. *Sensors and Actuators B: Chemical* **107**, 812-817 (2005). https://doi.org/10.1016/j.snb.2004.12.022

64 Miyamoto, A. *et al.* Solid Electrolyte Gas Sensor Based on a Proton-Conducting Graphene Oxide Membrane. *ACS Omega* **2**, 2994-3001 (2017). https://doi.org/10.1021/acsomega.7b00239

65 Cho, H. J. *et al.* Pt-Functionalized PdO Nanowires for Room Temperature Hydrogen Gas Sensors. *ACS Sens* **3**, 2152-2158 (2018). https://doi.org/10.1021/acssensors.8b00714

66 Jung, W. B. *et al.* Polyelemental Nanolithography via Plasma Ion Bombardment: From Fabrication to Superior H(2) Sensing Application. *Adv Mater* **31**, e1805343 (2019). https://doi.org/10.1002/adma.201805343

67 Dai, J. *et al.* Improved performance of fiber optic hydrogen sensor based on WO3-Pd2Pt-Pt composite film and self-referenced demodulation method. *Sensors and Actuators B: Chemical* **249**, 210-216 (2017). https://doi.org/10.1016/j.snb.2017.04.103

68 Dai, J. *et al.* Early Detection of Hydrogen Leakage Using Fiber Optic Hydrogen Sensor Based on WO(3)-PdPt-Pt Nanocomposite Films. *Nanomaterials (Basel)* **15** (2025). https://doi.org/10.3390/nano15110836

69 Wang, J., Dai, J., Hu, W., Zhang, F. & Yang, M. Improved performance of fiber-optic hydrogen sensor of porous Pt/WO3 based on ZIF-8. *International Journal of Hydrogen Energy* **51**, 909-916 (2024). https://doi.org/10.1016/j.ijhydene.2023.06.080

70 Chen, Y., Yang, Y., Liang, C., Yao, Y. & Chen, J. Investigation of fiber Bragg grating hydrogen sensor based on Pd78Ag15Ni7 ternary alloy. *International Journal of Hydrogen Energy* **193** (2025). https://doi.org/10.1016/j.ijhydene.2025.152241

71 Del Orbe Henriquez, D. *et al.* Pt Nanostructures Fabricated by Local Hydrothermal Synthesis for Low-Power Catalytic-Combustion Hydrogen Sensors. *ACS Applied Nano Materials* **4**, 7-12 (2020). https://doi.org/10.1021/acsanm.0c02794

72 Dabill, D. W., Gentry, S. J. & Walsh, P. T. A fast-response catalytic sensor for flammable gases. *Sensors and Actuators* **11**, 135-143 (1987). https://doi.org/10.1016/0250-6874(87)80012-4

73 Hwang, T. Y. *et al.* Pt/Graphene Catalyst and Tellurium Nanowire-Based Thermochemical Hydrogen (TCH) Sensor Operating at Room Temperature in Wet Air. *ACS Appl Mater Interfaces* **11**, 47015-47024 (2019). https://doi.org/10.1021/acsami.9b12604

74 Kittel, C. *Introduction to Solid State Physics*. 8th edn, (John Wiley & Sons, 2005).

75 Griffith, A. A. VI. The phenomena of rupture and flow in solids. *Philosophical Transactions of the Royal Society of London, Series A: Containing Papers of a Mathematical or Physical Character* **221**, 163-198 (1921). https://doi.org/10.1098/rsta.1921.0006

76 Haidemenopoulos, G. N. *Physical Metallurgy*. (CRC Press, 2018).

77 Kirchheim, R. Lattice discontinuities affecting the generation and annihilation of diffusible hydrogen and vice versa. *Philosophical Transactions of the Royal Society A: Mathematical, Physical and Engineering Sciences* **375**, 20160403 (2017). https://doi.org/10.1098/rsta.2016.0403

78 Sherby, O. D. & Wadsworth, J. Ancient blacksmiths, the Iron Age, Damascus steels, and modern metallurgy. *Journal of Materials Processing Technology* **117**, 347-353 (2001). https://doi.org/10.1016/s0924-0136(01)00794-4

79 Li, X., Lu, L., Li, J., Zhang, X. & Gao, H. Mechanical properties and deformation mechanisms of gradient nanostructured metals and alloys. *Nature Reviews Materials* **5**, 706-723 (2020). https://doi.org/10.1038/s41578-020-0212-2

80 Kraftmakher, Y. Equilibrium vacancies and thermophysical properties of metals. *Physics Reports* **299**, 79-188 (1998). https://doi.org/10.1016/S0370-1573(97)00082-3

81 Van der Ven, A., Ceder, G., Asta, M. & Tepesch, P. D. First-principles theory of ionic diffusion with nondilute carriers. *Physical Review B* **64** (2001). https://doi.org/10.1103/PhysRevB.64.184307

82 Chen, C. C. *et al.* Three-dimensional imaging of dislocations in a nanoparticle at atomic resolution. *Nature* **496**, 74-77 (2013). https://doi.org/10.1038/nature12009

83 Nilsson Pingel, T., Jorgensen, M., Yankovich, A. B., Gronbeck, H. & Olsson, E. Influence of atomic site-specific strain on catalytic activity of supported nanoparticles. *Nat Commun* **9**, 2722 (2018). https://doi.org/10.1038/s41467-018-05055-1

84 Bisht, A. *et al.* The impact of alloying on defect-free nanoparticles exhibiting softer but tougher behavior. *Nature Communications* **12**, 2515 (2021). https://doi.org/10.1038/s41467-021-22707-x

85 Liang, Z. & Rabkin, E. The effect of composition and long-range order on the strength of defect-free faceted Cu-Au nanoparticles. *Acta Materialia* **266** (2024). https://doi.org/10.1016/j.actamat.2024.119680

86 Sharma, A., Hickman, J., Gazit, N., Rabkin, E. & Mishin, Y. Nickel nanoparticles set a new record of strength. *Nature Communications* **9**, 4102 (2018). https://doi.org/10.1038/s41467-018-06575-6

87 Sharma, A., Kositski, R., Kovalenko, O., Mordehai, D. & Rabkin, E. Giant shape- and size-dependent compressive strength of molybdenum nano- and microparticles. *Acta Materialia* **198**, 72-84 (2020). https://doi.org/10.1016/j.actamat.2020.07.054

88 Flanagan, T. J., Kovalenko, O., Rabkin, E. & Lee, S.-W. The effect of defects on strength of gold microparticles. *Scripta Materialia* **171**, 83-86 (2019). https://doi.org/10.1016/j.scriptamat.2019.06.023

89 Bei, H. *et al.* Compressive strengths of molybdenum alloy micro-pillars prepared using a new technique. *Scripta Materialia* **57**, 397-400 (2007). https://doi.org/10.1016/j.scriptamat.2007.05.010

90 Bei, H., Gao, Y., Shim, S., George, E. P. & Pharr, G. M. Strength differences arising from homogeneous versus heterogeneous dislocation nucleation. *Physical Review B* **77**, 060103 (2008). https://doi.org/10.1103/PhysRevB.77.060103

91 Mordehai, D. *et al.* Size effect in compression of single-crystal gold microparticles. *Acta Materialia* **59**, 5202-5215 (2011). https://doi.org/10.1016/j.actamat.2011.04.057

92 Taylor, G. I. The mechanism of plastic deformation of crystals. Part I.—Theoretical. *Proceedings of the Royal Society of London. Series A, Containing Papers of a Mathematical and Physical Character* **145**, 362-387 (1934).

93 Orowan, E. For crystal plasticity. III. *Z Phys* **89**, 634-659 (1934). https://doi.org/10.1007/Bf01341480

94 Polanyi, M. Über eine Art Gitterstörung, die einen Kristall plastisch machen könnte. *Z Phys* **89**, 660-664 (1934).

95 El-Awady, J. A. Unravelling the physics of size-dependent dislocation-mediated plasticity. *Nature communications* **6**, 5926 (2015). https://doi.org/10.1038/ncomms6926

96 Legros, M., Dehm, G., Arzt, E. & Balk, T. J. Observation of giant diffusivity along dislocation cores. *Science* **319**, 1646-1649 (2008). https://doi.org/10.1126/science.1151771

97 Rabier, J. & Puls, M. Atomistic calculations of point-defect interaction and migration energies in the core of an edge dislocation in NaCl. *Philosophical Magazine A* **59**, 533-546 (1989). https://doi.org/10.1080/01418618908229783

98 NobelPrize.org. *The Nobel Prize in Chemistry 2007*, https://www.nobelprize.org/prizes/chemistry/2007/summary/ (Accessed 1 Mar 2026).

99 NobelPrize.org. *The Nobel Prize in Chemistry 1932*, https://www.nobelprize.org/prizes/chemistry/1932/summary/ (Accessed 1 Mar 2026).

100 NobelPrize.org. *The Nobel Prize in Physics 1981*, https://www.nobelprize.org/prizes/physics/1981/summary/ (Accessed 1 Mar 2026).

101 NobelPrize.org. *The Nobel Prize in Physics 1986*, https://www.nobelprize.org/prizes/physics/1986/summary/ (Accessed 1 Mar 2026).

102 Norskov, J. K. *et al.* The nature of the active site in heterogeneous metal catalysis. *Chem Soc Rev* **37**, 2163-2171 (2008). https://doi.org/10.1039/b800260f

103 Tan, C., Chen, J., Wu, X.-J. & Zhang, H. Epitaxial growth of hybrid nanostructures. *Nature Reviews Materials* **3** (2018). https://doi.org/10.1038/natrevmats.2017.89

104 Yang, Y., Hellman, A. & Gronbeck, H. Inherent strain and kinetic coupling determine the kinetics of ammonia synthesis over Ru nanoparticles. *Nat Commun* **16**, 1625 (2025). https://doi.org/10.1038/s41467-025-56765-2

105 Lu, K. Stabilizing nanostructures in metals using grain and twin boundary architectures. *Nature Reviews Materials* **1**, 1-13 (2016). https://doi.org/10.1038/natrevmats.2016.19

106 Swiatnicki, W., Łojkowski, W. & Grabski, M. W. Investigation of grain boundary diffusion in polycrystals by means of extrinsic grain boundary dislocations spreading rate. *Acta Metallurgica* **34**, 599-605 (1986). https://doi.org/10.1016/0001-6160(86)90175-6

107 Han, J., Thomas, S. L. & Srolovitz, D. J. Grain-boundary kinetics: A unified approach. *Progress in Materials Science* **98**, 386-476 (2018). https://doi.org/10.1016/j.pmatsci.2018.05.004

108 Manchester, F., San-Martin, A. & Pitre, J. The H-Pd (hydrogen-palladium) system. *Journal of phase equilibria* **15**, 62-83 (1994). https://doi.org/10.1007/BF02667685

109 Griessen, R., Strohfeldt, N. & Giessen, H. Thermodynamics of the hybrid interaction of hydrogen with palladium nanoparticles. *Nature Materials* **15**, 311-317 (2016). https://doi.org/10.1038/nmat4480

110 Park, J. S., Park, C. W. & Lee, K. J. Implication of peritectic composition in historical high-tin bronze metallurgy. *Materials Characterization* **60**, 1268-1275 (2009). https://doi.org/10.1016/j.matchar.2009.05.009

111 Sharma, M., Ortlepp, I. & Bleck, W. Boron in Heat-Treatable Steels: A Review. *steel research international* **90** (2019). https://doi.org/10.1002/srin.201900133

112 Melloy, G. F., Summon, P. R. & Podgursky, P. P. Optimizing the boron effect. *Metallurgical Transactions* **4**, 2279-2289 (1973). https://doi.org/10.1007/bf02669367

113 Rotter, M., Pangerl, M., Tegel, M. & Johrendt, D. Superconductivity and crystal structures of (Ba(1-x)Kx)Fe2As2 (x=0-1). *Angew Chem Int Ed Engl* **47**, 7949-7952 (2008). https://doi.org/10.1002/anie.200803641

114 Luetkens, H. *et al.* The electronic phase diagram of the LaO(1-x)F(x)FeAs superconductor. *Nat Mater* **8**, 305-309 (2009). https://doi.org/10.1038/nmat2397

115 Pei, G. X. *et al.* Performance of Cu-Alloyed Pd Single-Atom Catalyst for Semihydrogenation of Acetylene under Simulated Front-End Conditions. *ACS Catalysis* **7**, 1491-1500 (2017). https://doi.org/10.1021/acscatal.6b03293

116 Hannagan, R. T., Giannakakis, G., Flytzani-Stephanopoulos, M. & Sykes, E. C. H. Single-Atom Alloy Catalysis. *Chem Rev* **120**, 12044-12088 (2020). https://doi.org/10.1021/acs.chemrev.0c00078

117 Boucher, M. B. *et al.* Single atom alloy surface analogs in Pd0.18Cu15 nanoparticles for selective hydrogenation reactions. *Phys Chem Chem Phys* **15**, 12187-12196 (2013). https://doi.org/10.1039/c3cp51538a

118 Lin, Z. *et al.* A corus line: nanophase diagrams of miscible bimetallic nanoparticles. *Nanoscale* **17**, 26041-26049 (2025). https://doi.org/10.1039/d5nr03697f

119 Ishimoto, T. & Koyama, M. Electronic structure and phase stability of PdPt nanoparticles. *The Journal of Physical Chemistry Letters* **7**, 736-740 (2016). https://doi.org/10.1021/acs.jpclett.5b02753

120 Bharadwaj, S. R., Kerkar, A. S., Tripathi, S. N. & Dharwadkar, S. R. The palladium-platinum phase diagram. *Journal of the Less Common Metals* **169**, 167-172 (1991). https://doi.org/10.1016/0022-5088(91)90245-y

121 Okamoto, H. & Massalski, T. B. The Au−Pt (Gold-Platinum) system. *Bulletin of Alloy Phase Diagrams* **6**, 46-56 (1985). https://doi.org/10.1007/bf02871187

122 Okamoto, H. & Massalski, T. B. The Au−Pd (Gold-Palladium) system. *Bulletin of Alloy Phase Diagrams* **6**, 229-235 (1985). https://doi.org/10.1007/bf02880404

123 Samsonov, V. *et al.* Puzzles of Surface Segregation in Binary Pt–Pd Nanoparticles: Molecular Dynamics and Thermodynamic Simulations. *Metals* **13** (2023). https://doi.org/10.3390/met13071269

124 Duan, Z. & Wang, G. Monte Carlo simulation of surface segregation phenomena in extended and nanoparticle surfaces of Pt-Pd alloys. *J Phys Condens Matter* **23**, 475301 (2011). https://doi.org/10.1088/0953-8984/23/47/475301

125 Barcaro, G., Fortunelli, A., Polak, M. & Rubinovich, L. Patchy multishell segregation in Pd-Pt alloy nanoparticles. *Nano Lett* **11**, 1766-1769 (2011). https://doi.org/10.1021/nl200322s

126 Kobayashi, H. *et al.* Atomic-level Pd− Pt alloying and largely enhanced hydrogen-storage capacity in bimetallic nanoparticles reconstructed from core/shell structure by a process of hydrogen absorption/desorption. *Journal of the American Chemical Society* **132**, 5576-5577 (2010). https://doi.org/10.1021/ja1013163

127 Koo, W.-T. *et al.* Hydrogen Sensors from Composites of Ultra-small Bimetallic Nanoparticles and Porous Ion-Exchange Polymers. *Chem* **6**, 2746-2758 (2020). https://doi.org/10.1016/j.chempr.2020.07.015

128 Tayal, A. *et al.* Mechanism of Hydrogen Storage and Structural Transformation in Bimetallic Pd-Pt Nanoparticles. *ACS Appl Mater Interfaces* **13**, 23502-23512 (2021). https://doi.org/10.1021/acsami.0c22432

129 Tayal, A. *et al.* Effects of interfacial structure of Pd–Pt nanoparticles on hydrogen solubility. *Journal of Alloys and Compounds* **791**, 1263-1269 (2019). https://doi.org/10.1016/j.jallcom.2019.03.342

130 Lee, Y., Stender, P., Eich, S. M. & Schmitz, G. Probing the Miscibility Gap of the Pt–Pd Binary System by Atom Probe Tomography. *Microscopy and Microanalysis* **28**, 1385-1395 (2022). https://doi.org/10.1017/s1431927621013842

131 Pei, M., Petäjäniemi, M., Regnell, A. & Wijk, O. Toward a Fossil Free Future with HYBRIT: Development of Iron and Steelmaking Technology in Sweden and Finland. *Metals* **10** (2020). https://doi.org/10.3390/met10070972

132 Adhikari, S. & Fernando, S. Hydrogen Membrane Separation Techniques. *Industrial & Engineering Chemistry Research* **45**, 875-881 (2006). https://doi.org/10.1021/ie0506441

133 Ockwig, N. W. & Nenoff, T. M. Membranes for hydrogen separation. *Chem Rev* **107**, 4078-4110 (2007). https://doi.org/10.1021/cr0501792

134 Nivedhitha, K. S. *et al.* Advances in hydrogen storage with metal hydrides: Mechanisms, materials, and challenges. *International Journal of Hydrogen Energy* **61**, 1259-1273 (2024). https://doi.org/10.1016/j.ijhydene.2024.02.335

135 Hirscher, M. *et al.* Materials for hydrogen-based energy storage – past, recent progress and future outlook. *Journal of Alloys and Compounds* **827** (2020). https://doi.org/10.1016/j.jallcom.2019.153548

136 Mehr, A. S., Phillips, A. D., Brandon, M. P., Pryce, M. T. & Carton, J. G. Recent challenges and development of technical and technoeconomic aspects for hydrogen storage, insights at different scales; A state of art review. *International Journal of Hydrogen Energy* **70**, 786-815 (2024). https://doi.org/10.1016/j.ijhydene.2024.05.182

137 Coleman, C. & Hardie, D. The hydrogen embrittlement of α-zirconium—A review. *Journal of the less common metals* **11**, 168-185 (1966). https://doi.org/10.1016/0022-5088(66)90003-8

138 Sundell, G., Thuvander, M., Yatim, A. K., Nordin, H. & Andrén, H. O. Direct observation of hydrogen and deuterium in oxide grain boundaries in corroded Zirconium alloys. *Corrosion Science* **90**, 1-4 (2015). https://doi.org/10.1016/j.corsci.2014.10.016

139 Meda, U. S., Bhat, N., Pandey, A., Subramanya, K. N. & Lourdu Antony Raj, M. A. Challenges associated with hydrogen storage systems due to the hydrogen embrittlement of high strength steels. *International Journal of Hydrogen Energy* **48**, 17894-17913 (2023). https://doi.org/10.1016/j.ijhydene.2023.01.292

140 Dong, C. F., Liu, Z. Y., Li, X. G. & Cheng, Y. F. Effects of hydrogen-charging on the susceptibility of X100 pipeline steel to hydrogen-induced cracking. *International Journal of Hydrogen Energy* **34**, 9879-9884 (2009). https://doi.org/10.1016/j.ijhydene.2009.09.090

141 Griessen, R. & Driessen, A. Heat of formation and band structure of binary and ternary metal hydrides. *Physical Review B* **30**, 4372-4381 (1984). https://doi.org/10.1103/PhysRevB.30.4372

142 Ekborg-Tanner, P. & Erhart, P. Hydrogen-Driven Surface Segregation in Pd Alloys from Atomic-Scale Simulations. *The Journal of Physical Chemistry C* **125**, 17248-17260 (2021). https://doi.org/10.1021/acs.jpcc.1c00575

143 Saha, D. & Deng, S. Hydrogen adsorption on ordered mesoporous carbons doped with Pd, Pt, Ni, and Ru. *Langmuir* **25**, 12550-12560 (2009). https://doi.org/10.1021/la901749r

144 Watson, G. W., Wells, R. P. K., Willock, D. J. & Hutchings, G. J. A Comparison of the Adsorption and Diffusion of Hydrogen on the {111} Surfaces of Ni, Pd, and Pt from Density Functional Theory Calculations. *The Journal of Physical Chemistry B* **105**, 4889-4894 (2001). https://doi.org/10.1021/jp002864c

145 Graham, T. XVIII. On the absorption and dialytic separation of gases by colloid septa. *Philosophical transactions of the Royal Society of London*, 399-439 (1866).

146 Schwarzer, M. *et al.* Adsorption and Absorption Energies of Hydrogen with Palladium. *J Phys Chem C Nanomater Interfaces* **126**, 14500-14508 (2022). https://doi.org/10.1021/acs.jpcc.2c04567

147 Kozlov, S. M., Aleksandrov, H. A. & Neyman, K. M. Adsorbed and Subsurface Absorbed Hydrogen Atoms on Bare and MgO(100)-Supported Pd and Pt Nanoparticles. *The Journal of Physical Chemistry C* **118**, 15242-15250 (2014). https://doi.org/10.1021/jp502575a

148 Behm, R. J., Penka, V., Cattania, M. G., Christmann, K. & Ertl, G. Evidence for ‘‘subsurface’’ hydrogen on Pd(110): An intermediate between chemisorbed and dissolved species. *The Journal of Chemical Physics* **78**, 7486-7490 (1983). https://doi.org/10.1063/1.444739

149 Grönbeck, H. & Zhdanov, V. P. Effect of lattice strain on hydrogen diffusion in Pd: A density functional theory study. *Physical Review B* **84** (2011). https://doi.org/10.1103/PhysRevB.84.052301

150 Mamatkulov, M. & Zhdanov, V. P. Partial or complete suppression of hysteresis in hydride formation in binary alloys of Pd with other metals. *Journal of Alloys and Compounds* **885**, 160956 (2021). https://doi.org/10.1016/j.jallcom.2021.160956

151 Namba, K. *et al.* Acceleration of hydrogen absorption by palladium through surface alloying with gold. *Proceedings of the National Academy of Sciences* **115**, 7896-7900 (2018). https://doi.org/10.1073/pnas.1800412115

152 Delmelle, R., Bamba, G. & Proost, J. In-situ monitoring of hydride formation in Pd thin film systems. *International Journal of Hydrogen Energy* **35**, 9888-9892 (2010). https://doi.org/10.1016/j.ijhydene.2009.11.087

153 Hu, Z., Thundat, T. & Warmack, R. Investigation of adsorption and absorption-induced stresses using microcantilever sensors. *Journal of*

Applied Physics **90**, 427-431 (2001). https://doi.org/10.1063/1.1378333

154 Firth, J. B. XXII.—The sorption of hydrogen by palladium at low temperatures. *Journal of the Chemical Society, Transactions* **117**, 171-183 (1920). https://doi.org/10.1039/CT9201700171

155 Kirchheim, R. & Pundt, A. in *Physical Metallurgy* (5th ed.) (eds D. Laughlin & K. Hono) 2597-2705 (Elsevier, 2014).

156 Ulvestad, A. *et al.* Three-dimensional imaging of dislocation dynamics during the hydriding phase transformation. *Nature Materials* **16**, 565-571 (2017). https://doi.org/10.1038/nmat4842

157 Schwarz, R. B. & Khachaturyan, A. G. Thermodynamics of open two-phase systems with coherent interfaces: Application to metal-hydrogen systems. *Acta Materialia* **54**, 313-323 (2006). https://doi.org/10.1016/j.actamat.2005.08.044

158 Griessen, R. & Riesterer, T. in *Hydrogen in Intermetallic Compounds I: Electronic, Thermodynamic, and Crystallographic Properties, Preparation*ed.) (ed Louis Schlapbach) 219-284 (Springer Berlin Heidelberg, 1988).

159 Borgschulte, A. *et al.* Catalytic activity of noble metals promoting hydrogen uptake. *Journal of Catalysis* **239**, 263-271 (2006). https://doi.org/10.1016/j.jcat.2006.01.031

160 Baldi, A., Narayan, T. C., Koh, A. L. & Dionne, J. A. In situ detection of hydrogen-induced phase transitions in individual palladium nanocrystals. *Nature Materials* **13**, 1143-1148 (2014). https://doi.org/10.1038/nmat4086

161 Wicke, E. & Blaurock, J. New experiments on and interpretations of hysteresis effects of Pd-D2 and Pd-H2. *Journal of the Less Common Metals* **130**, 351-363 (1987). https://doi.org/10.1016/0022-5088(87)90129-9

162 Narayan, T. C. *et al.* Direct visualization of hydrogen absorption dynamics in individual palladium nanoparticles. *Nature Communications* **8**, 14020 (2017). https://doi.org/10.1038/ncomms14020

163 Johnson, N. J. J. *et al.* Facets and vertices regulate hydrogen uptake and release in palladium nanocrystals. *Nat Mater* **18**, 454-458 (2019). https://doi.org/10.1038/s41563-019-0308-5

164 Feenstra, R., Griessen, R. & De Groot, D. Hydrogen induced lattice expansion and effective HH interaction in single phase PdHc. *Journal*

of Physics F: Metal Physics **16**, 1933 (1986). https://doi.org/10.1088/0305-4608/16/12/008

165 Alefeld, G. Phase transitions of hydrogen in metals due to elastic interaction. *Berichte der Bunsengesellschaft für physikalische Chemie* **76**, 746-755 (1972). https://doi.org/10.1002/bbpc.19720760809

166 Horner, H. & Wagner, H. A model calculation for the α-α'phase transition in metal-hydrogen systems. *Journal of Physics C: Solid State Physics* **7**, 3305 (1974). https://doi.org/10.1088/0022-3719/7/18/014

167 Fukai, Y. *The Metal-Hydrogen System*. Vol. 21 (Springer Berlin Heidelberg, 2005).

168 Wagner, S. *et al.* Mechanical stress and stress release channels in 10–350 nm palladium hydrogen thin films with different micro-structures. *Acta Materialia* **114**, 116-125 (2016). https://doi.org/10.1016/j.actamat.2016.05.023

169 Pivak, Y., Schreuders, H., Slaman, M., Griessen, R. & Dam, B. Thermodynamics, stress release and hysteresis behavior in highly adhesive Pd–H films. *International Journal of Hydrogen Energy* **36**, 4056-4067 (2011). https://doi.org/10.1016/j.ijhydene.2010.12.063

170 Amin-Ahmadi, B. *et al.* Dislocation/hydrogen interaction mechanisms in hydrided nanocrystalline palladium films. *Acta Materialia* **111**, 253-261 (2016). https://doi.org/10.1016/j.actamat.2016.03.054

171 Myers, S. M. *et al.* Hydrogen interactions with defects in crystalline solids. *Reviews of Modern Physics* **64**, 559 (1992). https://doi.org/10.1103/RevModPhys.64.559

172 Kirchheim, R. Interaction of hydrogen with dislocations in palladium—I. Activity and diffusivity and their phenomenological interpretation. *Acta Metallurgica* **29**, 835-843 (1981). https://doi.org/10.1016/0001-6160(81)90126-7

173 Mütschele, T. & Kirchheim, R. Segregation and diffusion of hydrogen in grain boundaries of palladium. *Scripta metallurgica* **21**, 135-140 (1987). https://doi.org/10.1016/0036-9748(87)90423-6

174 Pundt, A. & Kirchheim, R. HYDROGEN IN METALS: Microstructural Aspects. *Annual Review of Materials Research* **36**, 555-608 (2006). https://doi.org/10.1146/annurev.matsci.36.090804.094451

175 Deutges, M., Barth, H. P., Chen, Y., Borchers, C. & Kirchheim, R. Hydrogen diffusivities as a measure of relative dislocation densities in

palladium and increase of the density by plastic deformation in the presence of dissolved hydrogen. *Acta Materialia* **82**, 266-274 (2015). https://doi.org/10.1016/j.actamat.2014.09.013

176 Čížek, J., Melikhova, O., Dobroň, P. & Hruška, P. In-situ characterization of hydrogen-induced defects in palladium by positron annihilation and acoustic emission. *International Journal of Hydrogen Energy* **42**, 22460-22467 (2017). https://doi.org/10.1016/j.ijhydene.2017.04.275

177 Lumbeeck, G. *et al.* Effect of hydriding induced defects on the small-scale plasticity mechanisms in nanocrystalline palladium thin films. *Journal of Applied Physics* **124** (2018). https://doi.org/10.1063/1.5055274

178 Alekseeva, S. *et al.* Grain boundary mediated hydriding phase transformations in individual polycrystalline metal nanoparticles. *Nature Communications* **8**, 1084 (2017). https://doi.org/10.1038/s41467-017-00879-9

179 Bannenberg, L. J. *et al.* Direct Comparison of PdAu Alloy Thin Films and Nanoparticles upon Hydrogen Exposure. *ACS Applied Materials and Interfaces* **11**, 15489-15497 (2019). https://doi.org/10.1021/acsami.8b22455

180 Darmadi, I., Khairunnisa, S. Z., Tomeček, D. & Langhammer, C. Optimization of the Composition of PdAuCu Ternary Alloy Nanoparticles for Plasmonic Hydrogen Sensing. *ACS Applied Nano Materials* **4**, 8716-8722 (2021). https://doi.org/10.1021/acsanm.1c01242

181 Darmadi, I., Nugroho, F. A. A., Kadkhodazadeh, S., Wagner, J. B. & Langhammer, C. Rationally Designed PdAuCu Ternary Alloy Nanoparticles for Intrinsically Deactivation-Resistant Ultrafast Plasmonic Hydrogen Sensing. *ACS Sensors* **4**, 1424-1432 (2019). https://doi.org/10.1021/acssensors.9b00610

182 Langhammer, C., Zhdanov, V. P., Zorić, I. & Kasemo, B. Size-Dependent Kinetics of Hydriding and Dehydriding of Pd Nanoparticles. *Physical Review Letters* **104**, 135502 (2010). https://doi.org/10.1103/PhysRevLett.104.135502

183 Nugroho, F. A. A., Iandolo, B., Wagner, J. B. & Langhammer, C. Bottom-Up Nanofabrication of Supported Noble Metal Alloy Nanoparticle Arrays for Plasmonics. *ACS Nano* **10**, 2871-2879 (2016). https://doi.org/10.1021/acsnano.5b08057

184 Wadell, C. *et al.* Hysteresis-free nanoplasmonic Pd–Au alloy hydrogen sensors. *Nano letters* **15**, 3563-3570 (2015). https://doi.org/10.1021/acs.nanolett.5b01053

185 Delmelle, R., Michotte, S., Sinnaeve, M. & Proost, J. Effect of internal stress on the hydriding kinetics of nanocrystalline Pd thin films. *Acta Materialia* **61**, 2320-2329 (2013). https://doi.org/10.1016/j.actamat.2013.01.003

186 Nagumo, M. *Fundamentals of Hydrogen Embrittlement*. Vol. 921 (Springer, 2016).

187 Dwivedi, S. K. & Vishwakarma, M. Hydrogen embrittlement in different materials: A review. *International journal of hydrogen energy* **43**, 21603-21616 (2018). https://doi.org/10.1016/j.ijhydene.2018.09.201

188 Chen, Y.-S. *et al.* Hydrogen trapping and embrittlement in metals – A review. *International Journal of Hydrogen Energy* **136**, 789-821 (2025). https://doi.org/10.1016/j.ijhydene.2024.04.076

189 Chowdhury, M. F. W., Tapia-Bastidas, C. V., Hoschke, J., Venezuela, J. & Atrens, A. A review of influence of hydrogen on fracture toughness and mechanical properties of gas transmission pipeline steels. *International Journal of Hydrogen Energy* **102**, 181-221 (2025). https://doi.org/10.1016/j.ijhydene.2025.01.018

190 Winterbottom, W. L. Equilibrium shape of a small particle in contact with a foreign substrate. *Acta Metallurgica* **15**, 303-310 (1967). https://doi.org/10.1016/0001-6160(67)90206-4

191 Hughes, R. C., Schubert, W. K., Zipperian, T. E., Rodriguez, J. L. & Plut, T. A. Thin-film palladium and silver alloys and layers for metal-insulator-semiconductor sensors. *Journal of Applied Physics* **62**, 1074-1083 (1987). https://doi.org/10.1063/1.339738

192 Jang, J. S. *et al.* Hollow Pd-Ag Composite Nanowires for Fast Responding and Transparent Hydrogen Sensors. *ACS Appl Mater Interfaces* **9**, 39464-39474 (2017). https://doi.org/10.1021/acsami.7b10908

193 Makrides, A. C. Absorption of Hydrogen by Silver—Palladium Alloys. *The Journal of Physical Chemistry* **68**, 2160-2169 (1964). https://doi.org/10.1021/j100790a023

194 Hughes, R. C. & Schubert, W. K. Thin films of Pd/Ni alloys for detection of high hydrogen concentrations. *Journal of Applied Physics* **71**, 542-544 (1992). https://doi.org/10.1063/1.350646

195 Sun, L., Chen, M., Peng, X., Xie, B. & Han, M. The effects of Ni contents on hydrogen sensing response of closely spaced Pd–Ni alloy nanoparticle films. *International Journal of Hydrogen Energy* **41**, 1341-1347 (2016). https://doi.org/10.1016/j.ijhydene.2015.10.117

196 Yamazaki, H., Hayashi, Y., Masunishi, K., Ono, D. & Ikehashi, T. High sensitivity MEMS capacitive hydrogen sensor with inverted T-shaped electrode and ring-shaped palladium alloy for fast response and low power consumption. *Journal of Micromechanics and Microengineering* **28** (2018). https://doi.org/10.1088/1361-6439/aac21d

197 Samsonov, G. V. *The Oxide Handbook*. (1973).

198 Jacob, T. Theoretical investigations on the potential-induced formation of Pt-oxide surfaces. *Journal of Electroanalytical Chemistry* **607**, 158-166 (2007). https://doi.org/10.1016/j.jelechem.2007.03.023

199 Meng, X., Bi, M. & Gao, W. Rapid response hydrogen sensor based on Pd@Pt/SnO2 hybrids at near-ambient temperature. *Sensors and Actuators B: Chemical* **370** (2022). https://doi.org/10.1016/j.snb.2022.132406

200 Yadav, A., Pandey, G., Lawaniya, S. D. & Awasthi, K. Selective hydrogen detection at reduced temperatures using WO3 nanorods functionalized with Pd–Pt alloy nanoparticles. *International Journal of Hydrogen Energy* **177** (2025). https://doi.org/10.1016/j.ijhydene.2025.151560

201 Kilinc, N. Highly sensitive hydrogen sensing properties of Pt-Pd alloy thin films on a flexible substrate. *Nano Express* **6** (2025). https://doi.org/10.1088/2632-959X/ade81d

202 Akiba, H. *et al.* Structural and Thermodynamic Studies of Hydrogen Absorption/Desorption Processes on PdPt Nanoparticles. *The Journal of Physical Chemistry C* **123**, 9471-9478 (2019). https://doi.org/10.1021/acs.jpcc.8b11380

203 Nguyen, T. T. D. *et al.* Superhigh sensing response and selectivity for hydrogen gas using PdPt@ZnO core-shell nanoparticles: Unique effect of alloyed ingredient from experimental and theoretical investigations. *Sensors and Actuators B: Chemical* **354** (2022). https://doi.org/10.1016/j.snb.2021.131083

204 Li, Y. *et al.* Inhibiting Emulative Oxygen Adsorption via Introducing Pt-Segregated Sites into the Pd Surface for Enhanced H(2) Sensing in Air. *ACS Sens* **9**, 5405-5413 (2024). https://doi.org/10.1021/acssensors.4c01622

205 Li, J., Yuan, Z., Mu, Z., Yang, Z. & Meng, F. Synergistic catalytic effect of PdPt bimetallic alloy for room temperature hydrogen detection. *Sensors and Actuators B: Chemical* **405** (2024). https://doi.org/10.1016/j.snb.2024.135404

206 Wadell, C. *et al.* Hysteresis-free nanoplasmonic pd-au alloy hydrogen sensors. *Nano Letters* **15**, 3563-3570 (2015). https://doi.org/10.1021/acs.nanolett.5b01053

207 Pearson, W. B. in *A Handbook of Lattice Spacings and Structures of Metals and Alloys*ed.) (ed W. B. Pearson) 123-130 (Pergamon, 1958).

208 Busch, G., Schlapbach, L. & Seiler, A. in *Hydrides for Energy Storage* (1 ed.) (eds A. F. Andresen & A. J. Maeland) 293-299 (Pergamon, 1978).

209 Mendelsohn, M. H., Gruen, D. M. & Dwight, A. E. The effect of aluminum additions on the structural and hydrogen absorption properties of AB5 alloys with particular reference to the LaNi5−xAlx ternary alloy system. *Journal of the Less Common Metals* **63**, 193-207 (1979). https://doi.org/10.1016/0022-5088(79)90243-1

210 Westerwaal, R. J. *et al.* Nanostructured Pd–Au based fiber optic sensors for probing hydrogen concentrations in gas mixtures. *International Journal of Hydrogen Energy* **38**, 4201-4212 (2013). https://doi.org/10.1016/j.ijhydene.2012.12.146

211 Moysan, I. *et al.* Pd–Pt alloys: correlation between electronic structure and hydrogenation properties. *Journal of Alloys and Compounds* **322**, 14-20 (2001). https://doi.org/10.1016/s0925-8388(01)01202-6

212 Kim, D. Y., Scheicher, R. H., Pickard, C. J., Needs, R. J. & Ahuja, R. Predicted formation of superconducting platinum-hydride crystals under pressure in the presence of molecular hydrogen. *Phys Rev Lett* **107**, 117002 (2011). https://doi.org/10.1103/PhysRevLett.107.117002

213 Scheler, T. *et al.* Synthesis and properties of platinum hydride. *Physical Review B* **83** (2011). https://doi.org/10.1103/PhysRevB.83.214106

214 Norskov, J. K., Bligaard, T., Rossmeisl, J. & Christensen, C. H. Towards the computational design of solid catalysts. *Nat Chem* **1**, 37-46 (2009). https://doi.org/10.1038/nchem.121

215 Greeley, J. & Mavrikakis, M. Alloy catalysts designed from first principles. *Nat Mater* **3**, 810-815 (2004). https://doi.org/10.1038/nmat1223

216 Hammer, B. & Norskov, J. K. Why gold is the noblest of all the metals. *Nature* **376**, 238-240 (1995). https://doi.org/10.1038/376238a0

217 Nørskov, J. K. *et al.* Trends in the Exchange Current for Hydrogen Evolution. *Journal of The Electrochemical Society* **152** (2005). https://doi.org/10.1149/1.1856988

218 Kumara, L. S. R. *et al.* Hydrogen storage and stability properties of Pd-Pt solid-solution nanoparticles revealed via atomic and electronic structure. *Sci Rep* **7**, 14606 (2017). https://doi.org/10.1038/s41598-017-14494-7

219 Yasumatsu, T., Wan, J. L., Matsuyama, M. & Watanabe, K. Absorption of hydrogen isotopes by Pd–Pt alloys. *Journal of Alloys and Compounds* **293-295**, 900-907 (1999). https://doi.org/10.1016/s0925-8388(99)00438-7

220 Yamauchi, M., Kobayashi, H. & Kitagawa, H. Hydrogen storage mediated by Pd and Pt nanoparticles. *Chemphyschem* **10**, 2566-2576 (2009). https://doi.org/10.1002/cphc.200900289

221 Kobayashi, H. *et al.* Double enhancement of hydrogen storage capacity of Pd nanoparticles by 20 at% replacement with Ir; systematic control of hydrogen storage in Pd-M nanoparticles (M = Ir, Pt, Au). *Chem Sci* **9**, 5536-5540 (2018). https://doi.org/10.1039/c8sc01460d

222 Langhammer, C., Larsson, E. M., Kasemo, B. & Zoric, I. Indirect nanoplasmonic sensing: ultrasensitive experimental platform for nanomaterials science and optical nanocalorimetry. *Nano letters* **10**, 3529-3538 (2010). https://doi.org/https://doi.org/10.1021/nl101727b

223 Yamauchi, M., Ikeda, R., Kitagawa, H. & Takata, M. Nanosize Effects on Hydrogen Storage in Palladium. *The Journal of Physical Chemistry C* **112**, 3294-3299 (2008). https://doi.org/10.1021/jp710447j

224 Syrenova, S. *et al.* Hydride formation thermodynamics and hysteresis in individual Pd nanocrystals with different size and shape. *Nature Materials* **14**, 1236-1244 (2015). https://doi.org/10.1038/nmat4409

225 Mamatkulov, M. & Zhdanov, V. P. Suppression of hysteresis in absorption of hydrogen by a Pd-Au alloy. *Physical Review E* **101**, 1-9 (2020). https://doi.org/10.1103/PhysRevE.101.042130

226 Sonwane, C. G., Wilcox, J. & Ma, Y. H. Achieving optimum hydrogen permeability in PdAg and PdAu alloys. *Journal of Chemical Physics* **125** (2006). https://doi.org/10.1063/1.2387166

227 Lynggaard, H., Andreasen, A., Stegelmann, C. & Stoltze, P. Analysis of simple kinetic models in heterogeneous catalysis. *Progress in*

Surface Science **77**, 71-137 (2004). https://doi.org/10.1016/j.progsurf.2004.09.001

228 Borgschulte, A., Gremaud, R. & Griessen, R. Interplay of diffusion and dissociation mechanisms during hydrogen absorption in metals. *Physical Review B* **78**, 094106 (2008). https://doi.org/10.1103/PhysRevB.78.094106

229 Patki, N. S., Lundin, S. T. B. & Way, J. D. Apparent activation energy for hydrogen permeation and its relation to the composition of homogeneous PdAu alloy thin-film membranes. *Separation and Purification Technology* **191**, 370-374 (2018). https://doi.org/10.1016/j.seppur.2017.09.047

230 Richards, P. M. Surface-limited hydrogen release and uptake in metals. *Journal of Nuclear Materials* **152**, 246-258 (1988). https://doi.org/10.1016/0022-3115(88)90333-9

231 Zhao, M., Sloof, W. G. & Böttger, A. J. Modelling of surface segregation for palladium alloys in vacuum and gas environments. *International Journal of Hydrogen Energy* **43**, 2212-2223 (2018). https://doi.org/10.1016/j.ijhydene.2017.12.039

232 Sun, Y., Zwolińska, E. & Chmielewski, A. G. Abatement technologies for high concentrations of NOxand SO2removal from exhaust gases: A review. *Critical Reviews in Environmental Science and Technology* **46**, 119-142 (2015). https://doi.org/10.1080/10643389.2015.1063334

233 Duan, L.-s. *et al.* Emission characteristics of a diesel engine with an electrically heated catalyst under cold start conditions. *Journal of Cleaner Production* **380** (2022). https://doi.org/10.1016/j.jclepro.2022.134965

234 Copernicus Atmosphere Monitoring Service (2021): CAMS European air quality reanalyses. Copernicus Atmosphere Monitoring Service (CAMS) Atmosphere Data Store. Date Accessed: (23rd Feb 2026). *Validated data of CO and NO2 concentrations in Jan and July 2023.* https://doi.org/10.24381/7cc0465a

235 Vrekoussis, M. *et al.* Local and regional air pollution characteristics in Cyprus: A long-term trace gases observations analysis. *Sci Total Environ* **845**, 157315 (2022). https://doi.org/10.1016/j.scitotenv.2022.157315

236 Notario, A. *et al.* Analysis of NO, NO2, NOx, O3 and oxidant (OX=O3+NO2) levels measured in a metropolitan area in the southwest of Iberian Peninsula. *Atmospheric Research* **104-105**, 217-226 (2012). https://doi.org/10.1016/j.atmosres.2011.10.008

237 Carrasco, J., Klimes, J. & Michaelides, A. The role of van der Waals forces in water adsorption on metals. *J Chem Phys* **138**, 024708 (2013). https://doi.org/10.1063/1.4773901

238 Yu, R., Zhang, Z., Lu, X., Chang, I. S. & Liu, T. Variations in dew moisture regimes in desert ecosystems and their influencing factors. *WIREs Water* **7** (2020). https://doi.org/10.1002/wat2.1482

239 Bjorneholm, O. *et al.* Water at Interfaces. *Chem Rev* **116**, 7698-7726 (2016). https://doi.org/10.1021/acs.chemrev.6b00045

240 Hodgson, A. & Haq, S. Water adsorption and the wetting of metal surfaces. *Surface Science Reports* **64**, 381-451 (2009). https://doi.org/10.1016/j.surfrep.2009.07.001

241 Skúlason, E. *et al.* Modeling the Electrochemical Hydrogen Oxidation and Evolution Reactions on the Basis of Density Functional Theory Calculations. *The Journal of Physical Chemistry C* **114**, 18182-18197 (2010). https://doi.org/10.1021/jp1048887

242 Water. in *NIST-JANAF Thermochemical Tables* (4th ed.) *Journal of Physical and Chemical Reference Data* (ed M. W. Chase) Ch. Hydrogen, 1323 (National Institute of Standards and Technology, 1998).

243 Noh, H., Flanagan, T. B. & Sakamoto, Y. Hydrogen-induced segregation in PdPt alloys. *Journal of Alloys and Compounds* **231**, 10-14 (1995). https://doi.org/10.1016/0925-8388(95)01830-1

244 Goodell, P. D. Stability of rechargeable hydriding alloys during extended cycling. *Journal of the Less Common Metals* **99**, 1-14 (1984). https://doi.org/10.1016/0022-5088(84)90330-8

245 Zohra, F. T., Webb, C. J., Lamb, K. E. & Gray, E. M. Degradation of metal hydrides in hydrogen-based thermodynamic machines: A review. *International Journal of Hydrogen Energy* **64**, 417-438 (2024). https://doi.org/10.1016/j.ijhydene.2024.03.228

246 Gamo, T., Moriwaki, Y., Yanagihara, N. & Iwaki, T. Life properties of TiMn alloy hydrides and their hydrogen purification effect. *Journal of the Less Common Metals* **89**, 495-504 (1983). https://doi.org/10.1016/0022-5088(83)90361-2

247 Zou, L. *et al.* Dislocation nucleation facilitated by atomic segregation. *Nat Mater* **17**, 56-63 (2018). https://doi.org/10.1038/nmat5034

248 Chen, J., Li, P. & Lin, E. E. A molecular dynamics study on the mechanical properties of Fe-Ni alloy nanowires and their temperature

dependence. *RSC Adv* **10**, 40084-40091 (2020). https://doi.org/10.1039/d0ra07831j

249 Nitol, M. S., Adibi, S., Barrett, C. D. & Wilkerson, J. W. Solid solution softening in dislocation-starved Mg–Al alloys. *Mechanics of Materials* **150** (2020). https://doi.org/10.1016/j.mechmat.2020.103588

250 Knecht, M. R., Weir, M. G., Frenkel, A. I. & Crooks, R. M. Structural Rearrangement of Bimetallic Alloy PdAu Nanoparticles within Dendrimer Templates to Yield Core/Shell Configurations. *Chemistry of Materials* **20**, 1019-1028 (2007). https://doi.org/10.1021/cm0717817

251 Mamatkulov, M. *et al.* Pd Segregation on the Surface of Bimetallic PdAu Nanoparticles Induced by Low Coverage of Adsorbed CO. *The Journal of Physical Chemistry C* **123**, 8037-8046 (2018). https://doi.org/10.1021/acs.jpcc.8b07402

252 Fredriksson, H. *et al.* Hole-mask colloidal lithography. *Advanced Materials* **19**, 4297-4302 (2007). https://doi.org/10.1002/adma.200700680

253 Kadkhodazadeh, S., Nugroho, F. A. A., Langhammer, C., Beleggia, M. & Wagner, J. B. Optical Property-Composition Correlation in Noble Metal Alloy Nanoparticles Studied with EELS. *ACS Photonics* **6**, 779-786 (2019). https://doi.org/10.1021/acsphotonics.8b01791

254 Rahm, J. M. *et al.* A Library of Late Transition Metal Alloy Dielectric Functions for Nanophotonic Applications. *Advanced Functional Materials* **30**, 2002122 (2020). https://doi.org/10.1002/adfm.202002122

255 Zimmerman, J., Bisht, A., Mishin, Y. & Rabkin, E. Size and shape effects on the strength of platinum nanoparticles. *Journal of Materials Science* **56**, 18300-18312 (2021). https://doi.org/10.1007/s10853-021-06435-7

256 Bhushan, B., Kulkarni, A. V., Bonin, W. & Wyrobek, J. T. Nanoindentation and picoindentation measurements using a capacitive transducer system in atomic force microscopy. *Philosophical Magazine A* **74**, 1117-1128 (1996). https://doi.org/10.1080/01418619608239712

257 Nilsson, S. *et al.* Probing the role of grain boundaries in single Cu nanoparticle oxidation by in situ plasmonic scattering. *Physical Review Materials* **6** (2022). https://doi.org/10.1103/PhysRevMaterials.6.045201

258 Nilsson, S., Albinsson, D., Antosiewicz, T. J., Fritzsche, J. & Langhammer, C. Resolving single Cu nanoparticle oxidation and Kirkendall void formation with in situ plasmonic nanospectroscopy and electrodynamic simulations. *Nanoscale* **11**, 20725-20733 (2019). https://doi.org/10.1039/c9nr07681f

259 Nilsson, S. *et al.* The Role of Grain Boundary Sites for the Oxidation of Copper Catalysts during the CO Oxidation Reaction. *ACS Nano* **17**, 20284-20298 (2023). https://doi.org/10.1021/acsnano.3c06282

260 Albinsson, D. *et al.* Copper catalysis at operando conditions—bridging the gap between single nanoparticle probing and catalyst-bed-averaging. *Nature Communications* **11**, 1-13 (2020). https://doi.org/10.1038/s41467-020-18623-1

261 Albinsson, D. *et al.* Operando detection of single nanoparticle activity dynamics inside a model pore catalyst material. *Sci Adv* **6**, eaba7678 (2020). https://doi.org/10.1126/sciadv.aba7678

262 Insplorion. *Hole-Mask Colloidal Lithography*, https://www.insplorion.com/en/publications/hole-mask-colloidal-lithography/ (Accessed 30th Mar 2026).

263 Tiburski, C., Nugroho, F. A. A. & Langhammer, C. Optical Hydrogen Nanothermometry of Plasmonic Nanoparticles under Illumination. *ACS Nano* **16**, 6233-6243 (2022). https://doi.org/10.1021/acsnano.2c00035